Old Dominion University

ODU Digital Commons

Mechanical & Aerospace Engineering Theses & Dissertations

Mechanical & Aerospace Engineering

Winter 1986

Investigation of Vscous/Inviscid Interaction in Transonic Flow Over Airfoils With Suction

Chadra S. Vemuru
Old Dominion University

Follow this and additional works at: https://digitalcommons.odu.edu/mae_etds

Part of the Mechanical Engineering Commons

INVESTIGATION OF VISCOUS/INVISCID

INTERACTION IN TRANSONIC FLOW OVER AIRFOILS WITH SUCTION

by

Chandra S. Vemuru
M.Tech. (Mechanical Engineering) 1980
Indian Institute of Technology, Madras, India

A Dissertation Submitted to the Faculty of
Old Dominion University in Partial Fulfillment of the
Requirement of the Degree of

DOCTOR OF PHILOSOPHY
MECHANICAL ENGINEERING

OLD DOMINION UNIVERSITY
DECEMBER 1986

Approved by:

_____
S. N. Tiwari (Director)

_____
R. L. Ash

_____
A. S. Roberts

_____
O. Baysal

_____
C. H. Cooke

©1987

CHANDRA SEKHAR VEMURU

All Rights Reserved

ABSTRACT

INVESTIGATION OF VISCOUS/INVISCID

INTERACTION IN TRANSONIC FLOW OVER AIRFOILS WITH SUCTION

Old Dominion University, 1986
Director: Dr. Surendra N. Tiwari

The viscous/inviscid interaction over transonic airfoils with and without suction is studied. The streamline angle at the edge of the boundary layer is used to couple the viscous and inviscid flows. The potential flow equations are solved for the inviscid flow field. In the shock region the Euler equations are solved using the method of integral relations. For this the potential flow solution is used as the initial and boundary conditions. An integral method is used to solve the laminar boundary-layer equations. Since both methods are integral methods, a continuous interaction is allowed between the outer inviscid flow region and the inner viscous flow region.

To avoid the Goldstein singularity near the separation point the laminar boundary-layer equations are derived in an inverse form to obtain solutions for the flows with small separations. The displacement thickness distribution is specified instead of the usual pressure

distribution to solve the boundary-layer equations. The Euler equations are solved for the inviscid flow using finite volume technique and the coupling is achieved by surface transpiration model. A method is developed to apply a minimum amount of suction that is required to have an attached flow on the airfoil. The suction parameter is varied based on the velocity profile parameter and the suction distribution obtained is considered to be close to the optimum value. The turbulent boundary layer equations are derived using the bi-logarithmic wall law for mass transfer. The solution method is similar to the laminar inverse boundary-layer approach. The results are found to be in good agreement with available experimental data and with the results of other computational methods.

ACKNOWLEDGMENT

The author wishes to express his sincere appreciation to Dr. Surendra N. Tiwari for the guidance and encouragement throughout the course of study. He is indebted to Dr. R. B. Ram and W. D. Harvey for their help during the earlier stages of the research work.

The author wishes to thank the members of his Dissertation Guidance Committee, Drs. R. L. Ash, A. S. Roberts, O. Baysal, and C. H. Cooke for encouragement and helpful suggestions. Also, he would like to thank Barbara Kraft for her excellent typing of the manuscript.

TABLE OF CONTENTS

iii

iv

LIST OF FIGURES

v

LIST OF SYMBOLS

A, B	Euler flux vectors
a	Speed of sound, velocity profile parameter
c	Chord length
C_d	Drag coefficient
C_ℓ	Lift coefficient
C_p	Pressure coefficient
c_v	Specific heat at constant volume
c_p	Specific heat at constant pressure
D	Total drag
F, J, Q, R, Z, H	Velocity profile quantities
f	Solution of Falkner-Skan equation
J_c	Jacobian of transformation in Eq. 2.29
K	$1/\gamma\, M_\infty^2$
L	Total lift
m	$(\gamma - 1)M^2/2$
M	Mach number
P	Pressure
R_G	Universal gas constant
Re	Reynolds number
S	Entropy
s, n	Orthogonal curvilinear coordinates measured along and normal to airfoil surface, normalized by chord length
T	Static temperature
U, u	Streamwise velocity
V, v	Normal velocity
U_τ	Frictional velocity
U_β	Wake velocity
V_ω	Suction velocity
V_∞	Free stream velocity

SUBSCRIPTS

e	Edge of the boundary layer
d	Drag
Cr	Critical
∞	Free stream

GREEK LETTERS

α	Angle of attack
β	$\dfrac{a_e P_e}{a_\infty}$
β_1	Eddy viscosity parameter
Γ	Circulation
γ	Ratio of specific heats
δ	Boundary layer thickness normalized by chord length
δ_i^*	Transformed displacement thickness in the incompressible plane

$$\int_0^{\delta_i} \left(1 - \frac{U}{U_e}\right) d\eta$$

δ_i	Transformed boundary layer thickness defined by

$$\frac{a_e}{a_\infty} \int_0^{\delta} \rho\, dn$$

ε	Suction parameter
ζ	Falkner-Skan variable

$$\eta\left[[(m + 1)/2]U_e/v_\infty\, \xi\right]^{1/2}$$

η^+	$U_\tau \eta/\nu$
θ	Surface inclination with respect to the direction of free stream velocity
μ	Viscosity coefficient
ξ, η	Stewartson's transformed coordinates
ρ	Density
τ_ω	Shear stress at wall
Φ	Perturbation potential
ϕ	Velocity potential

x

Chapter 1

INTRODUCTION

Transonic flows are the flows in which the local flow speed is close to the local speed of sound. These flows occur in nozzles, over propellers and turbine blades, around blunt bodies flying supersonically and near airplanes which fly close to the Mach number of one. The interest in transonic flow started due to the problems encountered in the attempts to design efficient commercial aircraft which fly close to but below speed of sound.

The most distinguishing feature of transonic flows is their mixed flow character. The acceleration of the initially subsonic flow over the forward portion of an airfoil is sufficient to provide an embedded region of supersonic flow adjacent to the airfoil surface. This supersonic region is terminated by a shock wave that recompresses the flow.

The qualitative behavior of lift and drag coefficients (C_ℓ and C_d) as functions of free stream Mach number M_∞ is discussed in [1].[*] The critical Mach number M_{cr} is the value of M_∞ for which an embedded supersonic region first appears. As the Mach number increases

_____

beyond M_{cr}, the supersonic region grows, increasing the strength and extent of the terminating shock; C_ℓ also increases and C_d essentially remains constant. As M_∞ increases beyond M_d, the drag rise Mach number, shock and viscous influences cause a rapid increase in drag and, eventually, a decrease in lift. Therefore, the optimum cruise Mach number is for the value of M_∞ just above M_d.

The main objectives for fighter type aircraft are high lift at low drag level, high thrust-to-drag ratio for acceleration, and high load factors for maneuvers. These features make the analysis of transonic flow fields one of the most studied in fluid dynamics. To improve these factors limiting the performance of aircraft, detailed studies (comprising both wind tunnel testing and fluid dynamic computations) have to be performed. The high cost of transonic wind tunnel test time severely limits the number of configurations that can be considered in the search for the optimum design. Considerable attention has been directed in recent years in developing theoretical models for the design of aerodynamic bodies to supplement wind tunnel simulations. Theoretical methods reduce the cost of wind tunnel testing and also provide a data base to check errors due to wind tunnel wall interference, incorrect Reynolds number scaling, model and sting deflections under load. A natural approach to the computation of transonic viscous-inviscid interaction is to use the Reynolds averaged Navier-Stokes equations as a global solution procedure. However according to present trends [2], it could be a long time before computers will attain the power required to perform the routine engineering calculations using the Navier-Stokes equations. An alternative is to use a zonal solution method to compute the transonic viscous-inviscid interaction. This

method involves solving different numerical algorithms for various regions of the flow. An advantage of zonal methods is that simpler equations are used in regions where permissible and, consequently, computer requirements are reduced. A disadvantage of zonal methods is that information must be exchanged at zonal boundaries or zonal overlap regions, which can cause convergence and stability problems.

The first major breakthrough to solve the governing nonlinear partial differential equations was made by Magnus and Yoshihara [3]. They presented a method to solve the steady supercritical planar flows over lifting airfoils using the finite-difference technique. Steady-state solutions were obtained as the asymptotic flow for large times. Mathematically, the description of steady transonic flows requires the solution of "mixed equations," which are elliptic in subsonic regions and hyperbolic in supersonic regions. The problem is nonlinear, and solutions generally contain discontinuities representing shock waves. Murman and Cole [1] presented a governing steady transonic small disturbance potential equation using a mixed finite-difference system. They used central difference formulas in the subsonic region, where the governing equation is elliptic and upwind difference formulas in the supersonic region, where it is hyperbolic. Krupp and Murman [4] extended this method to lifting airfoils. These initial successes started a new field of study, the computational transonic aerodynamics.

After the approach suggested by Murman and Cole [1] for solution to the transonic flow problems there was considerable research interest to solve potential flow equations using different techniques. Lomax et al. [5], Klunker and Neuman [6], Schmidt et al. [7], Albone et al. [8], and Van der Vooren et al. [9] have used various forms of the transonic small

disturbance equations with the aim of improving the solutions. There is also a parallel effort to solve the exact potential equation. Garabedian et al. [10] solved the full equation for velocity potential using a relaxation technique similar to Murman's transonic small perturbation method. In this method the central difference scheme for subsonic flow is replaced by a 'retarded' differencing scheme for supersonic flow. Jameson [11], Arlinger [12], Baker [13], and Caughey and Jameson [14] have obtained results for two-dimensional and axially symmetric flows. Jameson [15] solved the transonic full potential flow equation using a 'rotated' differencing scheme to confirm with the local stream direction. Carlson [16] solved the full, inviscid perturbation potential equation in a Cartesian system. The second-order partial differential equation is replaced with a nonconservative system of finite difference equations which includes Jameson's rotated differencing scheme at the supersonic points. Using a stream function approach, Hafez and Lovell [17] solved the transonic inviscid flow equations. Also numerous techniques were developed to improve the efficiency of the basic algorithms. Ballhaus et al. [18] developed implicit approximate factorization algorithms for steady-state transonic flow problems to accelerate convergence. South and Brandt [19] used a multigrid method to achieve this goal. A hybrid Poisson solver/ successive line over relaxation (SLOR) scheme proposed by Jameson [20] substantially increased the computational efficiency over the conventional SLOR scheme.

The comparison between the solutions using the potential flow equations and experimental data is not very good in the mid to upper transonic regions. This is because of the isentropic assumption

inherent in these formulations. Recently, it was also discovered that these solutions are not unique; for certain angles of attack and Mach numbers, the full potential flow equation yields multiple solutions. Also, large negative or positive lift is predicted even for symmetric airfoils at zero angle of attack. Steinhoff and Jameson [21] noted that the nonuniqueness is not because of the discretization error, but because of the governing partial differential equation itself. Several investigators studied the occurrence and behavior of this anomaly, and concluded that it shows up in the conservative formulation of the partial differential equation [22-24], but not in the nonconservative formulation. This suggests that the anomaly is associated with the approximate treatment of shock waves within the potential formulation since this is the main difference between the conservative and nonconservative formulations.

The solution of Euler equations do not show the anomalous behavior as exhibited by the potential solutions. However, the cost of computations is higher. For flows in the upper transonic range it is necessary to solve the Euler equations because of the rotational nature of the flow. The comparison between the Euler and potential solutions is found to be excellent in the lower transonic or subsonic range. Using Euler equations in the whole flow field or in the shock region should improve the results. Euler equations can be solved either by using the method of integral relations (MIR) or by the finite-difference technique. The method of integral relations has been used by Holt and Masson [25], Melnik and Ives [26], Sato [27], and Tai [28] to solve the Euler equations. This method is valid for transonic flows with moderate to strong shocks. The disadvantage of MIR is that the solution procedure

requires man-machine interactions because of the multiple iterative processes involved. Liepmann [29] and Ackeret et al. [30] investigated the phenomenon of the transonic viscous-inviscid interaction. Their experiments showed that the shock and the boundary layer interact strongly with each other. This phenomenon is of great complexity because the behavior of the boundary layer depends mainly on the Reynolds number, whereas, the conditions in a wave are primarily dependent on the Mach number. The pressure disturbances caused by the shock propagate upstream through the subsonic portion of the boundary layer causing the flow to separate ahead of the shock.

Bauer et al. [31,32] incorporated the Nash and Macdonald [33] turbulent boundary-layer method into the inviscid Garabedian method [10]. The viscous-inviscid interaction was taken into account using a solid displacement model. Collyer and Lock [34-36] used the lag entrainment method of Green et al. [37] to calculate the turbulent boundary layer. The surface transpiration model was used to represent the displacement effect of the boundary layer and wakes on the equivalent inviscid flow. This method has an advantage over the previous method in that the computational grid needs to be generated only once. Melnik [38] used a 'multi deck' model near the trailing-edge region, based on the asymptotic theory of turbulent shear flows in the limit of infinite Reynolds number. The matching between the inviscid and viscous solutions is achieved using the surface transpiration model.

Klineberg and Steger [39] treated the viscous-inviscid interaction by using a boundary-layer integral approach combined with a finite-difference relaxation technique for the small disturbance equations. Inviscid and viscous flows are treated separately even for strong

interactions. Brilliant and Adamson [40] used the method of matched asymptotic expansions for an incident shock interacting with an unseparated laminar boundary layer in transonic flow. Tai [41] coupled the inviscid transonic solution obtained by using the method of integral relations with the integral method developed originally by Lees and Reeves [42] and refined by Klineberg and Lees [43] for compressible, attached and separated laminar boundary layers.

All of the methods discussed above are direct methods where the external pressure distribution is prescribed and the boundary-layer quantities are calculated. These methods exhibit the Goldstein singularity near the separation and are limited to attached flow conditions. As demonstrated by Goldstein [44], the boundary layer growth rate becomes infinite when the shear stress gradient is infinite causing a singularity at the point of separation. This was confirmed by Klineberg and Steger [45], Werle and Davis [46], and Pletcher and Dancey [47]. It is also posssible to get nonunique solutions from direct boundary-layer solutions. For non-similar flows this problem was noted by Murphy and King [48]. Catherall and Mangler [49] pointed out that this does not limit the validity of Prandtl's boundary-layer equations past separation. Using an inverse approach where the boundary-layer thickness distribution is specified, this problem could be avoided. Many of the recent researchers have used inverse boundary-layer equations to calculate separated flows. Carter [50] showed that the inverse boundary-layer solutions compare well with the Navier-Stokes solution. Cebeci et al. [51] used a nonlinear eigenfunction formulation, and Klineberg et al. [45] and Horton [52] specified shear stress in their calculations to obtain regular solutions.

The high cost and time requirements and the resources available for conducting experiments either in the wind tunnel or in flight warrant the need for an approximate suction distribution from a reliable numerical method. Also, the solution procedure should be faster and efficient to perform the routine calculations on any desired airfoil. It is essential to have an idea about the suction quantities or the velocities to maintain full chord laminar flow to reduce viscous drag. This will lead to a better design of Natural Laminar Flow (NLF) or Laminar Flow Controlled (LFC) airfoils. The computational procedure should include both the laminar and turbulent boundary-layer models with a transition criteria. In the viscous-inviscid interaction near the shock and the trailing edge, the wake curvature effect have to be considered. The specific objectives of the present study, therefore, are to develop a computational method which would consider laminar as well as turbulent attached boundary-layer interaction for the flow over transonic airfoils, and to develop a method to obtain the suction distribution for maintaining attached flow on the airfoil.

In Chap. 2 governing equations for the inviscid flow as well as the direct and inverse boundary layer equations are presented. Method of solution to solve these equations is discussed in Chap. 3. Also, the interaction models to couple the outer inviscid flow with the inner viscous flow are presented. Results are obtained for several airfoils using the direct and the inverse boundary-layer approaches for laminar and turbulent flows. These are compared with the available experimental as well as other numerical results in Chap. 4.

Chapter 2

THEORETICAL FORMULATION

2.1 Basic Formulation for Inviscid/Viscous Interaction

The mixed flow field over an airfoil in the transonic range is illustrated in Fig. 2.1. Except in the shock region the potential flow equation is solved by a finite-difference relaxation technique. Euler equations are solved in the shock region. In Sec. 2.1.1 the governing equations for the inviscid flow are presented. The direct boundary-layer equations are derived in Sec. 2.1.2 and the corresponding initial conditions are given in Sec. 2.1.3.

2.1.1 Inviscid Flow

Under the assumption of inviscid and irrotational flow the transonic potential flow equation is given by [53]

$$\left(a^2 - \phi_x^2\right)\phi_{xx} - 2\phi_x \phi_y \phi_{xy} + \left(a^2 - \phi_y^2\right)\phi_{yy} = 0 \qquad (2.1)$$

where ϕ is the velocity potential.

Introducing a perturbation potential of the form

$$\Phi = xV_\infty \cos \alpha + yV_\infty \sin \alpha + V_\infty \phi \qquad (2.2)$$
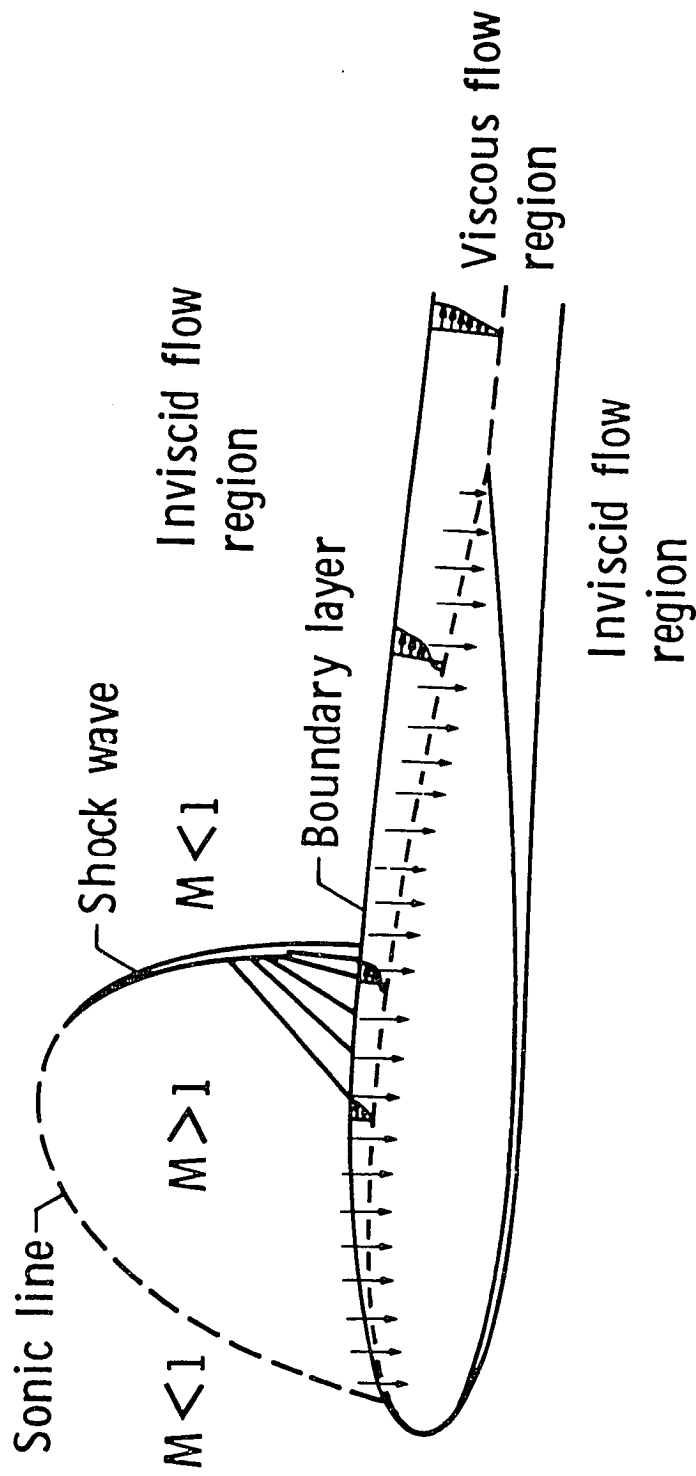
Fig. 2.1 Transonic viscous-inviscid interaction over airfoils with suction.

Equation (2.1) can be written as

$$(a^2 - u^2)\Phi_{xx} - 2uv\Phi_{xy} + (a^2 - v^2)\Phi_{yy} = 0 \qquad (2.3)$$

where $u = \Phi_x$ and $v = \Phi_y$ are the velocity components, and

$$a^2 = a_\infty^2 - \left(\frac{\gamma - 1}{2}\right)\left[u^2 + v^2 - v_\infty^2\right] \qquad (2.4)$$

Equation (2.3) has the form locally, either of a wave equation (hyperbolic type) representing supersonic flow ($\Phi_x > 1$), or of a Laplace equation (elliptic type) representing the subsonic flow ($\Phi_x < 1$). The nonlinear term, $uv\Phi_{xy}$ allows the transition from one type to another.

The boundary conditions for inviscid flow are given as

$$\left(\frac{dy}{dx}\right)_{body} = \left(\frac{v}{u}\right)_{body} \qquad (2.5a)$$

$$\Phi = -\frac{\Gamma}{2\pi}\tan^{-1}\left(\beta\tan(\theta - \alpha)\right) \qquad (2.5b)$$

where circulation Γ is determined by the change in potential across the Kutta-Joukowski cut at the trailing edge (TE), i.e.,

$$\Gamma = \left(\Phi_{y=0^+} - \Phi_{y=0^-}\right)_{TE} \qquad (2.5c)$$

The potential flow equation is rearranged in rotated coordinates parallel and perpendicular to the local velocity. This rearrangement permits coordinate stretching in the physical plane and avoids computational problems in the supersonic region. Several methods are available

[32,54] to solve the potential Eq. (2.3) subjected to the boundary condition, Eq. (2.5).

The isentropic assumption inherent in the potential flow equation, Eq. (2.3), is not valid in the case of moderate to strong shocks across which the increase in entropy cannot be neglected. Therefore, in the shock region it is necessary to solve the Euler equations for the inviscid flow solution. The Euler equations are expressed in vector form as

$$A_x + B_y = 0 \qquad (2.6a)$$

where

$$A = \begin{bmatrix} \rho u \\ \rho u^2 + p \\ \rho uv \end{bmatrix} \; ; \; B = \begin{bmatrix} \rho v \\ \rho uv \\ \rho v^2 + p \end{bmatrix}$$

and

$$c_p T + \tfrac{1}{2}(u^2 + v^2) = \text{constant} \qquad (2.6b)$$

$$p = \rho^\gamma \exp\left(\frac{S_2 - S_1}{c_v}\right) \qquad (2.6c)$$

2.1.2 Viscous Flow

The governing equations for a steady, two-dimensional compressible laminar boundary layer in coordinates parallel and normal to the surface are

Continuity:

$$\frac{\partial(\rho u)}{\partial s} + \frac{\partial(\rho v)}{\partial n} = 0 \tag{2.7}$$

s-momentum:

$$\rho u \frac{\partial u}{\partial s} + \rho u \frac{\partial v}{\partial n} = -K \frac{dp}{ds} + \frac{1}{Re_\infty} \frac{\partial}{\partial n}\left(\mu \frac{\partial u}{\partial n}\right) \tag{2.8}$$

n-momentum:

$$\frac{\partial p}{\partial n} = 0 \tag{2.9}$$

Energy:

$$C_p T + \tfrac{1}{2}(u^2 + v^2) = 0 \tag{2.10}$$

Equation of state:

$$p = \rho RT \tag{2.11}$$

Illingworth [55] and Stewartson [56] have shown that for an adiabatic surface and for a fluid with a Prandtl number of unity, the compressible boundary-layer equation can be transformed into an incompressible form. By applying the Stewartson transformation,

$$\xi = \int_0^s \frac{a_e}{a_\infty} \frac{P_e}{P_\infty} ds; \quad \eta = \int_0^n \frac{a_e}{a_\infty} \frac{\rho_e}{\rho_\infty} \frac{\rho}{\rho_e} dn \tag{2.11a}$$

$$U = (a_\infty/a_e)u; \quad V = \left(\frac{P_\infty}{P_e}\right)\left(\frac{a_\infty}{a_e}\right)^2 u \frac{\partial}{\partial s} \int_0^n \frac{\rho_e}{\rho_\infty} \frac{a_e}{a_\infty} \frac{\rho}{\rho_e} dn$$
$$+ \frac{P_\infty}{P_e} \frac{a_\infty}{a_e} \frac{\rho}{\rho_e} v \tag{2.11b}$$

Eqs. (2.7) - (2.9) are reduced to the incompressible form as

$$\frac{\partial U}{\partial \xi} + \frac{\partial V}{\partial \eta} = 0 \tag{2.12}$$

$$U \frac{\partial U}{\partial \xi} + V \frac{\partial U}{\partial \eta} = U_e \frac{dU_e}{d\xi} + \frac{1}{Re_\infty} \frac{\partial^2 U}{\partial \eta^2} \tag{2.13}$$

In order to avoid the semi-empirical features inherent in the methods such as Crocco-Lees [57], a moment of momentum equation is used in addition to Eqs. (2.12) and (2.13). Upon multiplying Eq. (2.13) by U, one finds

$$U^2 \frac{\partial U}{\partial \xi} + UV \frac{\partial U}{\partial \eta} = UU_e \frac{dU_e}{d\xi} + \frac{1}{Re_\infty} U \frac{\partial^2 U}{\partial \eta^2} \tag{2.14}$$

The governing partial differential equations, Eqs. (2.12) - (2.14), are integrated across the boundary layer resulting in three ordinary differential equations. These equations can be written in the matrix form as

$$
\begin{bmatrix}
F & \delta_i^* & \dfrac{\delta_i^* f_A}{M_e} \\[3ex]
H & \delta_i^* & \dfrac{\delta_i^*(2H + 1)}{M_e} \\[3ex]
J & \delta_i^* \dfrac{dJ}{dH} & \dfrac{3\delta_i^* J}{M_e}
\end{bmatrix}
\begin{bmatrix}
\dfrac{d\delta_i^*}{ds} \\[3ex]
\dfrac{dH}{ds} \\[3ex]
\dfrac{dM_e}{ds}
\end{bmatrix}
=
\begin{bmatrix}
\dfrac{\beta}{m_e} \dfrac{1 + m_e}{1 + m_\infty} \tan \theta - \dfrac{V_\omega}{U_e} \\[3ex]
\beta \dfrac{M_\infty}{M_e} \dfrac{Q}{Re_{\delta_i^*}} + \dfrac{V_\omega}{U_e} \\[3ex]
\beta \dfrac{M_\infty}{M_e} \dfrac{R}{Re_{\delta_i^*}} + \dfrac{V_\omega}{U_e}
\end{bmatrix}
\tag{2.15}
$$

where

$$J = \frac{\Theta_i^*}{\delta_i^*}, \quad Q = \frac{\delta_i^*}{U_e}\left(\frac{\partial U}{\partial \eta}\right)_{\eta=0}, \quad H = \frac{\Theta_i}{\delta_i^*}$$

$$R = \frac{2\delta_i^*}{U_e^2} \int_0^{\delta_i} \left(\frac{\partial U}{\partial \eta}\right)^2 d\eta$$

$$F = H + \frac{1 + m_e}{m_e}$$

$$Z = \frac{1}{\delta_i^*} \int_0^{\delta_i} \frac{U}{U_e} d\eta, \quad Re_{\delta_i^*} = \frac{V_\infty}{\nu_\infty} c\delta_i^*$$

$$f_A = \left(2 + \frac{\gamma+1}{\gamma-1}\frac{m_e}{1+m_e}\right)H + \frac{3\gamma-1}{\gamma-1} + \frac{M_e^2 - 1}{m_e(1+m_e)} Z$$

For a given velocity profile $\frac{U}{U_e}$, the integrals in R and Z can be evaluated and the system of Eq. (2.15) can be solved simultaneously.

Lees and Reeves [42] have shown that the solutions of the Falkner-Skan [58] equation for similar flows including reversed flow profiles calculated by Stewartson [59] can be used to determine J, Q, H, R, and Z as functions of a single parameter 'a'. This is referred to as the velocity profile parameter and is given by

$$a = \frac{\partial(U/U_e)}{\partial(\eta/\delta_i)}\Big|_{\eta=0} = \zeta_{0.99} \, f''(0), \quad 0 \leqslant a \leqslant 4 \quad \text{for attached profile}$$

$$a = \left(\frac{\eta}{\delta_i}\right)_{\frac{U}{U_e} = 0} = \frac{(\zeta)_{f'=0}}{\zeta_{0.99}}, \qquad \begin{array}{l} 0 \leqslant a \leqslant 1 \\ \text{for separated profile} \end{array}$$

$$a = \left(\frac{U}{U_e}\right)_{\substack{\text{dividing} \\ \text{streamline}}} = (f')_{f=0}, \qquad \begin{array}{l} 0 \leqslant a \leqslant 0.46 \\ \text{for wake reversed profile} \end{array}$$

$$a = \left(\frac{U}{U_e}\right)_{\eta=0} = (f')_{\zeta=0}, \qquad \begin{array}{l} 0 \leqslant a \leqslant 1 \\ \text{for wake forward profile} \end{array}$$

The quantity f is obtained from the solution of the Falkner-Skan equation

$$f''' + ff'' + b(1 - f'^2) = 0 \qquad\qquad (2.16)$$

subjected to the boundary conditions

$$f(0) = 0$$

$$f'(0) = 0$$

$$\lim_{\zeta \to \infty} f'(\zeta) = 1$$

These relations for 'a' are valid not only in the case where there is no mass transfer at the wall, but also in cases with mass transfer provided f is obtained by solving Eq. (2.16) with the boundary conditions

$$f(0) = \varepsilon$$

$$f'(0) = 0$$

$$\lim_{\zeta \to \infty} f'(\infty) = 1$$

Considering ε to be a small perturbation, Eq. (2.16) can be written as

$$(f_1 + \varepsilon f_2)''' + (f_1 + \varepsilon f_2)(f_1 + \varepsilon f_2)'' + b\left(1 - (f_1 + \varepsilon f_2)'^2\right) = 0 \quad (2.17)$$

and the boundary conditions as

$$f_1(0) + \varepsilon f_2(0) = \varepsilon \quad (2.17a)$$

$$f_1'(0) + \varepsilon f_2'(0) = 0 \quad (2.17b)$$

$$\lim_{\zeta \to \infty}\left(f_1'(\zeta) + \varepsilon f_2'(\zeta)\right) = 1 \quad (2.17c)$$

For small perturbations, the ε^0 equation is expressed as

$$f_1''' + f_1 f_1'' + b\left(1 - f_1'^2\right) = 0 \quad (2.18)$$

$$f_1(0) = 0$$

$$f_1'(0) = 0$$

and

$$\lim_{\zeta \to \infty} f_1'(\zeta) = 1$$

The ε^1 equation can be expressed

$$f_2''' + f_2 f_1'' + f_1 f_2'' + 2bf_1' f_2' = 0 \quad (2.19)$$

and the boundary conditions are

$$f_2(0) = 1$$

$$f_2'(0) = 0$$

$$\lim_{\zeta \to \infty} f_2'(\zeta) = 0$$

Equation (2.18) is the Falkner-Skan equation and Eq. (2.19) is the auxiliary equation governing f_2.

Solutions to the Falkner-Skan equation are available in the literature for different pressure gradients. But to evaluate the suction quantities, very accurate solutions to the Falkner-Skan equation and the auxiliary equation due to suction are needed. Therefore, these equations subjected to the respective boundary conditions are solved by using the state variable approach of Forbrich [60]. A solution accurate to sixth decimal place can be obtained using this method.

The integral quantities used in Eq. (2.15) consists of the perturbed and unperturbed parts. The unperturbed integral quantities are,

$$H_1 = \frac{1}{\delta_{i1}^*} \int_0^{\zeta_{0.99}} f_1'(1 - f_1')d\zeta \qquad (2.20a)$$

$$J_1 = \frac{1}{\delta_{i1}^*} \int_0^{\zeta_{0.99}} f_1'\left(1 - f_1'^2\right)d\zeta \qquad (2.20b)$$

$$Q_1 = \delta_{i1}^* \, f_1''(0) \qquad (2.20c)$$

$$R_1 = 2\delta_{i1}^* \int_0^{\zeta_{0.99}} f_1^{\prime\prime 2} \, d\zeta \tag{2.20d}$$

$$Z_1 = \frac{1}{\delta_{i1}^*} \left[f_1(\zeta_{0.99}) - f_1(0) \right] \tag{2.20e}$$

where

$$\delta_{i1}^* = \int_0^{\zeta_{0.99}} \left(1 - f_1^\prime \right) d\zeta$$

The perturbed integral quantities are

$$H_2 = \frac{1}{\delta_i^* (1 + b)} \left[(1 + b)(1 + H_1) \left(f_2(\zeta)_{0.99} - 1 \right) \right.$$
$$\left. + f_2^{\prime\prime}(0) - f_2(\zeta)_{0.99} \right] \tag{2.20f}$$

$$J_2 = \frac{1}{\delta_i^*} \left\{ (1 + J_1) \left(f_2(\zeta)_{0.99} - 1 \right) - 3 \int_0^{\zeta_{0.99}} f_1^{\prime 2} f_2^\prime \, d\zeta \right\} \tag{2.20g}$$

$$Q_2 = f_2^{\prime\prime}(0) \delta_i^* - f_1^{\prime\prime}(0) \left(f_2(\zeta)_{0.99} - 1 \right) \tag{2.20h}$$

$$R_2 = \frac{R_1}{\delta_i^*} \left(1 - f_2(\zeta)_{0.99} \right) + 4\delta_i^* \int_0^{\zeta_{0.99}} f_1^{\prime\prime} f_2^{\prime\prime} \, d\zeta \tag{2.20i}$$

$$Z_2 = \frac{(1 + Z_1)}{\delta_i^*} \left[f_2(\zeta)_{0.99} - 1 \right] \tag{2.20j}$$

All these quantities are expressed as polynomials in 'a.' For any combination of the velocity profile parameter and the suction parameter,

the total quantities can be evaluated as $H = H_1 + \varepsilon H_2$, $J = J_1 + \varepsilon J_2$, etc.

Now the system of Eqs. (2.15) can be expressed as

$$\frac{d\delta_i^*}{ds} = \frac{1}{D_1} \begin{vmatrix} d_1 & a_{12} & a_{13} \\ d_2 & a_{22} & a_{23} \\ d_3 & a_{32} & a_{33} \end{vmatrix} \qquad (2.21)$$

$$\frac{da}{ds} = \frac{1}{D_1 \cdot \frac{dH}{da}} \begin{vmatrix} a_{11} & d_1 & a_{13} \\ a_{21} & d_2 & a_{23} \\ a_{31} & d_3 & a_{33} \end{vmatrix} \qquad (2.22)$$

$$\frac{dM_e}{ds} = \frac{1}{D_1} \begin{vmatrix} a_{11} & a_{12} & d_1 \\ a_{21} & a_{22} & d_2 \\ a_{31} & a_{32} & d_3 \end{vmatrix} \qquad (2.23)$$

where a_{ij}, d_j and D_1 are given in Appendix A.

In the usual boundary-layer calculations, the pressure distribution along the airfoil is computed using an inviscid method, and the boundary-layer quantities are evaluated. Since the solution of the viscous and inviscid equations is not simultaneous, mass transfer between these two regions is not allowed and only the momentum and moment of momentum equations are used.

For a specified pressure distribution, Eq. (2.15) reduces to

$$
\begin{bmatrix} H & \delta_i^* \\[2ex] J & \delta_i^* \dfrac{dJ}{dH} \end{bmatrix}
\begin{bmatrix} \dfrac{d\delta_i^*}{ds} \\[2ex] \dfrac{dH}{ds} \end{bmatrix}
=
\begin{bmatrix} \beta \dfrac{M_\infty}{M_e} \dfrac{Q}{Re_{\delta_i^*}} + \dfrac{V_\omega}{U_e} - \dfrac{\delta_i^*(2H+1)}{m_e} \dfrac{dM_e}{ds} \\[3ex] \beta \dfrac{M_\infty}{M_e} \dfrac{R}{Re_{\delta_i^*}} + \dfrac{V_\omega}{U_e} - \dfrac{3\delta_i^* \, J}{M_e} \dfrac{dM_e}{ds} \end{bmatrix}
\qquad (2.24)
$$

This may be rewritten as

$$
\frac{d\delta_i^*}{ds} = \frac{1}{D_2} \begin{vmatrix} b_2 & a_{22} \\[2ex] b_3 & a_{32} \end{vmatrix}
\qquad (2.25)
$$

$$
\frac{da}{ds} = \frac{1}{D_2 \dfrac{dH}{da}} \begin{vmatrix} a_{21} & b_2 \\[2ex] a_{31} & b_3 \end{vmatrix}
\qquad (2.26)
$$

where

$$
D_2 = \begin{vmatrix} a_{21} & a_{22} \\[2ex] a_{31} & a_{32} \end{vmatrix}
$$

$$
b_2 = d_2 - a_{23} \frac{dM_e}{ds}
$$

$$
b_3 = d_3 - a_{33} \frac{dM_e}{ds}
$$

These equations have a singularity at the separation point. If suction is not applied before the flow separates, the denominator becomes zero

and the boundary-layer equations cannot be applied past separation point. This formulation, termed as the weak interaction formulation, should be applied only in the attached flow region.

2.1.3 Initial Conditions

To avoid the stagnation point singularity the calculations are started away from the leading edge. Klineberg and Steger [61], Tai [28], and Ram et al. [62] assumed that the flow is locally similar to derive the initial conditions. Although this assumption is valid for only thin airfoils, it was found by Tai [28] that these conditions can be applied also to blunt airfoils to obtain converged solutions.

For a locally similar flow, $\frac{da}{ds} = 0$ and Eq. (2.26) reduces to

$$\begin{vmatrix} a_{21} & b_2 \\ a_{31} & b_3 \end{vmatrix} = 0$$

or

$$a_{21} b_3 - b_2 a_{31} = 0$$

or

$$H \, \beta \, \frac{M_\infty}{M_e} \, \frac{R}{Re_{\delta_i^*}} + \frac{V_\omega}{U_e} = J \, \beta \, \frac{M_\infty}{M_e} \, \frac{Q}{Re_{\delta_i^*}} + \frac{V_\omega}{U_e} - \frac{\delta_i^* (2H+1)}{M_e} \frac{dM_e}{ds} - \frac{3 \delta_i^* \, J}{M_e} \frac{dM_e}{ds}$$

$$(2.27)$$

Upon substituting for $\frac{dM_e}{ds}$ from Eq. (2.27) into Eq. (2.25), there is obtained

$$\frac{d\delta_i^*}{ds} = \frac{R + 2HR - 3JQ}{J(1 - H)Re_{\delta_i^*}} + \frac{(1 + H - 3J)}{J(1 - H)} \frac{V_\omega}{\delta_e} \qquad (2.27a)$$

or

$$\delta_i^* \frac{d\delta_i^*}{ds} = K_1 \delta_i^* + K_2 \qquad (2.27b)$$

where

$$K_1 = \frac{(1 + H - 3J)}{J(1 - H)} \frac{V_\omega}{U_e}$$

$$K_2 = \frac{(R + 2HR - 3JQ)}{J(1 - H)Re_c}$$

An integration of Eq. (2.27b) with respect to S gives

$$\frac{\delta_i^*}{K_1} - \frac{K_2}{K_1^2} \ell n \left(K_1 \delta_i^* + K_2 \right)_0 = S_0$$

or

$$\left[\delta_i^* K_1 - K_2 \ell n \left(K_1 \delta_i^* + K_2 \right) \right]_0 = [K_1 S]_0 \qquad (2.28)$$

From Eq. (2.27), one finds

$$\delta_i^* = \left[\frac{JQ - HR}{J(1 - H)Re_c} \frac{1}{\frac{dM_e}{ds}} \right]^{1/2}$$

Starting with an initial value of 'a', the velocity profile quantities are computed and both sides of Eq. (2.28) are evaluated. Then the initial value of 'a' is updated depending upon the ratio of the right-hand side to the left-hand side. This iteration process is continued until there is no appreciable change in the velocity profile parameter 'a'. The initial displacement thickness δ_i^* is calculated for this value of 'a'.

2.2 Laminar Inverse Boundary-Layer Interactions

The transformed Euler equations are presented in Sec. 2.2.1 to solve for the entire inviscid flow. In Sec. 2.2.2 the boundary-layer equations are written in an inverse form to avoid the Goldstein singularity past the separation point and the corresponding initial conditions are derived in Sec. 2.2.3.

2.2.1 Inviscid Flow

In the direct boundary-layer computations, Euler equations are solved only in the shock and wake regions. Because of the multiple interative process involved in solving the two different types of equations for the inviscid flow solution, the computational procedure is difficult. It is convenient to solve the Euler equations in the entire inviscid flow region especially when the weak interaction equations are solved in the boundary layer.

For numerical calculations Eqs. (2.6) are transformed into general coordinates using the transformation

$$R = R(x,y)$$

$$S = S(x,y)$$

This results in

$$A_R + B_S = 0 \qquad\qquad (2.29)$$

where

$$A_R = (R_x A + R_y B)/J_c$$

$$B_S = (S_x A + S_y B)/J_c$$

$$J_c = (R_x S_y - R_y S_x)$$

2.2.2 Inverse Boundary-Layer Equations

In the usual boundary-layer method the boundary-layer quantities are calculated for a specified pressure distribution. These methods, termed as direct methods, exhibit the Goldstein singularity near the separation. The flow past separation cannot be calculated because of this singularity. However, this behavior does not limit the validity of the Prandtl equations. In an inverse boundary-layer method the boundary-layer thickness is specified and the pressure distribution is evaluated. An integral method is used to solve the inverse boundary-layer equations in the present approach. For a known boundary-layer thickness distribution, the viscous governing equations, Eqs. (2.15), reduce to

$$
\begin{bmatrix}
\delta_i^* & \dfrac{\delta_i^*(2H + 1)}{M_e} \\[2ex]
\delta_i^* \dfrac{dJ}{dH} & \dfrac{3\delta_i^* J}{M_e}
\end{bmatrix}
\begin{bmatrix}
\dfrac{dH}{ds} \\[2ex]
\dfrac{dM_e}{ds}
\end{bmatrix}
=
\begin{bmatrix}
\beta \dfrac{M_\infty}{M_e} \dfrac{Q}{Re_{\delta_i^*}} + \dfrac{V_\omega}{U_e} - H \dfrac{d\delta_i^*}{ds} \\[2ex]
\beta \dfrac{M_\infty}{M_e} \dfrac{R}{Re_{\delta_i^*}} + \dfrac{V_\omega}{U_e} - J \dfrac{d\delta_i^*}{ds}
\end{bmatrix}
\tag{2.30a}
$$

This is written in a compact form as

$$
\begin{bmatrix} a_{22} & a_{23} \\ a_{32} & a_{33} \end{bmatrix} \begin{bmatrix} \dfrac{dH}{ds} \\ \dfrac{dM_e}{ds} \end{bmatrix} = \begin{bmatrix} K_3 \\ K_4 \end{bmatrix} \tag{2.30b}
$$

where $K_3 = d_2 - H\dfrac{d\delta_i^*}{ds}$ and $K_4 = d_3 - J\dfrac{d\delta_i^*}{ds}$. From Eq. (2.30b) it follows that

$$
\frac{da}{ds} = \frac{1}{D_3 \cdot \dfrac{dH}{da}} \begin{vmatrix} K_3 & a_{23} \\ K_4 & a_{33} \end{vmatrix} \tag{2.31}
$$

$$
\frac{dM_e}{ds} = \frac{1}{D_3} \begin{vmatrix} a_{22} & k_3 \\ a_{32} & k_4 \end{vmatrix} \tag{2.32}
$$

where $D_3 = a_{22}a_{33} - a_{23}a_{32}$. Equations (2.31) and (2.32) can be expressed in an alternate form as

$$
\frac{da}{ds} = \frac{1}{D_3 \cdot \dfrac{dH}{da}} \left[\frac{\beta M_\infty \, \delta_i^*}{M_e^2 \, Re_{\delta_i^*}} \left(3JQ - R(2H+1)\right) + \frac{\delta_i^*}{M_e} \frac{d\delta_i^*}{ds} \left(J(2H+1) - 3JH\right) \right] \tag{2.33}
$$

$$
\frac{dM_e}{ds} = \frac{1}{D_3} \left[\frac{\beta M_e \, \delta_i^*}{M_e \, Re_{\delta_i^*}} \left(R - Q\frac{dJ}{dH}\right) + \delta_i^* \frac{d\delta_i^*}{ds} \left(H\frac{\bar{dJ}}{dH} - J\right) \right] \tag{2.34}
$$

where

$$
D_3 = \frac{\delta_i^{*2}}{M_e} \left(3J - (2H+1)\frac{dJ}{dH}\right)
$$

The inverse boundary-layer equations, Eqs. (2.33) and (2.34), are checked for singularities for both the attached and separated flow conditions. However, for extensive regions of separation, these equations are not valid.

2.2.3 Initial Conditions

Assuming the flow to be locally similar near the leading edge, i.e., $\frac{da}{ds} = 0$, Eq. (2.33) reduces to

$$\frac{\beta M_\infty}{M_e \, Re_{\delta_i^*}} \left(3JQ - R(2H + 1)\right) + \frac{d\delta_i^*}{ds} \left(J(1 - H)\right) = 0$$

or

$$\frac{d\delta_i^*}{ds} = \frac{\beta M_\infty}{M_e \, Re_{\delta_i^*}} K_5/K_6 \qquad (2.35)$$

where

$$K_5 = 3JQ - R(2H + 1)$$

$$K_6 = J(H - 1)$$

Upon substituting for $\frac{d\delta_i^*}{ds}$ in Eq. (2.34), there is obtained

$$\frac{dM_e}{ds} = \left\{ \frac{\beta M_\infty}{\delta_i^* \, Re_{\delta_i^*}} \left(R - Q \frac{dJ}{dH}\right) + \frac{1}{\delta_i^*} \frac{\beta M_\infty}{Re_{\delta_i^*}} \left(H \frac{dJ}{dH} - J\right) \frac{K_5}{K_6} \right\} \Bigg/ D_4 \qquad (2.36)$$

where

$$D_4 = 3J - (2H + 1) \frac{dJ}{dH}$$

Since the velocity profile parameter and the profile quantities are locally constant, Eq. (2.36) can be integrated to obtain

$$
M_e = \left\{ \left[\frac{\beta M_\infty}{\delta_i^* \, Re_{\delta_i^*}} \left(R - Q \frac{dJ}{dH} \right) + \frac{1}{\delta_i^*} \frac{\beta M_\infty}{Re_{\delta_i^*}} \left(H \frac{dJ}{dH} - J \right) \frac{K_5}{K_6} \right] \Big/ D_4 \right\} S_0 \qquad (2.37)
$$

A substitution for M_e in Eq. (2.35), results in

$$
\frac{d\delta_i^*}{ds} \frac{1}{\delta_i^*} \left[\left(R - Q \frac{dJ}{dH} \right) K_6 + \left(H \frac{dJ}{dH} - J \right) K_5 \right] S_0 = K_5 \, D_4 \qquad (2.38)
$$

Solving for the velocity profile parameter 'a', which satisfies Eq. (2.38), gives the initial value for 'a' and for that value the initial Mach number is calculated from Eq. (2.35).

2.3 Turbulent Inverse Boundary-Layer Interaction

The governing equations for a compressible, turbulent boundary layer in coordinates parallel and normal to the surface are [63]

Continuity:

$$
\frac{\partial(\rho u)}{\partial s} + \frac{\partial(\rho v)}{\partial n} = 0 \qquad (2.39)
$$

Momentum:

$$
\rho u \frac{\partial u}{\partial s} + \rho v \frac{\partial u}{\partial n} = -k \frac{dp}{ds} + \frac{1}{\rho_\infty V_\infty c} \frac{\partial}{\partial n} \left(\beta_1 \frac{\partial u}{\partial n} \right) \qquad (2.40)
$$

By applying the Stewartson transformation Eqs. (2.39) and (2.40) are reduced to the incompressible form as

Continuity:

$$U_\zeta + V_\eta = 0 \qquad (2.41)$$

Momentum:

$$UU_\zeta + VU_\eta = U_e(U_e)_\zeta + \frac{1}{Re_\infty}(\beta_1 U_\eta)_\eta \qquad (2.42)$$

The input quantities are transformed to the incompressible form and after the boundary-layer calculations, the results are transformed back into the compressible plane.

2.3.1 Inverse Boundary-Layer Integral Method

The governing partial differential equations are integrated across the boundary layer as

$$\int_0^\delta U_\zeta \, d\eta + \int_0^\delta V_\eta \, d\eta = 0 \qquad (2.43a)$$

or

$$\int_0^\delta U_\zeta \, d\eta = V_\omega - V_e \qquad (2.43b)$$

$$\int_0^\delta \left[UU_\zeta + VU_\eta - U_e(U_e)_\zeta - \frac{1}{Re_\infty}\frac{\partial}{\partial\eta}\left(\beta_1 \frac{\partial U}{\partial\eta}\right) \right] d\eta = 0 \qquad (2.44)$$

A substitution for V from Eq. (2.41) in Eq. (2.44) gives

$$\int_0^\delta \left[UU_\zeta - U_\eta \int_0^\eta U_\zeta \, d\eta - U_e(U_e)_\zeta - \frac{1}{Re_\infty}(\beta_1 U_\eta)_\eta \right] d\eta = 0 \qquad (2.45)$$

As in the laminar boundary-layer problem, a moment of momentum equation is used to obtain the closure relationship.

Velocity Profile

The velocity profile expression similar to Kuhn and Nielson [64] has been used to eliminate the η dependence of the integral equations and this is given by

$$\frac{U}{U_\tau} = 2.5 \; \ell n(1 + \eta^+) + 5.1 - (3.39\eta^+ + 5.1)e^{-0.37\eta^+}$$

$$+ \frac{1}{2} U_\beta [1 - \cos(\Pi \frac{y}{\delta})] + V_\omega [2.5 \; \ell n(1 + \eta^+) + 5.1]^2 \tag{2.46}$$

The parameter U_τ is the friction velocity and is given by

$$U_\tau = (\tau_\omega / |\tau_\omega|)(|\tau_\omega|/\rho)^{1/2} \tag{2.47}$$

Equation (2.46) consists of an inner part, consisting of a laminar sublayer and the law of the wall function, and an outer part, a wake function. The last term in Eq. (2.46) includes the effect of mass transfer.

Eddy Viscosity

The eddy viscosity model used is similar to that used by Tai [63]. The expressions for the eddy viscosity are as follows:

For attached flow, inner layer

$$\beta_1 = 1 + 0.0533\left\{e^{0.41 \frac{U}{U_\tau}} - \left(1 + 0.41 \frac{U}{U_\tau} + 0.5\left(0.41 \frac{U}{U_\tau}\right)^2\right)\right\} \tag{2.48}$$

For attached flow, outer layer

$$\beta_1 = \frac{0.013 + 0.0038 e^{-\left(\delta^*/\tau_w\right)(dp/d\zeta)/15}}{\left[1 + 5.5\left(\frac{\eta}{\delta}\right)^6\right]} U_e \, \delta^* \, Re_\infty \tag{2.49}$$

For separated flow, inner layer

$$\dot\beta_1 = 1 + 0.018 U_e \, \eta Re_\infty\left[1 - \left(\frac{U}{U_e}\right)^2\right] \tag{2.50}$$

For separated flow, outer layer

$$\beta_1 = \frac{0.013 U_e \, \delta^* \, Re_\infty}{\left[1 + 5.5\left(\frac{\eta}{\delta}\right)^6\right]} \tag{2.51}$$

A substitution of $\frac{U}{U_\tau}$ from Eq. (2.46) into the governing equations, with U_β eliminated by evaluating U at the edge of the boundary layer, results in three ordinary differential equations:

$$\begin{bmatrix} A_{11} & A_{12} & A_{13} \\ A_{21} & A_{22} & A_{23} \\ A_{31} & A_{32} & A_{33} \end{bmatrix} \begin{bmatrix} (U_\tau)_\zeta \\ (\delta^*)_\zeta \\ (U_e)_\zeta \end{bmatrix} = \begin{bmatrix} B_1 \\ B_2 \\ B_3 \end{bmatrix} \tag{2.52}$$

where A_{ij} and B_j are as given in the Appendix B.

The direct boundary-layer calculation corresponds to specifying U_e and solving for δ^* and U_τ. The inverse boundary-layer solution corresponds to specifying δ^* and solving for U_e and U_τ. Equation

(2.52) is reduced to the inverse form after rearranging the terms as

$$
\begin{bmatrix} A_{11} & A_{13} \\ A_{31} & A_{33} \end{bmatrix} \begin{bmatrix} (U_\tau)_\zeta \\ (U_e)_\zeta \end{bmatrix} = \begin{bmatrix} C_1 \\ C_2 \end{bmatrix}
\tag{2.53}
$$

where C_j are as given in the Appendix B.

2.3.2 Initial Conditions

The initial values for the viscous variables are evaluated, based on the Schlichting's skin-friction formula [65] for incompressible flow modified to include pressure gradient, as

$$
\delta^* = \frac{1.4}{U_e^{3.4}} \left[\frac{k(m+1)}{m \ Re_\infty^{1/m}} \int_0^\zeta U_e^{3.4+0.24/m} \, dR \right]^{m/m+1}
\tag{2.54}
$$

and

$$
U_\tau = \frac{0.122}{Re_\infty^{0.1}} \frac{U_e^{1.24+0.24/m}}{\left[\int_0^\zeta U_e^{3.4+2.4/m} \, dR \right]^{0.1}}
\tag{2.55}
$$

where $m = 4$ and $k = 0.0128$. Starting with the inviscid edge velocity, both sides of Eq. (2.54) are evaluated until the required convergence condition is satisfied. For this value of U_e, the frictional velocity U_τ is calculated using Eq. (2.55).

Chapter 3

METHOD OF SOLUTION

The numerical procedures used to solve the direct and inverse boundary-layer equations are presented in this chapter.

3.1 Direct Boundary-Layer Interaction

In the direct approach the pressure distribution from the inviscid flow is specified and the boundary-layer quantities are evaluated. The inviscid flow over an airfoil is obtained by solving the potential flow equation in the entire flow field except in the shock region. In the shock region the Euler equations are solved using the information from the potential flow. This method is referred to as the hybrid method.

In Sec. 3.1.1 the solution method to solve the potential flow equation and the Euler equations is discussed. A survey of the available viscous-inviscid interaction methods and the present method to achieve a continuous interaction between the inviscid and the viscous flow are presented in Sec. 3.1.2. Also, the description of the solution procedure for both flows is given.

3.1.1 Solution of Inviscid Flow Equations

The transonic potential flow equation, Eq. (2.3), subjected to the boundary condition, Eq. (2.5), is solved by the finite-difference

relaxation scheme developed by Carlson [16]. In this method the governing equation is replaced by a nonconservative system of finite-difference equations and the system of equations are solved by a column relaxation technique. This procedure is adopted in this study because the difference equations are solved on a Cartesian grid.

Solution of Euler Equations in the Shock Region

It is necessary to solve the Euler equations in the shock region because of the rotational nature of the flow. It is also important to have a continuous interaction between the inviscid and viscous flows. In order to achieve this, the solution methods should be of the same type for both flows. For this reason the method of integral relations (MIR) is adopted to solve the Euler equations. Melnik and Ives [26], Holt and Mason [25], Sato [27], Tai [28], and Ram et al. [62] have used this method to solve the transonic inviscid flow equations for various flow conditions. Another advantage of using the MIR is its small computational requirement.

The governing partial differential equations are reduced to ordinary differential equations by integrating Eq. (2.6) from the edge of the boundary layer to each strip boundary (Fig. 3.1) at some x location. In order to perform the integration, the integrand is approximated by an interpolation polynomial. For example, A in Eq. (2.6) can be approximated by

$$A = \sum_{k=0}^{N} a_k(x)(y - y_e)^k \qquad (3.1)$$
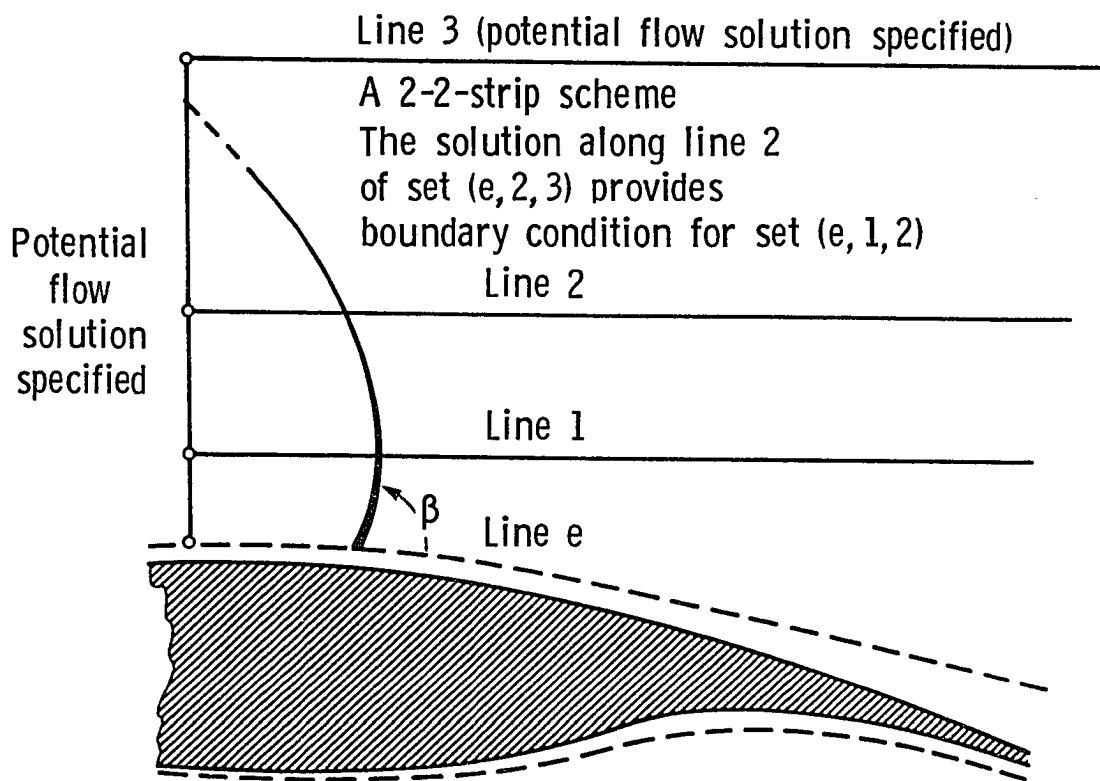
Fig. 3.1   Integration scheme for the method of integral

relation in the shock region.

Using a second-order approximation for Eq. (2.6) the method can be implemented with three strips for desired accuracy. This process is illustrated in Fig. 3.1. The integration domain is divided into two effective regions, which are denoted by strip boundaries (e, 1, 2) and (e, 2, 3). The base boundary e is set at the edge of the boundary layer. The flow conditions are specificed by the potential flow solution on the uppermost boundary 3. First, the MIR is applied to determine the flow conditions along the boundary 2. Then, it is applied to the inner part of the flow field (e, 1, 2).

The resulting ordinary differential equations for the inviscid external flow, reduced by means of the 2-2 strip integration scheme, associated with MIR, along the strip boundaries are

$$\frac{dU_e}{dx} = F_e \qquad (3.2)$$

$$\frac{dV_e}{dx} = G_e \qquad (3.3)$$

$$\rho_e = \left[\frac{C - U_e^2 - V_e^2}{C - 1} \right]^{1/(\gamma-1)} \qquad (3.4)$$

$$P_e = \rho_e^\gamma \qquad (3.5)$$

$$\frac{dU_j}{dx} = F_j \qquad (3.6)$$

$$\frac{dV_j}{dx} = G_j \qquad (3.7)$$

$$\rho_j = \left[\frac{(C - 1)(P_{t2}/\rho_{t2})_j - U_j^2 - V_j^2}{(C - 1)(P_2/\rho_2^\gamma)_j} \right]^{1/(\gamma-1)} \qquad (3.8)$$

$$P_j = \rho_j^\gamma \left(P_2 / \rho_2^\gamma \right)_j \tag{3.9}$$

where F_e, G_e, F_j and G_j are given in Ref. 41.

3.1.2 Shock/Boundary Layer Interaction and Viscous-Inviscid Coupling

In the transonic flow regime the interaction between the boundary layer and the external flow is more important than in the subsonic or supersonic regimes. Also, the Reynolds number has a large effect on the aerodynamic characteristics as confirmed by Loving [66] through experiments in flight and in the wind tunnel.

Experiments by Liepmann [29] and Ackeret et al. [30] indicated that the pressure rise in the boundary layer is much more gradual than in the external inviscid flow. When a normal shock impinges on the boundary layer, the disturbance propagates upstream through the subsonic portion of the boundary layer diffusing within a few boundary-layer thicknesses depending on the strength of the shock. If the pressure gradient is large enough, the flow may separate ahead of the shock. The pressure rise diverges the streamlines in the subsonic region generating compression waves in the supersonic region. In the case of the laminar boundary layer, the foot of the shock is thus smeared and a lambda shock appears. However, this does not necessarily happen in the case of the turbulent boundary layer because it can undergo a larger adverse pressure gradient than a laminar boundary layer. The displacement thickness increases considerably for a laminar boundary layer as compared to a turbulent boundary layer due to the shock. Also, the Reynolds number has a large effect on the laminar interaction but there is almost no effect on the turbulent boundary-layer interaction.

After the shock the laminar boundary layer remains separated all along the airfoil due to the adverse pressure gradients encountered. Preferably, the coupling method should allow the downstream influence on the upstream. These types of viscous-inviscid coupling methods are termed strong interaction coupling methods and others are termed weak interaction coupling methods.

Melnik [38] and LeBalleur [67] gave the recent state-of-art on the coupling of thin shear layer equations with the inviscid potential equations. In Bavitz's [68] method the effect of the wake is not included and an empirical correction near the trailing edge is used. Collyer and Lock [36] included the effect of a wake in their calculations in the form of a normal velocity jump. However, they did not take the shock-boundary-layer interaction into consideration. Melnik et al. [38] have considered the trailing-edge modelling but their method is for airfoils without any separation; also, the shock-boundary-layer interaction is not taken into account.

Nandaman et al. [69] used Inger's [70] non-symptotic multi-deck analysis to predict a realistic pressure calculation in the shock region. They have used a solid displacement model with smoothing for interaction and the effect of a wake is not considered. Also their method is applicable to airfoils without separation.

Wai and Yoshihara [71] considered an empirical model in the shock region to deal with separation. The interaction process is of semi-implicit nature. Updating the mesh periodically the curvature effect of the wake is taken into account by LeBalleur [67]. The interaction is acheived through a surface transpiration model. Klineberg and Lees [43] used the streamline angle at the edge of the boundary layer as a common

variable to allow for the continuous interaction between the boundary layer and the inviscid flow for supersonic external flow. Tai [41], and Ram et al. [62] successfully employed this method for transonic flow. In the present study, this interaction model is used in the hybrid approach where both the viscous and inviscid solutions are obtained by using the integral methods. This facilitates a simultaneous interaction between the inner boundary layer and the outer inviscid flow. The common variable is given by the relation

$$\Theta = \sin^{-1} \frac{V_{e,i}}{M_{e,v}\, a_{e,v}} - \theta \qquad (3.10)$$

where $V_{e,i}$ is the normal velocity component from the inviscid solution and $M_{e,v}\, a_{e,v}$ is the magnitude of velocity from the viscous solution. The mass transfer between the two regions is allowed using the continuity equation

$$\frac{d\delta^*}{ds} = \tan \Theta + (\delta - \delta^*) \frac{d}{ds} \ln(\rho_e\, U_e) \qquad (3.11)$$

where U_e, the horizantal component of velocity at the boundary-layer edge is determined by the equation,

$$U_e = \left[(M_e\, a_e)^2 - V_e^2 \right]^{1/2} \qquad (3.12)$$

The strong interaction formulation can be applied to the attached, as well as separated laminar boundary layers. When it is applied to the attached flows, the boundary layer separates in a short distance. If the usual weak interaction formulation is applied, it is noted that the

separation occurs only at the shock. However, the strong interaction formulation involves another iteration process to determine the location of the shock influence point. In the forward portion of the airfoil, the weak interaction equations are sufficient to account for the interaction.

Solution Procedure

The transonic full potential equation is solved by the finite-difference scheme developed by Carlson [16]. The shock location and the extent of the supersonic region is obtained from the Mach chart. This information is important to locate the shock influence point and to choose the strip boundaries to solve the Euler equations in the shock region.

The initial displacement thickness and the velocity profile parameter are calculated using the procedure given in Sec. 2.2. In the forward portion of the airfoil the interaction between the boundary layer and the inviscid flow is considered to be weak. Therefore, the weak interaction formulation is applied to calculate the boundary-layer thickness and velocity profile parameter for a given pressure distribution. The numerical integration of the boundary-layer equations is performed by a fourth-order Runge-Kutta method until the shock influence point is reached.

Location of the Shock Influence Point

To determine the shock influence point the strong interaction calculations are initiated at a number locations ahead of the shock. The shock location is determined from the inviscid solution. The

displacement thickness (δ_i^*) and the velocity profile parameter 'a' are kept continuous when the switch is made from the weak interaction to strong interaction formulation. Also the velocity gradient at the edge of the boundary layer should be continuous to achieve convergence for the influence point. This is done by adjusting the streamline angle at the boundary-layer edge.

In the inviscid flow region Euler equations are solved using the method of integral relations. The potential flow solution is taken as the initial condition along the vertical line and as the boundary condition along the outermost strip. The inviscid, as well as the viscous solutions, are obtained simultaneously.

Usually the flow is separated shortly after the strong interaction equations are applied. If suction is not applied to keep the flow attached, the boundary-layer quantities are calculated based on the separated profiles. The integration continues downstream through the trailing edge and into the wake. At the trailing edge it is important to check the velocity gradient and adjust the streamline angle before continuing the calculation into the wake.

The downstream boundary condition is satisfied for the correct shock influence point. The upper and lower surfaces are treated separately to compute the displacement thickness distributions. The velocity discontinuity at the trailing edge should be zero to satisfy the Kutta condition. This is checked by comparing the static pressures at the trailing edge from the upper and lower surfaces. The displacement thickness distribution is underrelaxed using a procedure discribed in Sec. 2.6.

The airfoil is updated by adding the displacement thickness to the original airfoil coordinates and the inviscid flow is computed for the updated airfoil with a new circulation accounting for the pressure difference near the trailing edge. With the new inviscid potential flow solution and the location of the shock, the procedure is repeated. This overall iteration process is continued until a specified convergence criteria on the displacement thickness is satisfied.

3.2 Inverse Boundary-Layer Interaction

In the inverse approach the boundary-layer thickness distribution is specified to avoid the separation point singularity. Semi-inverse coupling is used to couple the outer inviscid flow and the inner viscous flow. The solution method to solve the Euler equations in the entire flow field is presented in Sec. 3.2.1. The coupling method and the solution procedure for either a laminar boundary layer or a turbulent boundary layer are given in Sec. 3.2.2.

3.2.1 Solution of Euler Equations Using Finite-Volume Approach

The inviscid flow equations, Eqs. (2.29), are solved using the finite-volume approach developed by Jameson et al. [72]. The discretization procedure decouples the spatial and time terms using the method of lines. The computational domain is divided into quadrilateral cells as shown in the Fig. 3.2, and a system of ordinary differential equations is obtained by applying Eq. (2.29) to each of these cells separately. This resulting system of equations is solved by the Runge-Kutta time stepping scheme.
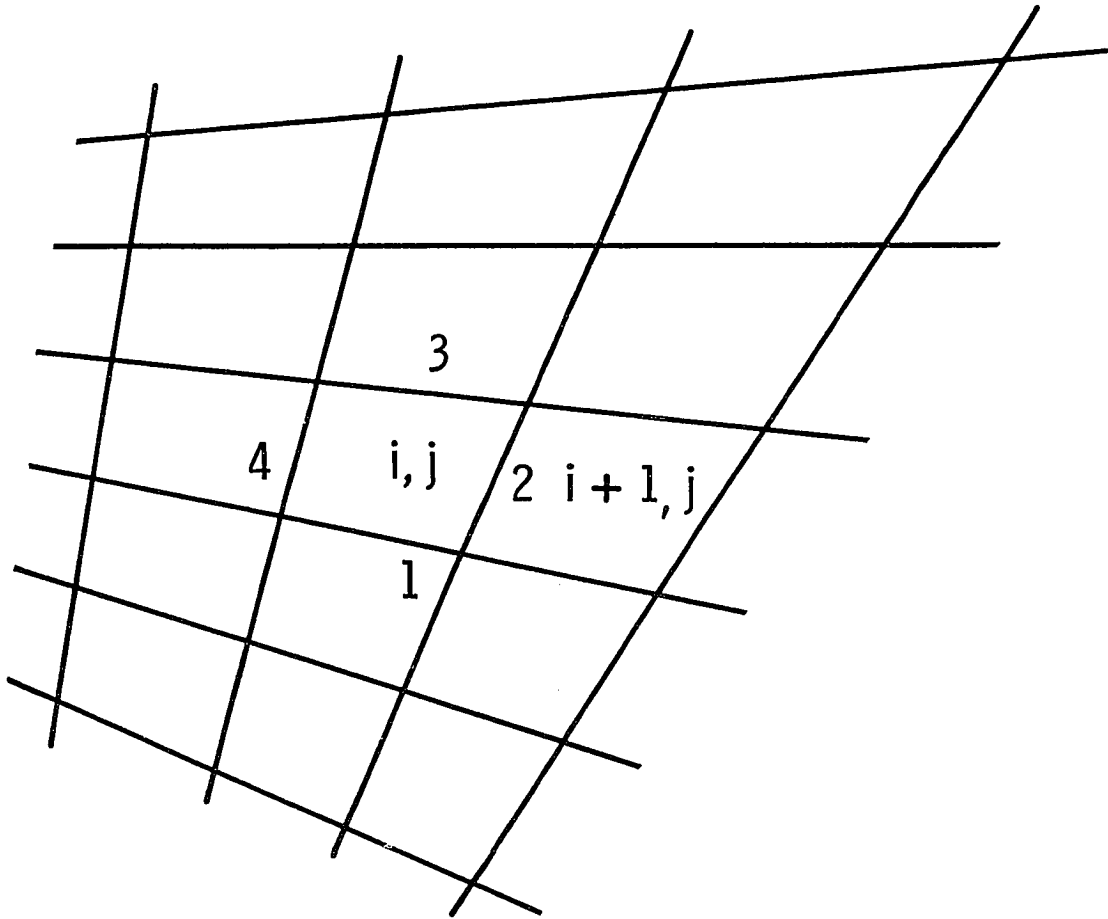
Fig. 3.2 Computational grid for solving Euler

equations by finite-volume approach.

The Runge-Kutta scheme has the advantage of allowing explicit time steps greater than a Courant number of one at the expense of evaluating additional functions at different stages. Whitfield et al. [73] has done some numerical experiments to find an optimum Courant number to perform the calculations. In this study, a four-stage Runge-Kutta scheme (with a Courant number of 2.8) is used; this is suggested in [74].

To suppress the oscillations near the shock and the stagnation points some external dissipation is added. The dissipative terms are a mixed blend of second-and fourth-order terms which are of third-order in smooth regions of flow and of first-order in the shock region.

The convergence to steady state is accelarated by using a local time step (determined by the local Courant number) and by adding a forcing term that depends on the difference between the local and free stream values of total enthalpy. The fourth-order dissipative terms are needed to eliminate nonlinear instabilities when accelerating convergence using a local time step.

3.2.2   Viscous-Inviscid Interaction Using Semi-Inverse Coupling

When the Euler equations are used to compute the inviscid flow field the coupling requires momentum and enthalpy sources in addition to the mass sources. Johnston and Sockol [75], and Murman and Bussing [76] pointed out this information at about the same time. Thomas [74] followed the approach of Johnston and Sockol to achieve the viscous-inviscid interaction. Thomas modified the normal momentum relation by Rizzi [77] to include surface porosity for the pressure on the surface. In the present study the matching conditions are derived for the case with suction following Johnston and Sockol [75].

Coupling Method

The matching procedure adopted here is similar to that proposed by Johnston and Sockol [75] and is discussed here very briefly. The inviscid and the viscous solutions are matched on the surface.

The Euler equations for steady two-dimensional flow can be written as

$$\frac{\partial F}{\partial x} + \frac{\partial G}{\partial y} = 0 \qquad (3.13)$$

where

$$F = \begin{bmatrix} \rho u \\ \rho u^2 + p \\ \rho u v \\ u(e + p) \end{bmatrix} \quad ; \quad G = \begin{bmatrix} \rho v \\ \rho u v \\ \rho v^2 + p \\ v(e + p) \end{bmatrix} \qquad (3.14)$$

The steady Navier-Stokes equations can be written as

$$\frac{\partial f}{\partial x} + \frac{\partial g}{\partial y} = 0. \qquad (3.15)$$

In the defect formulation to be presented, the components of f and g are not needed. Integrating Eqs. (3.13) and (3.15) from y = 0 to y = δ, one obtains

$$G_\delta - G_0 = - \frac{\partial}{\partial x} \int_0^\delta F \, dy \qquad (3.16)$$

$$g_\delta - g_0 = - \frac{\partial}{\partial x} \int_0^\delta f \, dy \qquad (3.17)$$

By noting that, outside the boundary layer, the G and g vectors coincide, one can combine Eqs. (3.16) and (3.17) to obtain

$$G_0 = g_0 + \frac{\partial}{\partial x} \int_0^\delta (f - F) dy \qquad (3.18)$$

Now representing the Navier-Stokes solution by a composite function of the type

$$f = f_c = F + f_b - F_0 \qquad (3.19)$$

where f_b is the boundary-layer solution, Eq. (3.18) reduces to

$$G_0 = (g_b)_0 - \frac{\partial}{\partial x} \int_0^\delta (F_0 - f_b) dy \qquad (3.20)$$

It should be noted that only the value of F at the wall is needed and specific variation of F in the boundary layer is not necessary.

From Eq. (3.14) we can evaluate the values of the vector G. The first term of G is expressed as

$$(\rho v)_0 = (\rho_b v_b)_0 + \frac{\partial}{\partial x} \int_0^\delta [(\rho u)_0 - \rho_b u_b] dy \qquad (3.21)$$

Using the definition of displacement thickness Eq. (3.21) can be written as

$$(\rho v)_0 = \frac{d}{dx} [(\rho u)_0 \delta^*] + (\rho_b v_b)_0 \qquad (3.22)$$

The second term of the vector G is written as

$$(\rho u v)_0 = (\rho_b v_b u_b)_0 - \tau_0 + \frac{\partial}{\partial x} \int_0^\delta [(\rho u^2 + p)_0 - (\rho_b u_b^2 + p_b)] dy$$

By considering the pressure from the boundary-layer solution to be equal to the pressure from Euler solution and using the definition for the

momentum thickness, Eq. (3.22) can be written as

$$(\rho uv)_0 = -\tau_0 + \frac{d}{dx}\left[(\rho u)_0(\delta^* + \theta)\right] \qquad (3.23)$$

To evaluate the third term of G the pressure at the wall was determined by Thomas [74] using the Rizzi's normal momentum relation [77]. The surface porosity term was included in this analysis. Different interpolation relations to obtain pressure on the body from the adjacent cells are suggested by Thomas [74]. In this study some of these relations are used to check the convergence rate and the accuracy of the results. The fourth term of vector G can be written as

$$\left((e + P)v\right)_0 = \left[(e + P)v - u\tau\right]_b$$

$$+ \frac{\partial}{\partial x} \int_0^{\delta} \left\{\left[(e + p)u\right]_0 - \left[(e + p)u\right]_b\right\} dy \qquad (3.24)$$

With the approximation that the total enthalpy from the boundary layer is equal to the Euler solution value, Eq. (3.24) becomes

$$\left[(e + p)v\right]_0 = \left[(e + p)v\right]_b + H_0 \frac{d}{dx}\left[(\rho u)_0 \delta^*\right]$$

$$\rho v H_0 = (\rho H v)_b + H_0 \frac{d}{dx}\left[(\rho u)_0 \delta^*\right] \qquad (3.25)$$

This is an identity. As can be noted from (3.22) and (3.23), only the wall values are needed from the Euler solution and they can be obtained easily once the boundary-layer solution is obtained.

Wake Relation

In the wake the boundary-layer quantities are evaluated along the wake center line for upper and lower surfaces separately. The difference in the mass, momentum, and energy fluxes is applied as the boundary condition to the inviscid flow. In this study, neither the wake curvature effect nor the strong interaction near the trailing edge are taken into consideration. The computational mesh needs to be recomputed periodically to take the curvature effect into account.

Viscous-Inviscid Coupling

The viscous-inviscid interaction is achieved through a semi-inverse coupling. This technique was developed by Carter [78] for subsonic flows and has been used for transonic flows by Whitfield et al. [73], Le Balleur [67], and Thomas [74]. The inviscid algorithm is advanced 100 time steps to obtain an approximate pressure distribution around the airfoil. Then the inverse boundary-layer equations are solved using a specified displacement thickness distribution. Initially, this distribution is that of a flat plate. The velocity at the edge of the boundary layer is calculated at all the grid points on the airfoil and along the wake center line. Then the semi-inverse coupling compares the velocities at the edge of the boundary layer obtained from viscous and inviscid solutions. Then the initial distribution of the boundary-layer thickness is updated using the relation

$$(\delta^*)_{new} = (\delta^*)_{old}\left[1 + \omega\left(\frac{u_{e,v}}{u_{e,i}} - 1\right)\right] \qquad (3.26)$$

where $u_{e,v}$ is the boundary-layer edge velocity computed from the inverse intergral method, $u_{e,i}$ is the edge velocity from the inviscid solution, and ω is a relaxation parameter.

By using the new boundary-layer thickness distribution, the boundary condition to the inviscid flow is computed by Eqs. (3.22) - (3.25). Then, the inviscid algorithm is advanced in time with this new boundary condition near the wall. The inverse boundary-layer equations are solved after every 20 inviscid cycles from then on and the boundary conditions are updated. When there is no appreciable change in the lift or the boundary-layer thickness distribution, the solution is considered to be converged and the calculations are ended.

Suction

The reduction in drag is an order of magnitude from the turbulent boundary layer to laminar boundary layer. Therefore, large extents of laminar flow are desirable to increase the aircraft performance.

The laminar boundary layer cannot undergo large adverse pressure gradients and the flow separates resulting in rapid thickening of the boundary layer; this increases the drag. To avoid this undesirable effect, suction can be applied before the flow separation point to keep the flow attached all along the airfoil.

Location of Suction

The velocity profile parameter 'a' is proportional to the velocity gradient near the wall. The value of 'a' is zero at separation. A specified amount of suction is applied when the value of 'a' falls below certain value depending on the airfoil under

consideration. The value of the suction parameter is increased at the next location if the value of 'a' is still below the specified value. When there is a negative pressure gradient or when the value of 'a' is higher than a specified value, the suction parameter is decreased.

With the above procedure, the flow separation is avoided and attached flow condition is maintained all along the airfoil. The amount of suction thus calculated is close to the minimum amount.

Chapter **4**

RESULTS AND DISCUSSION

Results have been obtained for different airfoils by employing the direct and inverse boundary-layer procedures for laminar and turbulent flows. Specific results were obtained for various cases with and without suction in the boundary layer. Results of calculations for the 6% circular arc and LFC-73-06-135 airfoils are presented in Sec. 4.1. These results were obtained for laminar flows using the direct boundary-layer equations. In Sec. 4.2 results are presented for the King Cobra airfoil and the modified NACA 66-012 airfoil. The flow conditions are selected such that the results can be compared with the experimental data. Also results for DESB-154 and LFC-73-06-135 airfoils are presented for attached flow conditions. Results for the laminar inverse boundary-layer equations coupled with the Euler equations are presented in Sec. 4.3 for the NACA-0012 airfoil and the RAE-2822 airfoil. Using the same approach, results were calculated for the turbulent boundary-layer flows with and without suction; these are presented in Sec. 4.4.

4.1 Laminar Direct Boundary-Layer Solutions Without Suction

Results of calculations at supercritical freestream Mach numbers are presented for a 6% circular arc and LFC-73-06-135 airfoils. Flow

conditions were chosen to enable comparisons with available experimental data.

The viscous results were calculated in terms of boundary-layer quantities in a transformed incompressible plane. Figure 4.1 gives the boundary-layer displacement thickness throughout a 6% circular arc airfoil at $M_\infty = 0.868$ and $Re_\infty = 6.9 \times 10^4$, which agrees very well with similar results reported elsewhere [79]. The thickening of the boundary layer in the forward portion follows a similar trend as that found by Schubauer, using the Karman-Polhausen method [80]; however, the present method gives a far more realistic δ^* distribution pattern in the rear portion.

The corresponding distribution of the boundary-layer shape factor H and the velocity profile parameter, a, are presented in Figs. 4.2 and 4.3, respectively. The boundary layer is practically, but not exactly, of Blasius type in the leading-edge region and varies slightly throughout the forward portion of the airfoil. It remains unseparated through the embedded supersonic region although the viscous-inviscid interaction becomes strong after $x = 0.395$. The separation point is found when $a = 0$ which corresponds to zero shear stress at the wall.

The boundary layer remains separated over the rear of the airfoil where small adverse pressure gradients are generated by continuous compression of the outer subsonic flow. This is a physical feature of the transonic viscous-inviscid interaction since by compression the flow ought to return almost to the free-stream value downstream. After the trailing edge there is a wake reversed flow and then a forward flow to match the downstream conditions. The location of the rear stagnation point agrees well with that found by Klineberg and Steger [39], and by
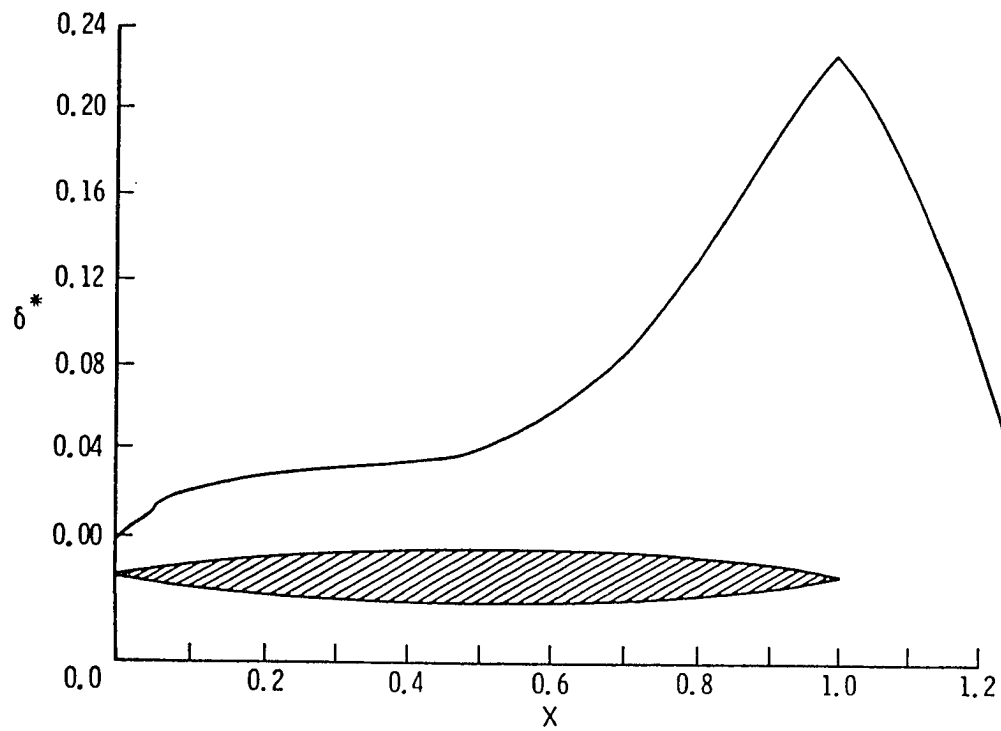
Fig. 4.1 Boundary-layer displacement thickness for a 6% circular arc airfoil at $M_\infty = 0.868$ and $Re = 6.9 \times 10^4$.

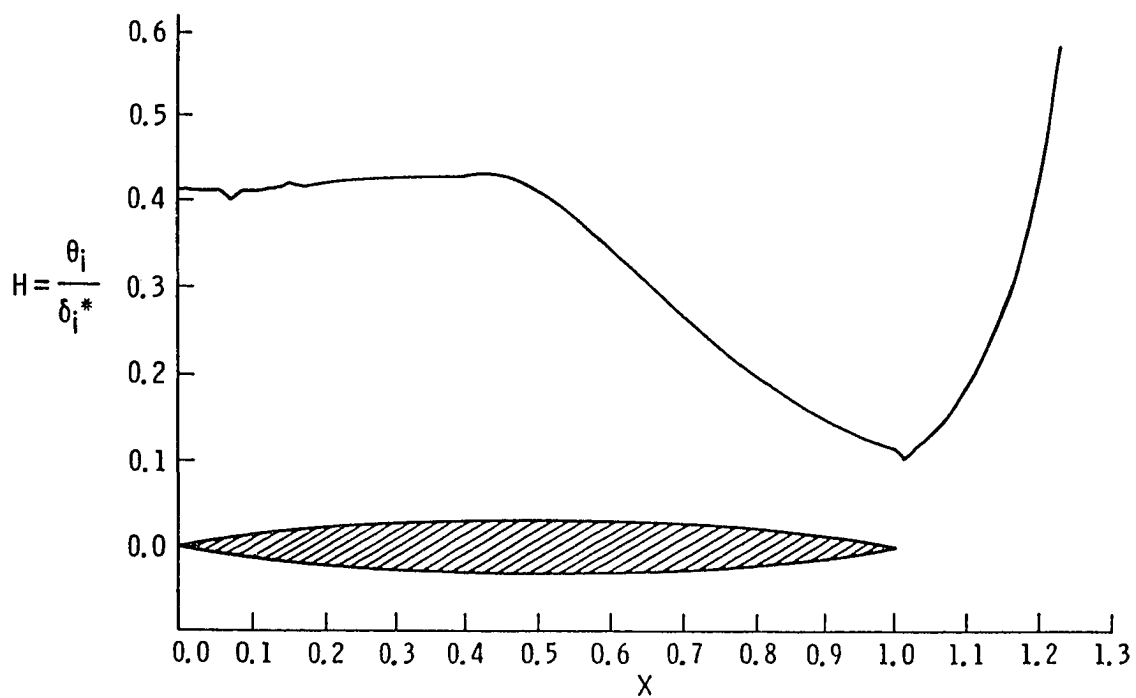Fig. 4.2 Boundary-layer shape factor H for a 6% circular arc airfoil at $M_\infty = 0.868$ and $Re = 6.9 \times 10^4$.
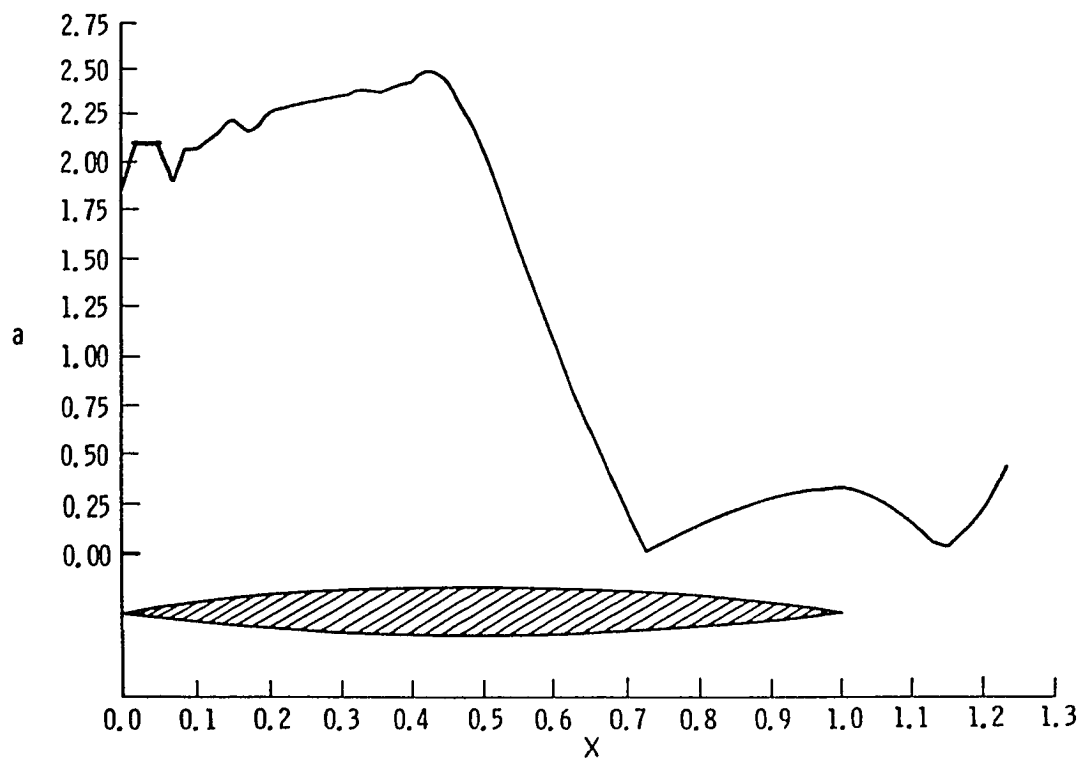
Fig. 4.3   Velocity profile parameter for a 6% circular arc

airfoil at $M_\infty = 0.868$ and $Re = 6.9 \times 10^4$.

Tai [79] under similar flow conditions. Computed results for the 6% circular arc airfoil compare very well with the laminar experimental data of Collins and Krupp [81] as presented in Fig. 4.4, not only in pressure distribution but also in separation point. The small difference in free-stream Mach number and Reynolds number between theory and experiment was selected deliberately to offset wind-tunnel inter-ference effects [82].

There is no referenceable experimental data available at the present time for supercritical airfoils for which the boundary layer remains laminar over most of the airfoil. Of course, plenty of experimental data are available for many airfoils with turbulent boundary layers. For this reason it was decided to compare the theo-retical predictions of the present method to that of some other existing methods, such as Carlson's TRANSEP [83], to judge its reliability and accuracy. Based on the experience with the ongoing swept supercritical LFC airfoil experiment in the Langley 8-Foot Transonic Pressure Tunnel [84], it is expected that the flow will remain laminar over an extensive chordwise length of the LFC-73-06-135 airfoil for $M_\infty = 0.75$, $Re_c = 8 \times 10^6$, and $\alpha = -0.09°$. Therefore, this airfoil and these flow conditions were chosen to calculate viscous results using both TRANSEP and the present method, along with the inviscid results using Carlson's TRANDES [85]. Figures 4.5 and 4.6 show the pressure distribution obtained from these three methods. The viscous results obtained from these two methods are in very good agreement with each other except for a few deviations which were expected. For example, the c_p values for the upper surface obtained from TRANSEP are slightly lower (i.e., more negative) than those from the present method in the region lying between
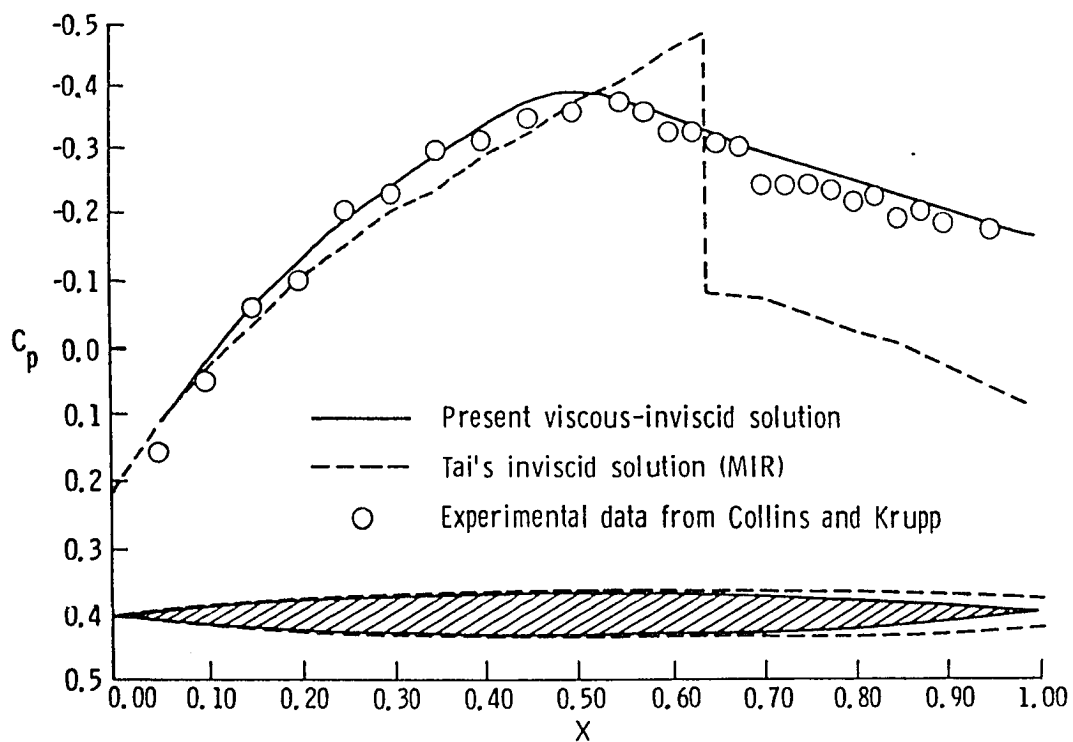
Fig. 4.4 Pressure distribution over a 6% circular arc airfoil

at $M_\infty = 0.868$, $\alpha = 0^\circ$, and $Re = 6.9 \times 10^4$.

Legend within figure:
- Present viscous-inviscid solution
- Tai's inviscid solution (MIR)
- O Experimental data from Collins and Krupp

Fig. 4.5 Pressure distribution on the upper surface of a swept

supercritical LFC-73-06-135 airfoil at $M_\infty = 0.750$,

$\alpha = -0.09°$, and $Re = 8 \times 10^6$.

Fig. 4.6 Pressure distribution on the lower surface of a swept supercritical LFC-73-06-135 airfoil at $M_\infty = 0.750$, $\alpha = -0.09^\circ$, and $Re = 8 \times 10^6$.

39% through 76% of the chordwise length. The starting position of the adverse pressure gradient is located at 50% and 46% of the chord, respectively, as predicted by TRANSEP and the present method. The present method predic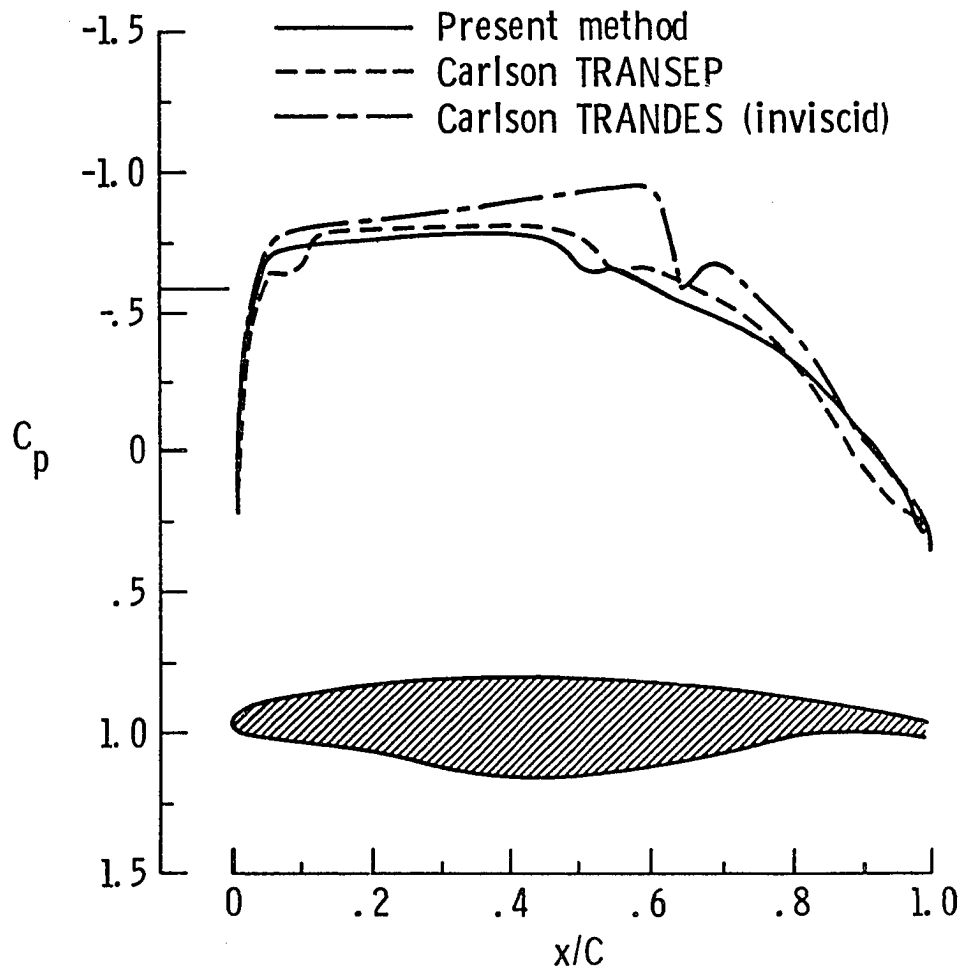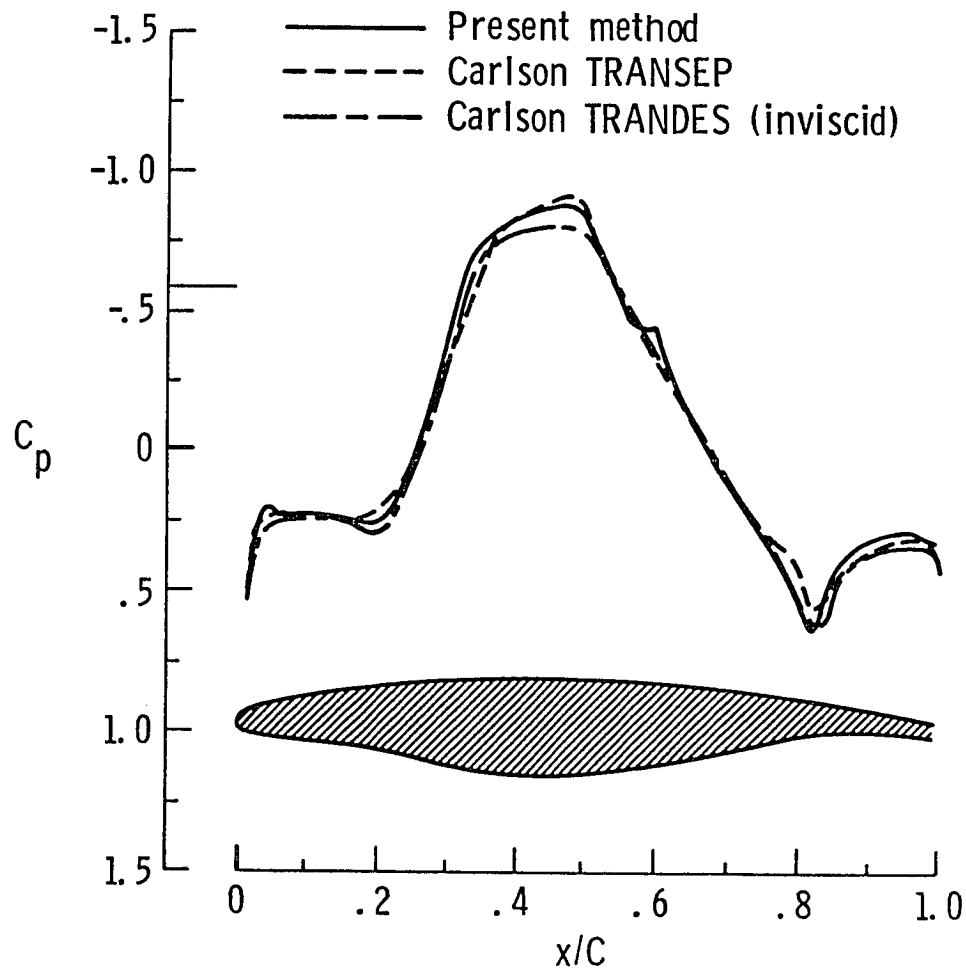ts flow separation at $x = 0.665$, whereas the flow remains attached over the airfoil according to TRANSEP. Because of the strong interaction formulation modeled in the present method, the flow separates, whereas it remains attached due to weak interaction formulation modeled in TRANSEP. Also, the displacement thickness of the laminar boundary layer increases more rapidly through the shock than that of turbulent boundary layer [86] and this may cause laminar separation. The pressure rises more rapidly for turbulent than for laminar boundary layers [87,88]. From 80% of the chord to the trailing edge, the c_p values predicted by TRANSEP are higher (i.e., more positive) than those obtained from the present method. This is true because the boundary layer over the last 20% of the chord is definitely turbulent, whereas in the present method the boundary layer over the entire chord length always remains laminar. Thus, the theoretical results calculated from this method conform very well to the findings of [86-88].

4.2 Laminar Direct Boundary-Layer Solutions With Suction

Results of calculations are presented for modified NACA 66-012 [89], DESB 154 [90], King Cobra [91], and LFC-73-06-135 [92] airfoils. The airfoil NACA 66-012 was chosen to enable comparison of the calculated result with experimental data available from [89]. The DESB 154

and King Cobra airfoils retain laminar flow over an extensive chordwise length (approximately 70% and 65%, respectively). These two airfoils were chosen because of extensive laminar flow which will be more appropriate to test the accuracy and reliability of the present method. Furthermore, experimental data available for a King Cobra airfoil for the no suction case permits comparison of the computed results under similar conditions. Since the method has been developed for super-critical airfoils, LFC-73-06-135 airfoil designed at NASA Langley was selected for comparison.

The viscous results were calculated in terms of boundary-layer quantities in a transformed incompressible plane. Figure 4.7 gives the boundary-layer displacement thickness on the upper surface of a natural laminar flow airfoil (DESB 154 at $M_\infty = 0.4$, Re $= 10 \times 10^6$, and $\alpha = -0.97^\circ$) for different values of the suction parameter ε. It was found that $\varepsilon = 0.015$ was the minimum amount of suction that kept the flow attached all the way to the trailing edge. The suction was started at 65% of the chord length and was maintained up to the trailing edge. It should be pointed out here that the flow separates at about 70% of the chord length for the same flow conditions if the suction is not applied, i.e., $\varepsilon = 0$, as shown by the present theoretical computations as well as by those in [90]. It is further seen that the thickening of the boundary layer and hence, the overall viscous effects can be controlled easily by varying the magnitude of the suction parameter ε.

The corresponding distribution of the velocity profile parameter a is presented in Fig. 4.8. There are minimal fluctuations in its values until the point of separation (in the absence of suction) is approached when it suddenly increases and remains high or drops down
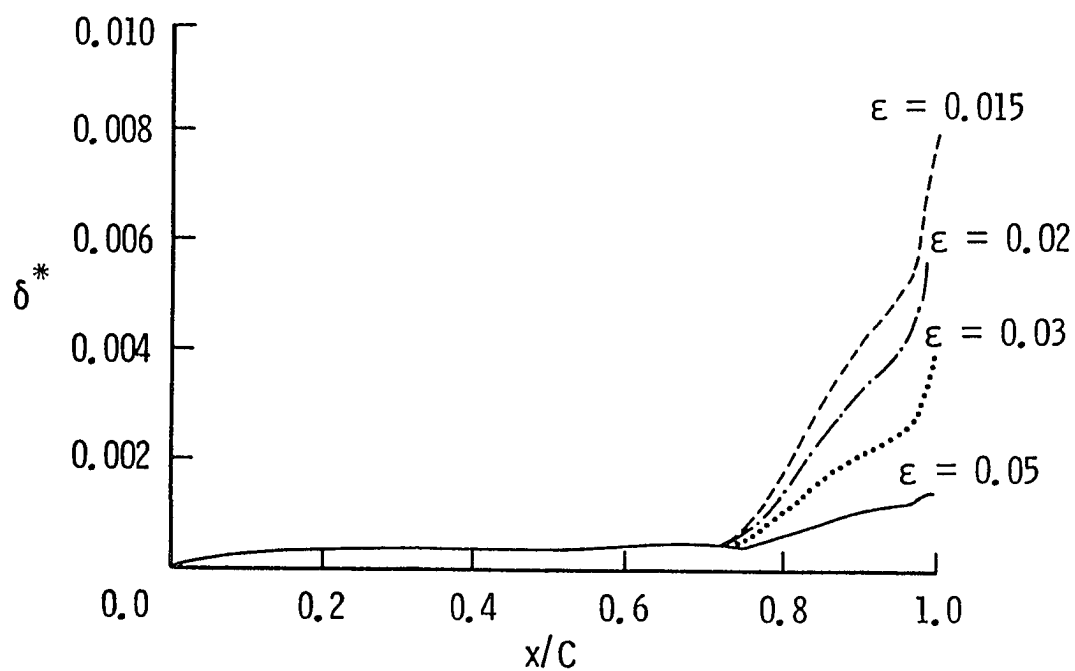
Fig. 4.7 Boundary-layer displacement thickness for DESB 154
airfoil at $M_\infty = 0.4$, Re = 10 x 10^6, $\alpha = -0.97°$, for
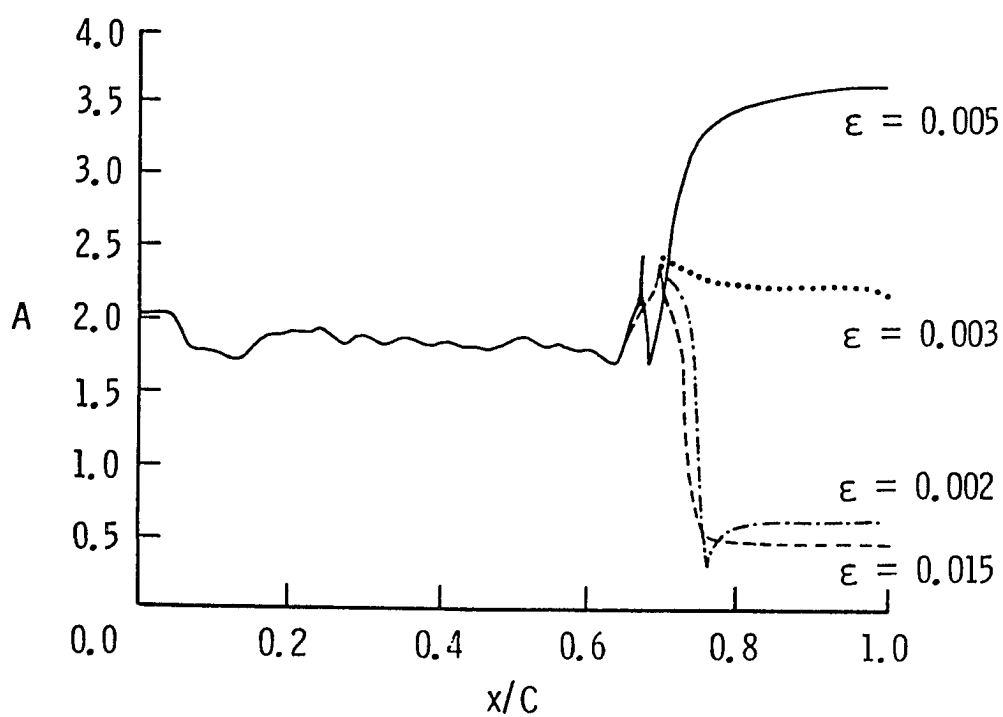different values of the suction parameter ϵ.

Fig. 4.8 Velocity profile parameter for DESB 154 airfoil at

$M_\infty = 0.4$, Re = 10 × 10^6, $\alpha = -0.97°$ for different values

of the suction parameter ε.

depending on the amount of suction applied. The lowest value, a = 0, occurs at the point of separation and corresponds to zero shear stress at the wall.

Figure 4.9 shows the pressure distribution over a DESB 154 airfoil obtained by using the Carlson's TRANDES (Inviscid) method and the present method with suction. These theoretical results compare very well as expected. The C_p values for the upper surface obtained from the TRANDES (Inviscid), when there is no boundary layer, are slightly lower (i.e., more negative) than those from the present method with suction, when there is a very thin boundary layer. The point of sudden rise (i.e., more positive) in C_p value occurs at 0.71c and 0.68c, respectively.

Figures 4.10 and 4.11 give the pressure distribution over the King Cobra airfoil without and with suction, respectively. The computed results in Fig. 4.10 compare very well with the experimental data reported in [91], not only in pressure distribution but also in separation point. The suction for the King Cobra airfoil was started at 60% of the chord length and was maintained up to the trailing edge. It should be mentioned here that the flow separates at about 65% of the chord length for the same flow conditions if the suction is not applied, i.e., $\varepsilon = 0$, as shown by the theoretical computations as well as experimental data.

Figure 4.12 shows the pressure distribution over a swept LFC airfoil (modified NACA 66-012) obtained from the present method with suction. The computed results compare very well with the experimental data, also with suction, reported in [89].
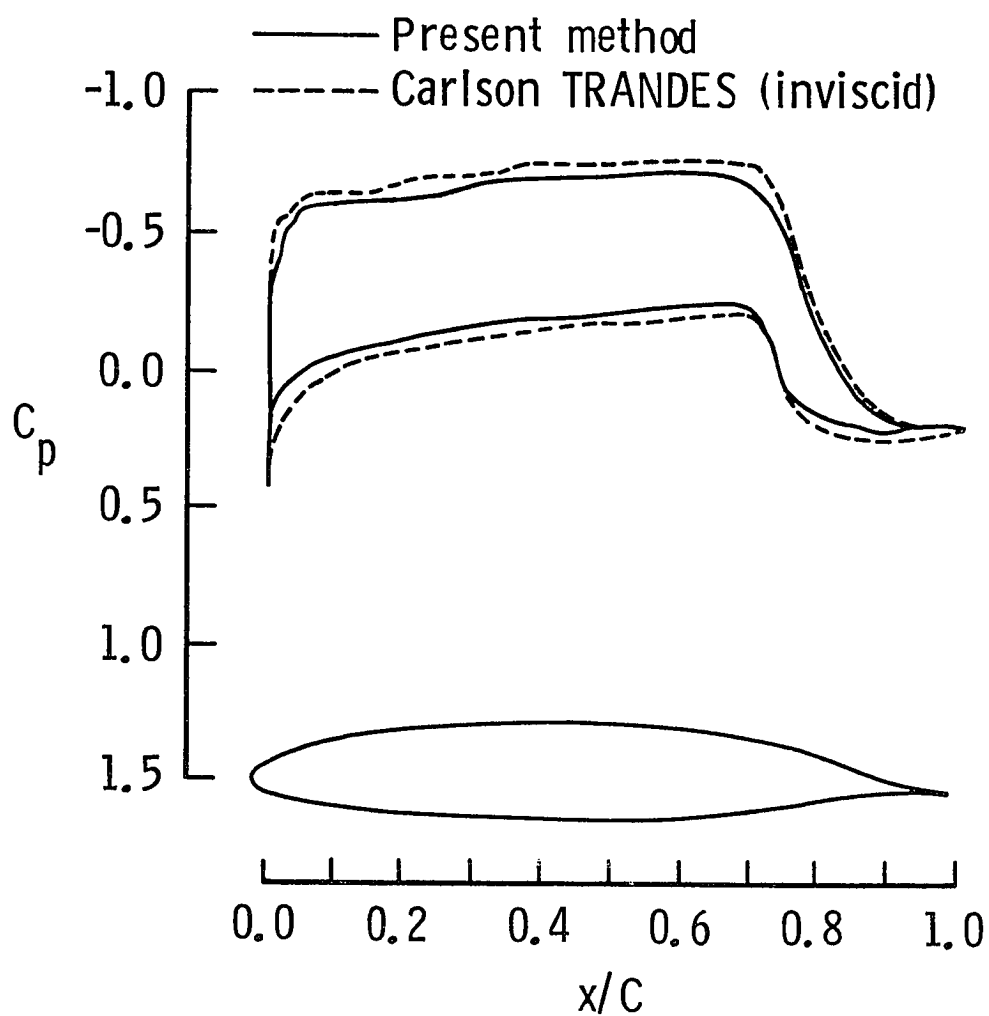
Fig. 4.9 Pressure distribution on the upper and lower surfaces of
DESB 154 airfoil at $M_\infty = 0.4$, Re $= 10 \times 10^6$, $\alpha = -0.97°$,
$\varepsilon = 0.015$.
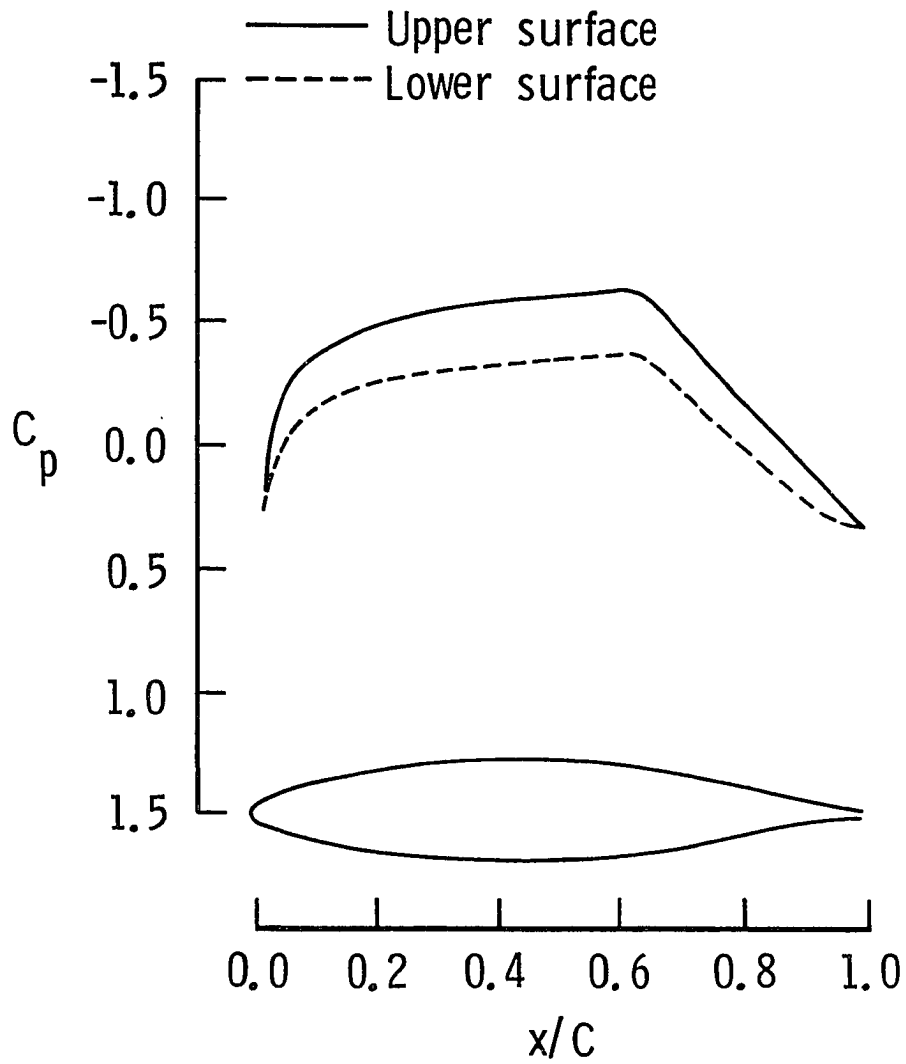
Fig. 4.10 Pressure distribution over King Cobra airfoil at

$M_\infty = 0.4$, $\alpha = 1^\circ$, $Re = 10 \times 10^6$ and $\varepsilon = 0$.
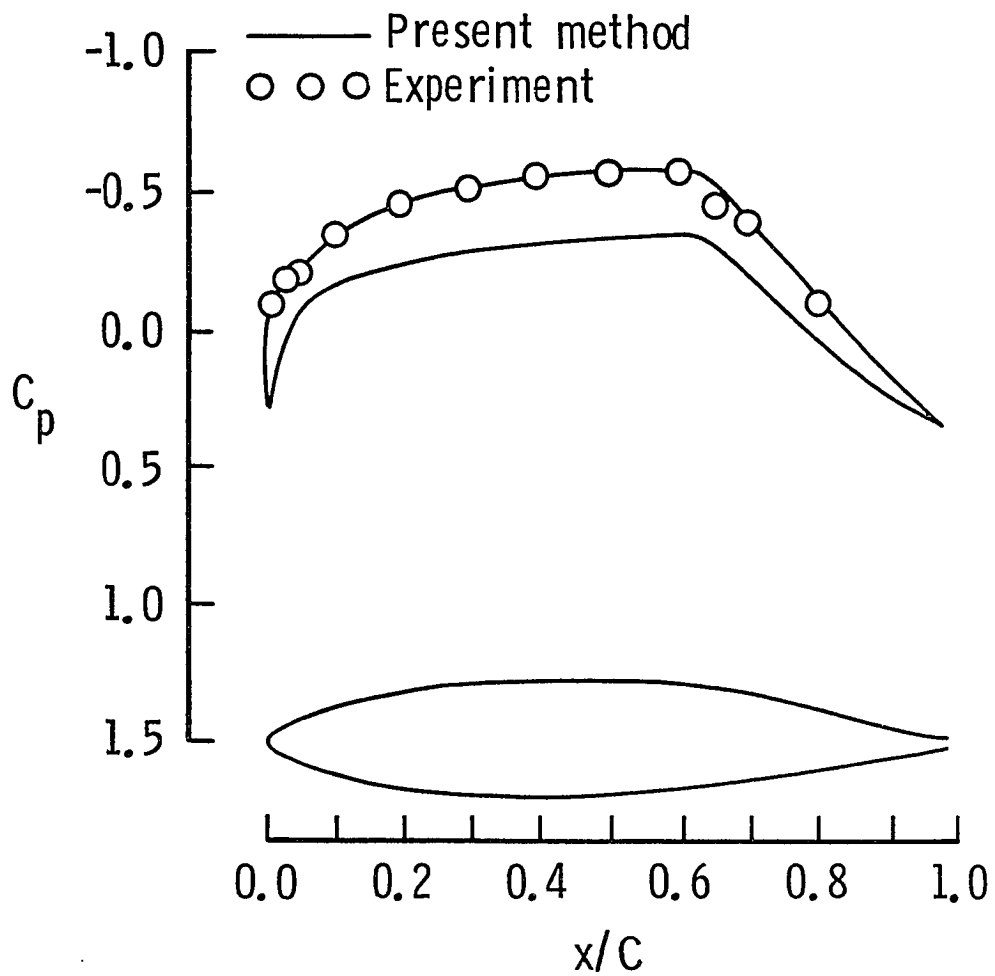
Fig. 4.11 Pressure distribution on the upper and lower surfaces of King Cobra airfoil at $M_\infty = 0.4$, Re $= 10 \times 10^6$, $\alpha = 1^\circ$, $C_\ell = 0.199$, $\varepsilon = 0.002$ for upper surface obtained from the present program.
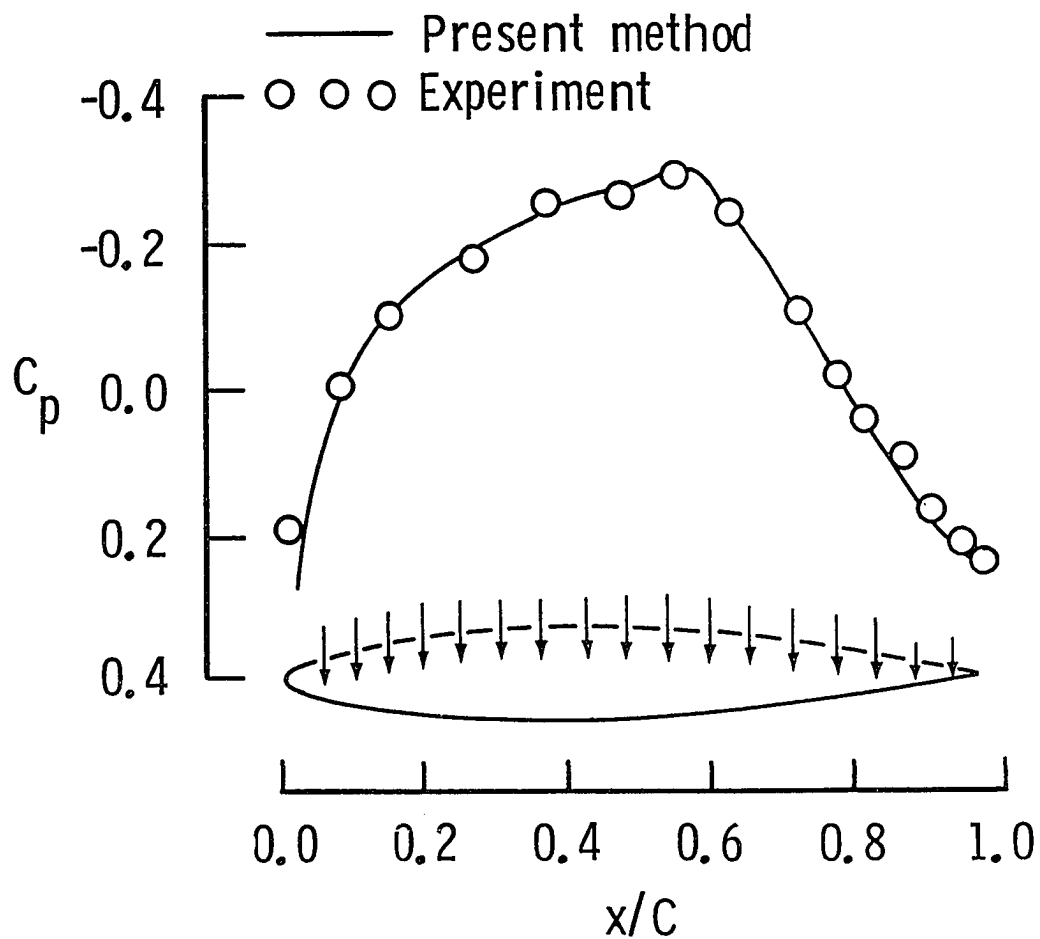
Fig. 4.12. Pressure distribution on the upper surface of a modified
NACA 66-012 airfoil at $M_\infty = .12$, $\alpha = 0°$, $Re = 14 \times 10^6$,
and $.003 \leqslant \varepsilon \leqslant .015$.

There does not exist any computational method which solves strong inviscid-laminar viscous interactions by solving Euler equations in the shock-dominated region and where the boundary layer is optimally sucked such that boundary-layer instability and separation do not occur. The pressure distributions over the LFC-73-06-135 supercritical airfoil calculated from Carlson's TRANDES (Inviscid) and the present method are compared to show the effect of suction and the formulation of the viscous-inviscid model. The flow conditions were chosen to assure the existence of a shock on the upper surface of the airfoil. In the inviscid analysis, Fig. 4.13, the shock appears at 77% of the chord length. In the inviscid-viscous analysis with suction, Fig. 4.14, the shock becomes much weaker, moves upstream to 0.63c and the boundary layer remains attached. Figure 4.15 shows that C_p values calculated from the present method are consistently higher (i.e., more positive) by as much as up to 24.3%. This is expected due to effect of viscosity and the change of entropy across the shock which are accounted for in the present method. The results mentioned here for LFC-73-06-135 airfoil are in agreement with the findings of the swept supercritical LFC airfoil experiments conducted in the Langley 8-Foot Transonic Pressure Tunnel [93].

Fig. 4.13 Pressure distribution over a swept supercritical
LFC-73-06-135 airfoil at $M_\infty = 0.780$, $\alpha = 0°$, Re $= 10 \times 10^6$,
and $\varepsilon = 0$ obtained from Carlson's TRANDES (Inviscid).
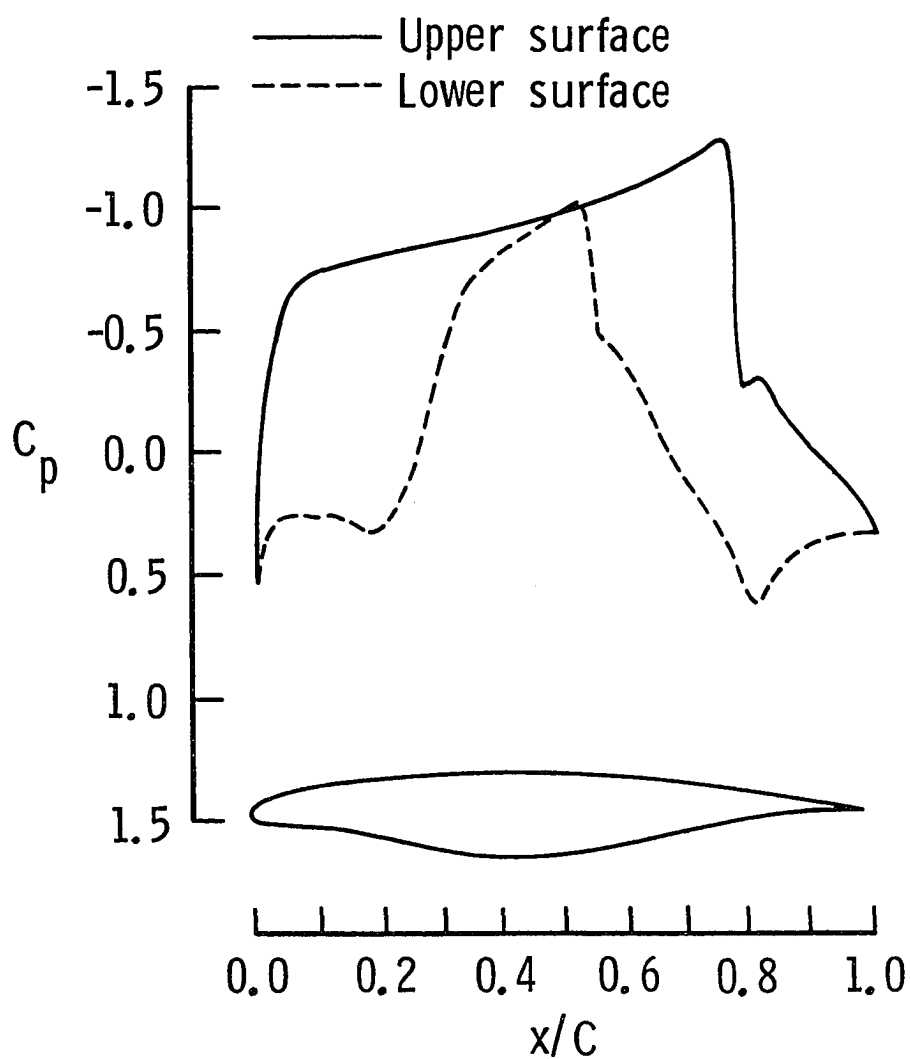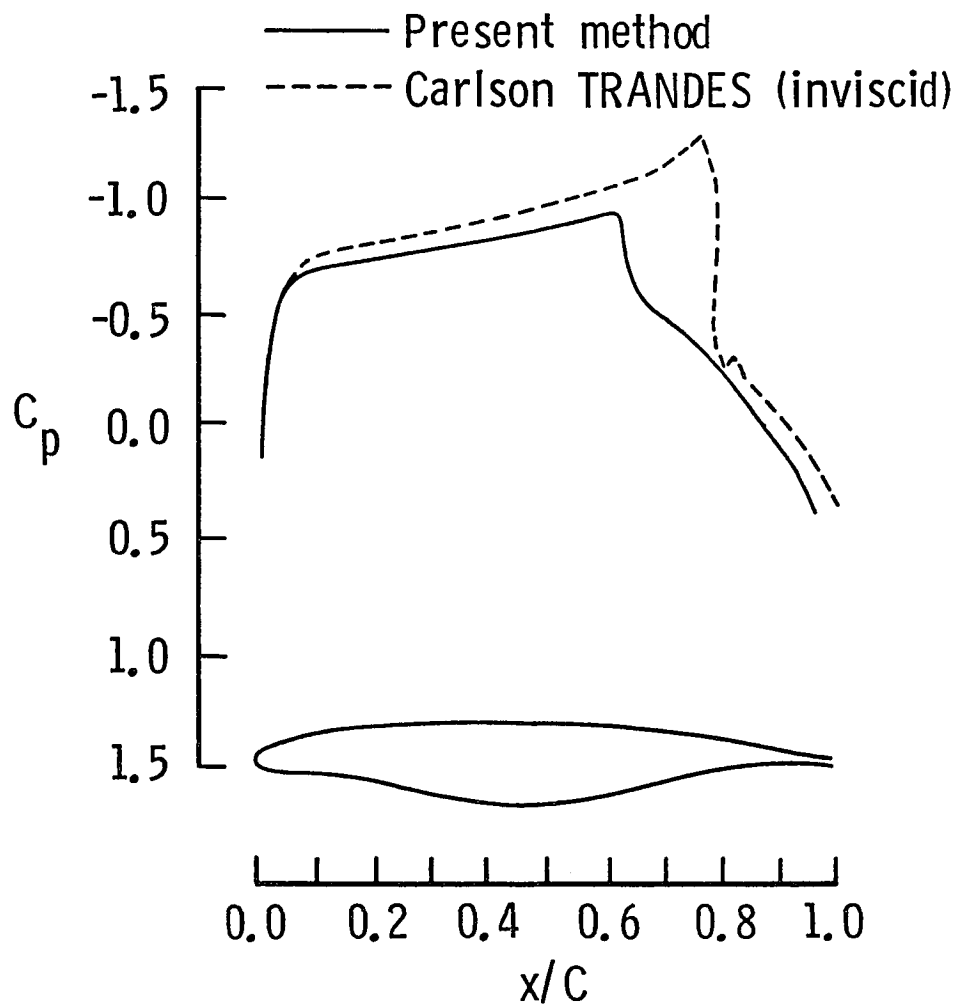
Fig. 4.14 Pressure distribution over a swept supercritical LFC-73-06-135 airfoil at $M_\infty = 0.780$, $\alpha = 0^\circ$, $Re = 10 \times 10^6$, $\epsilon = 0.035$ on the upper surface obtained from the present program.

Fig. 4.15 Pressure distribution on the upper surface of a

swept supercritical LFC-73-06-135 airfoil at

$M_\infty = 0.780$, $\alpha = 0°$, and $Re = 10 \times 10^6$.

4.3 Inverse Laminar Boundary-Layer Solutions

Results are presented in Fig. 4.16 for an RAE-2822 airfoil at subcritical condition. The free stream Mach number is 0.6 and the angle of attack is 2.57°. The inviscid flow calculations are performed by solving the unsteady Euler equations [72]. The viscous-inviscid interaction was started very close to the leading edge. A small amount of suction was required to keep the flow from separating near the leading edge. The pressure peak near the nose causes early transition to turbulent flow if suction is not applied. After the pressure minimum, the flow is continuously decelerated to match the downstream flow of the airfoil. The laminar flow is stable in this region and the flow remains attached all the way to the trailing edge. There is no need to apply suction after the nose peak. The boundary layer is thicker than in the case of a turbulent flow and the C_p values, are less negative along the airfoil.

Figure 4.17 illustrates results for the supercritical conditions. The free stream Mach number is 0.73 and the corrected angle of attack is 2.78°. This case corresponds to case 9 of the experiments conducted by Cook et al. [94]. In the experiments, the flow was tripped very close to the leading edge to produce a turbulent boundary layer. For laminar boundary layers the flow would separate at about 45% of the chord length. The suction was applied before the separation point to keep the flow attached. The amount of suction applied depends upon the velocity profile parameter a. The value of the suction parameter is increased or decreased based on whether the value of a is below or above a specified limit. This was an effort to apply only the minimum suction
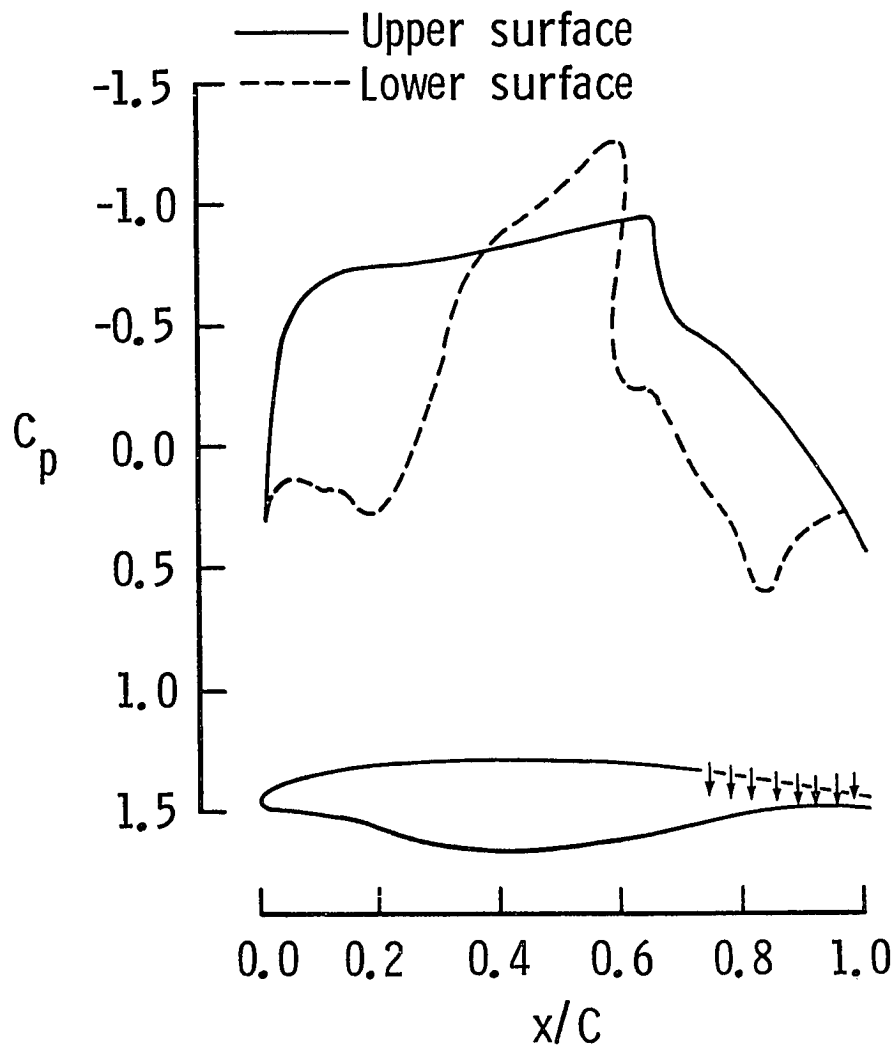
Fig. 4.16 Pressure distribution on the upper surface of RAE-2822

supercritical airfoil at $M_\infty = 0.6$, $\alpha = 2.57^\circ$, and

$Re = 6.5 \times 10^6$.
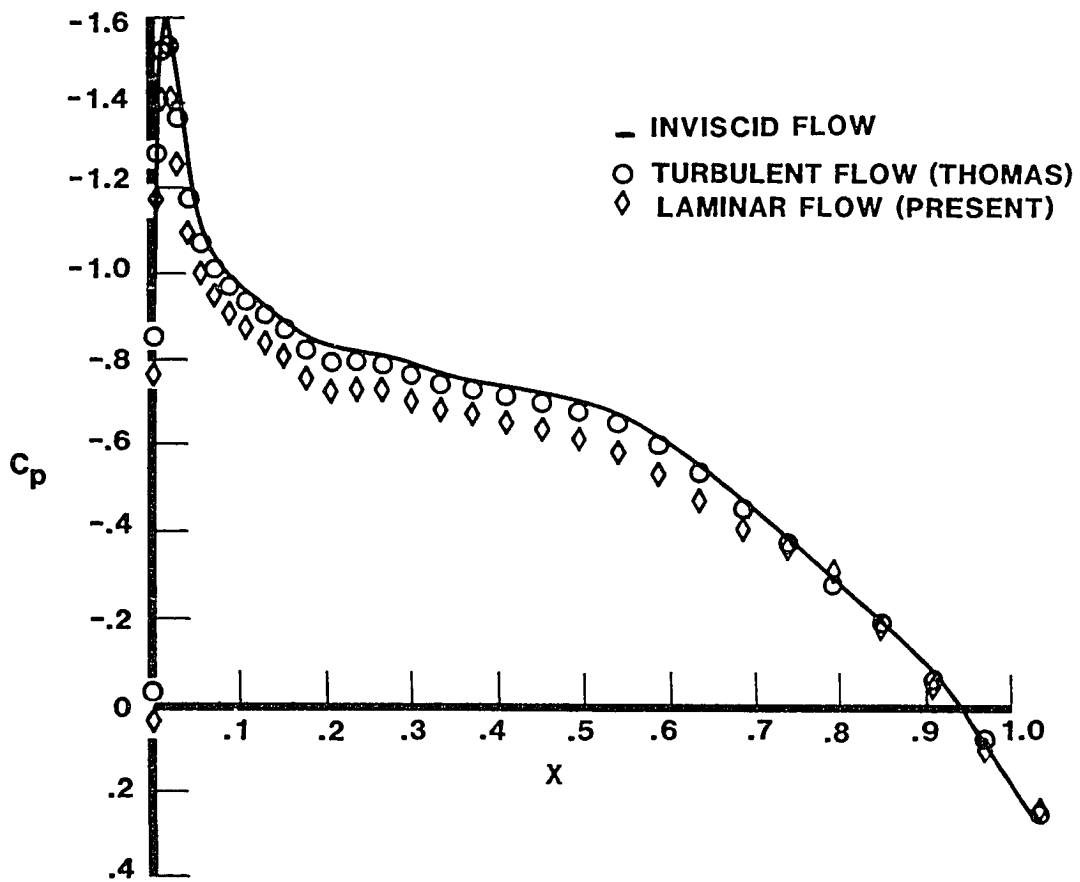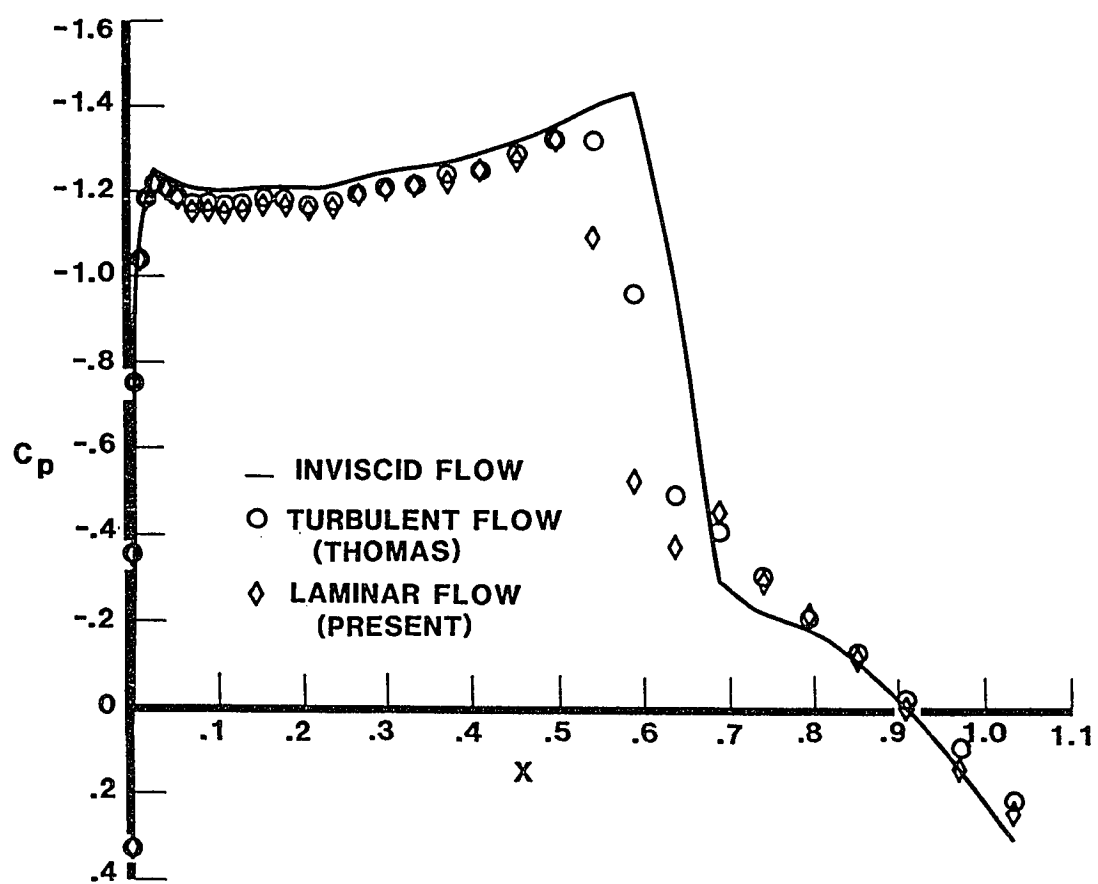
Fig. 4.17 Pressure distribution on the upper surface of RAE-2822
supercritical airfoil at $M_\infty = 0.73$, $\alpha = 2.78^\circ$, and
$Re = 6.5 \times 10^6$.

required rather than an arbitrary amount. The strength of the shock is reduced and moved forward because of the laminar boundary layer as compared to the inviscid flow calculations.

For NACA-0012 airfoil extensive experiments were conducted by Harris for subcritical to supercritical Mach numbers and for different values of the angle of attack [95]. However, in all these experiments the boundary layer has been tripped close to the nose to produce a turbulent boundary layer flow. Present results for transonic laminar flow are compared with these experimental data for a qualitative comparison. Results presented in Fig. 4.18 are for a Mach number of 0.758 and an angle of attack of 3.06°. The laminar viscous-inviscid interaction was started just ahead of the stagnation point at about 1% of the chord length on both the upper and lower surfaces. The location of the shock foot is at about 52% of the chord length according to the inviscid flow results. From the viscous-inviscid interaction calculations, it is noted at about 48% of the chord length. The suction was applied at 47.48% to maintain the laminar attached flow. A large amount of suction was required up to about 55% of the chord and after the shock, a relatively small amount of suction was sufficient to keep the flow attached. In the experiments the turbulent flow was separated at 34% of the chord, the shock strength was reduced considerably and moved forward in comparison with the present results. The suction was applied to produce a turbulent, attached boundary layer flow over this airfoil under similar conditions and those results are presented in the next section. The C_p values of both the experimental investigation and the present method are close to the inviscid results in the rear part of the airfoil where the flow has to match the subcritical conditions in the downstream region.

Fig. 4.18 Pressure distribution on the upper surface of NACA-0012

airfoil at $M_\infty = 0.758$, $\alpha = 3.06^\circ$, Re = 3.0 × 10^6.

Results are presented in Fig. 4.19 for an NACA-0012 airfoil at high angle of attack conditions. The free stream Mach number is 0.601 and the Reynolds number based on the chord length is three million. A correction to the angle of attack was applied to compare the results with the experiments [95]. It is evident from the Fig. 4.19 that there is a pressure peak in the forward portion of the airfoil and there is a pressure rise at about 17-20% of the chord. The experimental values are closer to the inviscid flow results in the peak region and the pressure rise region except near the end of the shock. The viscous-inviscid interaction was started at about 1% of the chord. Suction was applied to maintain laminar attached flow. After the shock not much suction is required. In comparison to the inviscid flow, the shock strength is reduced and the pressure wiggle is reproduced at the end of the shock. The coefficient of lift is 0.761 as compared to the turbulent value of 0.847.

4.4 Turbulent Boundary-Layer Results With Suction

Results are presented in Fig. 4.20 for the RAE-2822 airfoil at subcritical conditions. The free stream Mach number is 0.6 and the angle of attack is 2.57°. A correction to the angle of attack is made following the suggestions of Cook et al. [94]. The results are compared with the experimental data of Cook et al. [94] and with the theoretical results of Thomas [74]. The Reynolds number based on the chord length is 6.5 million. The viscous-inviscid interaction was started at about 15% of the chord on the lower surface and at 18% of the chord on the

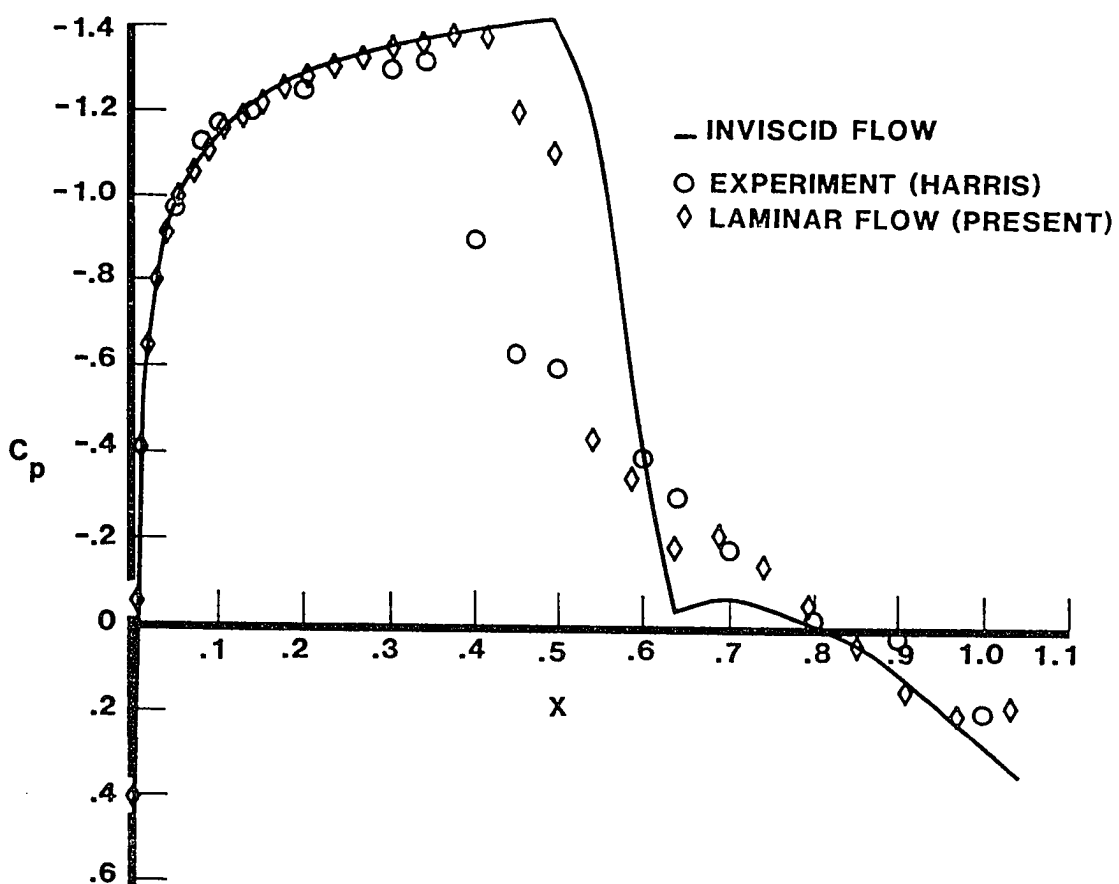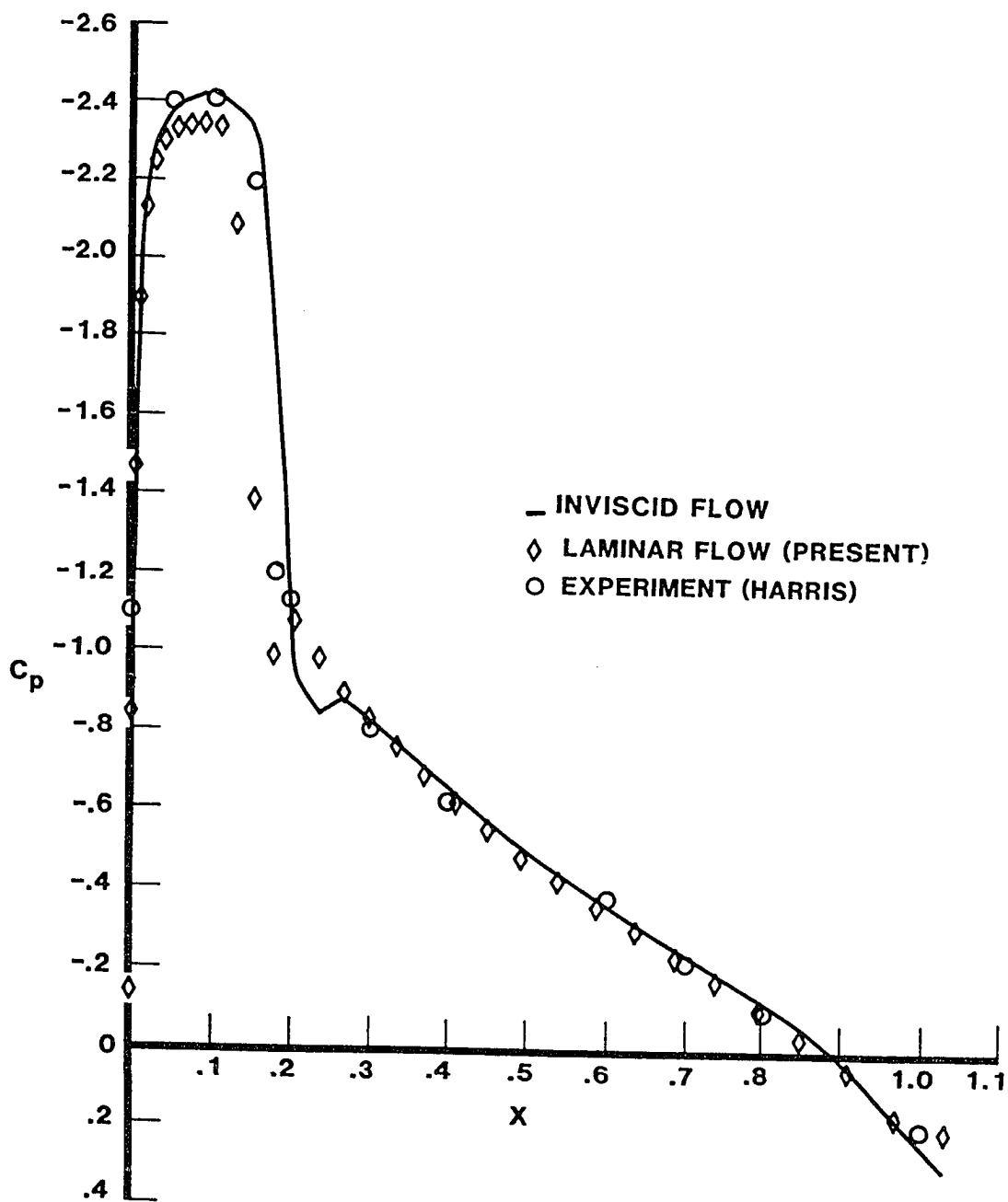Fig. 4.19 Pressure distribution on the upper surface of

NACA-0012 airfoil at $M_\infty = 0.758$, $\alpha = 5.85^\circ$,

$Re = 3 \times 10^6$.

Fig. 4.20 Pressure distribution on the upper surface of RAE-2822

supercritical airfoil at $M_\infty = 0.600$, $\alpha = 2.57^\circ$, and

$Re = 6.5 \times 10^6$.

upper surface. In the experiment the boundary layer has been tripped at these locations. The initial displacement thickness values correspond to the experimental data. The calculations were performed on a C-type mesh using 128 points along the airfoil and 30 points away from the airfoil. The boundary layer was iterated for every 20 cycles of the inviscid calculations (after the first 100 cycles). In the forward portion of the airfoil, where there is a pressure peak, results obtained from the present calculations agree closely with the experimental values. The turbulent flow remains attached until the trailing edge and there is no suction applied in this case. The lift coefficient, C_ℓ, values were found to be 0.71 and 0.65 for inviscid and turbulent flows, respectively. The results for the RAE-2822 airfoil for supercritical conditions are illustrated in Fig. 4.21. The free stream Mach number is 0.73, the corrected angle of attack is 2.78°, and the Reynolds number based on the chord length is 6.5 million. These conditions correspond to case 9 of Ref. 94. These calculations were also obtained using a C-type mesh with 128 × 30 points. The grid was highly stretched away from the airfoil until the change in the lift coefficient was small [74]. The inviscid lift coefficient showed no appreciable change after 600 time steps. The extent of reduction in the maximum residual is of fourth-order. After the first 100 time steps the boundary layer was interacted for every five time steps. Although this increases the computational time, the results were more accurate. Because of frequent updating, the viscous-inviscid interaction process is closer to the strong interaction conditions. The interaction was started at about 18% of the chord with the initial displacement thickness values from the experiment [94]. For comparison, the equilibrium dissipation model of
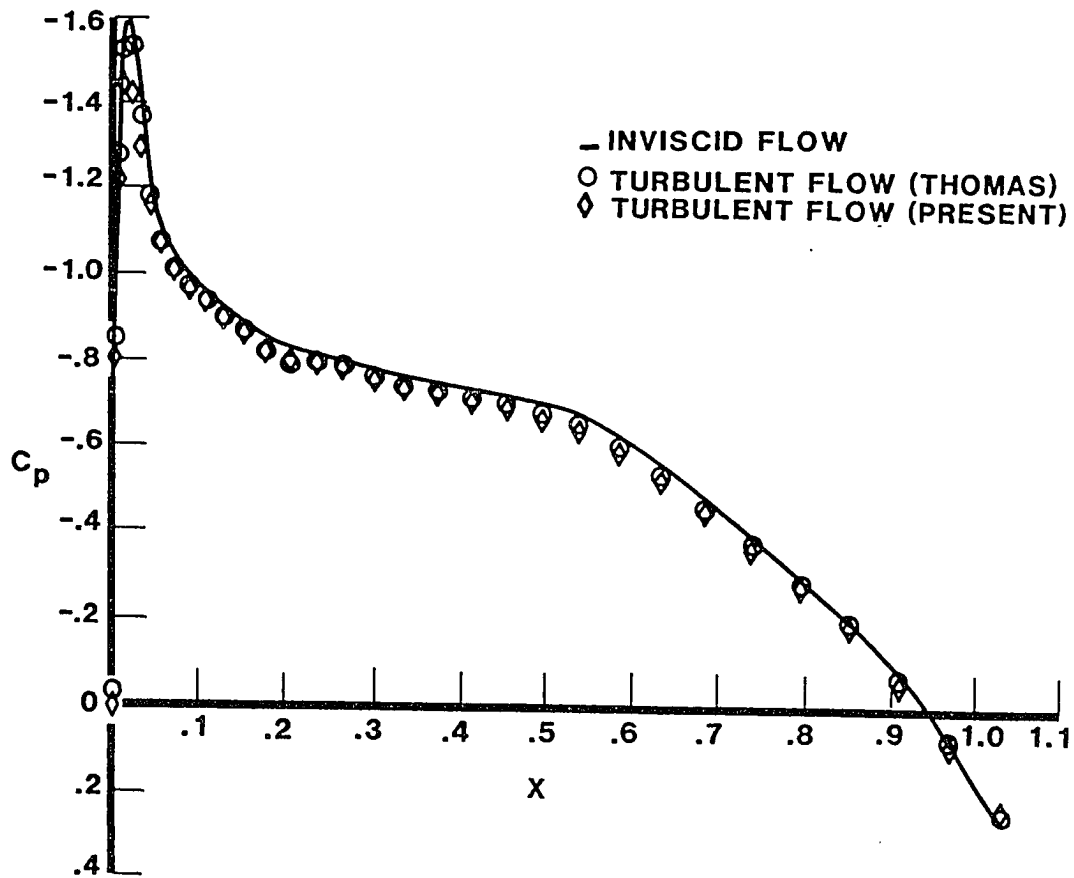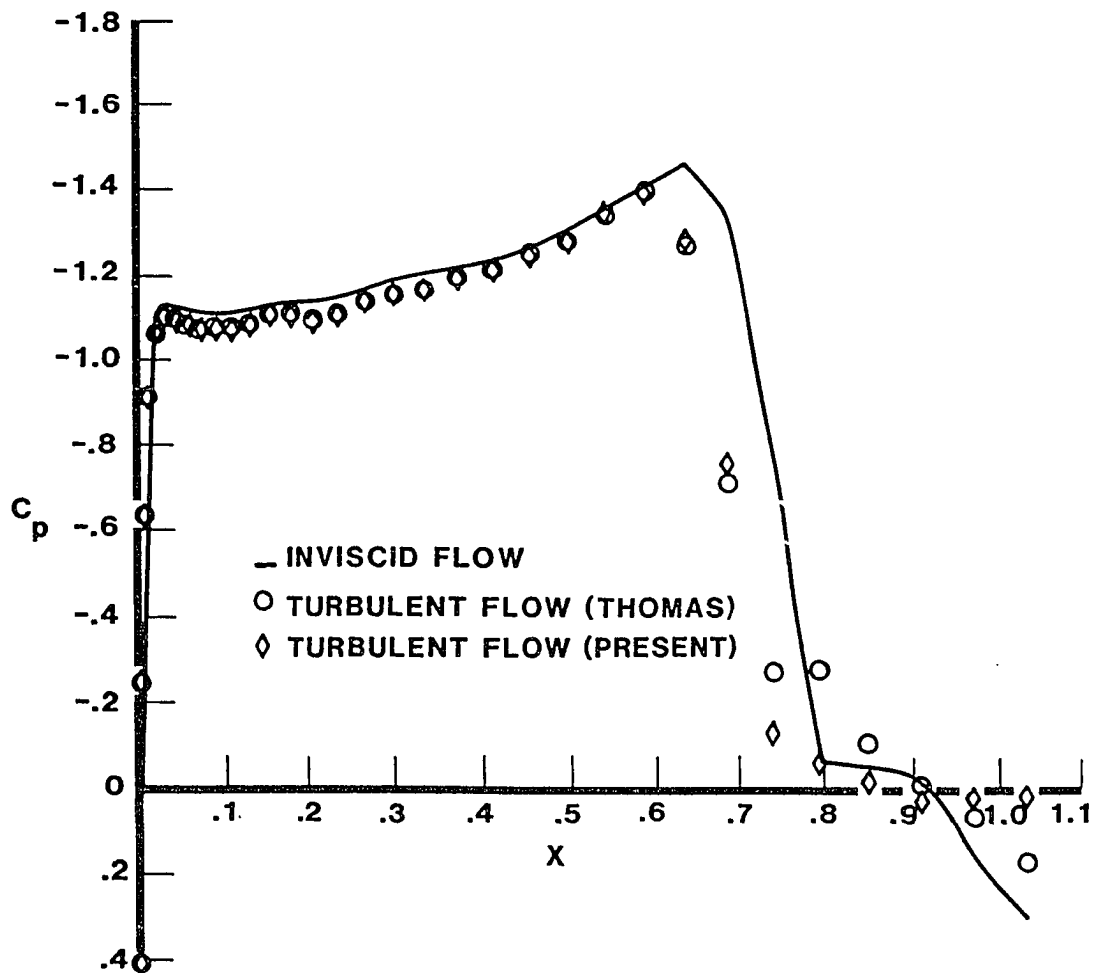
Fig. 4.21   Pressure distribution on the upper surface of RAE-2822

supercritical airfoil at $M_\infty = 0.73$, $\alpha = 2.78^\circ$, and

$Re = 6.5 \times 10^6$.

Thomas [74] was used. The pressure coefficient values are compared in Fig. 4.21. In the forward portion of the airfoil the pressure coefficient values are slightly lower with the present model. In this area results using the equilibrium dissipation model of Thomas [74] are closer to the experimental data. The agreement between the results of the two methods is very good except close to the shock foot. The C_p values are underpredicted near the shock and in the rearward portion of the airfoil. The lift coefficient values are found to be 0.97,0.90 and 0.91 for the inviscid, equilibrium dissipation, and present methods, respectively.

Results are presented for a supercritical case with separation at about 60% of the chord in Fig. 4.22. This case corresponds to case 10 of Ref. [94]. The free stream Mach number is 0.75 and the Reynolds number of the flow is 6.2 million. The corrected angle of attack is 2.81°. The viscous-inviscid interaction calculations were started at about 18% of the chord on the upper surface and at 15.5% on the lower surface. The boundary layer has been tripped to become turbulent at these points in the experiment. The present results are compared with the experimental data of Cook et al. [94]. The pressure distribution in Fig. 4.22 indicates that the agreement with the experiment is good in the acceleration zone where the boundary layer is thin. In the experiment the flow separation was observed near the foot of the shock between 62-72% of the chord length. In the present method suction was applied near the shock foot to keep turbulent attached flow conditions on the airfoil. The displacement thickness values are compared in Fig. 4.23. Because of suction, the displacement thickness does not increase as rapidly as the experimental values in the pressure rise area. In the
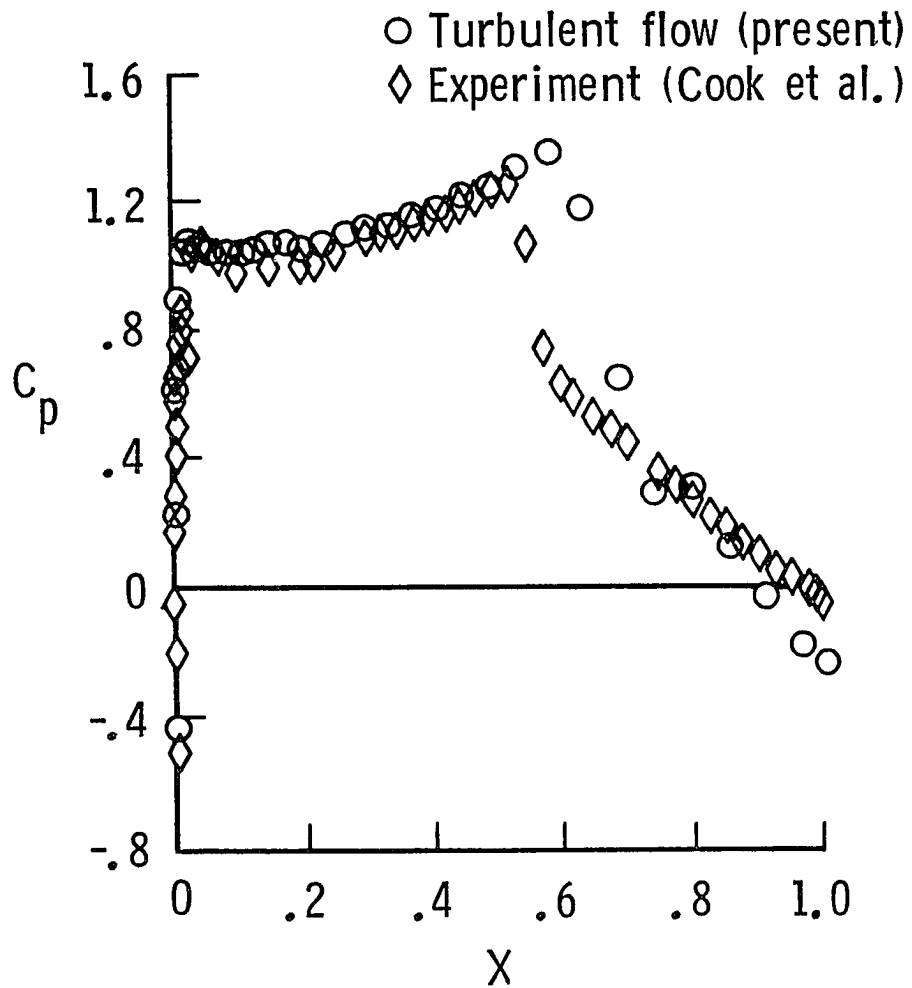
Fig. 4.22 Pressure thickness distribution on the upper surface of

RAE-2822 supercritical airfoil at $M_\infty = 0.75$, $\alpha = 2.81°$,
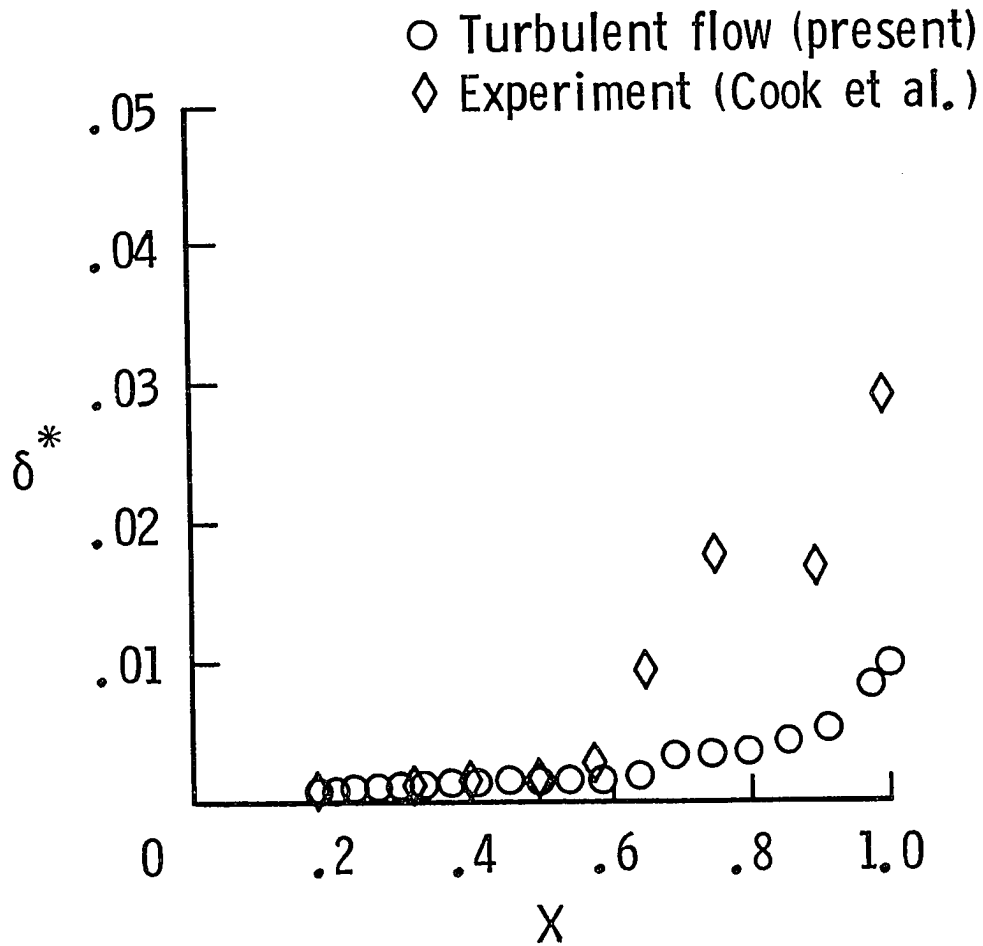
and Re = 6.2×10^6.

Fig. 4.23 Displacement thickness distribution on the upper surface of RAE-2822 supercritical airfoil at $M_\infty = 0.75$, $\alpha = 2.81°$, and $Re = 6.2 \times 10^6$.

experiment the wake is much thicker due to turbulent separation compared to the turbulent attached flow results by the present method. Because of this reason the C_p values are higher near the trailing edge.

The upper surface pressure distribution is presented in Fig. 4.24 for the NACA-0012 airfoil at subcritical conditions. The free stream Mach number is 0.601 and the corrected angle of attack based on the linear theory is 3.19° [95]. The Reynolds number of the flow is three million. The results are compared with the experimental data of Harris [95]. In the experiments the flow was tripped at about 5% of the chord length. The boundary-layer interaction was started corresponding to the experimental data. The numerical results obtained in this study and by Thomas [74] agree closely with the experimental data. However, better agreement is noted between the experiment and the present method in the forward portion of the airfoil. In the rearward portion, the pressure distribution is very close to the inviscid case.

The pressure coefficient results are presented in Fig. 4.25 for a free stream Mach number of 0.758 and for an angle of attack of 3.06°. Suction was applied at about 30% of the chord to keep the flow from being separated. In the experiment there was no attempt to apply any suction. The flow might have separated at about 35% of the chord and reattached after the shock. For the above conditions, the computer program using the equilibrium dissipation model failed to produce any results because of the extensive separation of the flow. Also the present method does not work if the suction is not applied before the separation occurs. The agreement between experiment and the present method is good up to about 30% of the chord. The turbulent boundary layer thickens rapidly after that point. The flow is separated and the
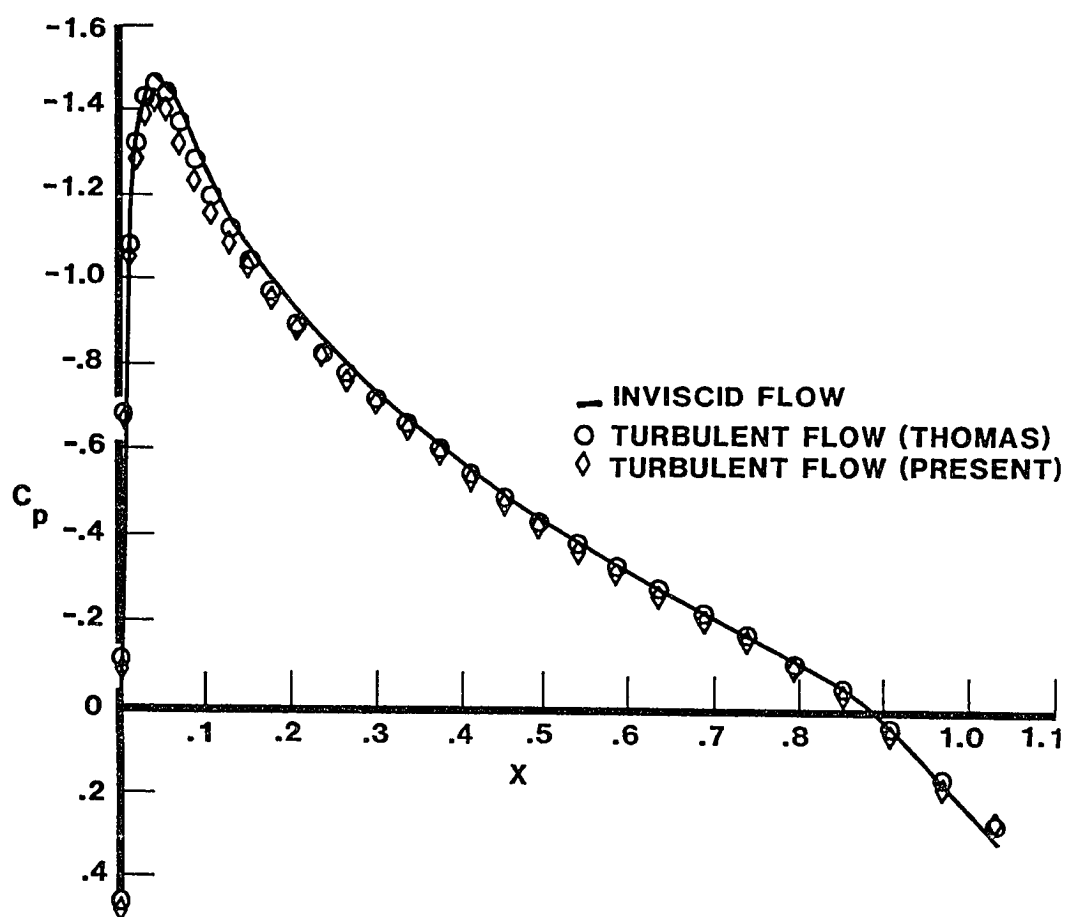
Fig. 4.24 Pressure distribution on the upper surface of NACA-0012

airfoil at $M_\infty = 0.601$, $\alpha = 3.19^\circ$, and $Re = 3.0 \times 10^6$.
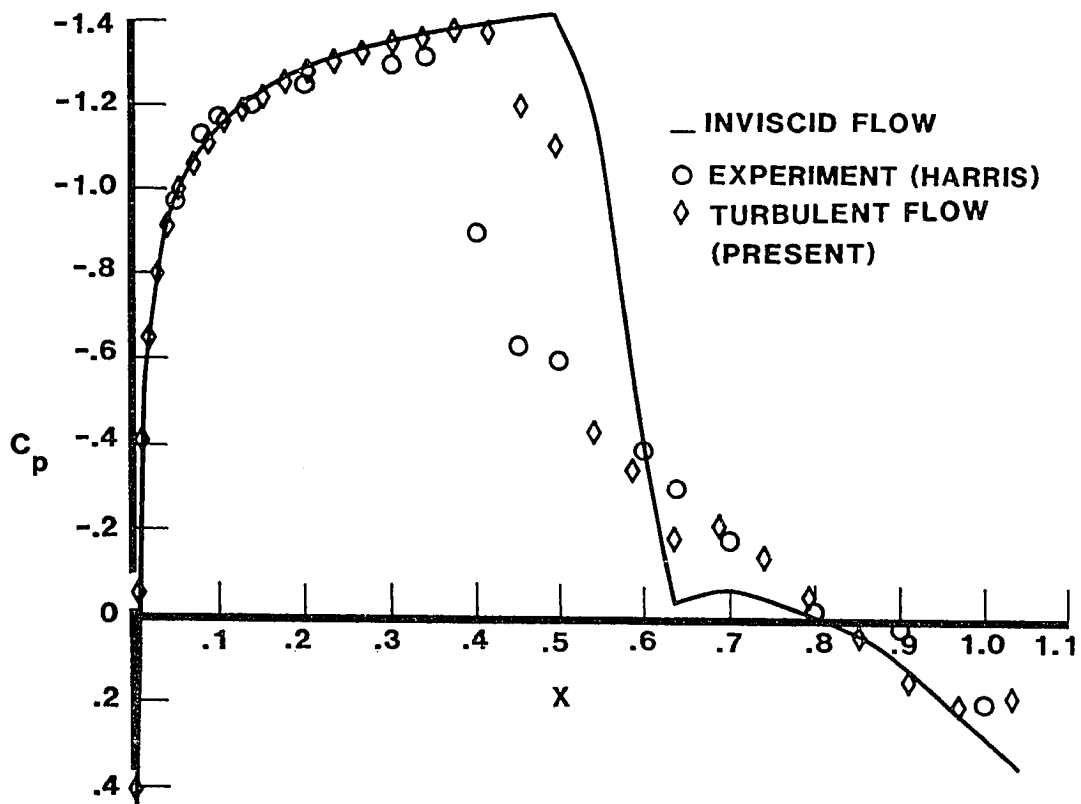
Fig. 4.25 Pressure distribution on the upper surface of NACA-0012 airfoil at $M_\infty = 0.758$, $\alpha = 3.06°$, and Re = 3.0×10^6.

shock front is moved towards the leading edge and also, as observed in the case of laminar flow, the strength of the shock is reduced. By applying the suction before the separation point, the flow separation was delayed by about 20% of the chord. The pressure rise is much more gradual that it would be in the case without the suction. After the shock the computational results are close to the experimental data.

Chapter 5

CONCLUSIONS

The viscous/inviscid interaction over transonic airfoils with and without suction is studied. Two approaches are considered to achieve the coupling between the viscous and inviscid flows. The first approach is a direct approach and is referred to as the hybrid method. In the second approach the entire inviscid flow field is investigated by solving the Euler equations using finite volume technique. The viscous flow is coupled to the inviscid flow using surface transpiration condition.

The interaction process in the hybrid method is continuous, and since all the dependent variables are calculated simultaneously, the convergence is faster and the solutions are more accurate. Using this method, flow over a 6% thick circular arc airfoil at $M_\infty = 0.868$ and $\alpha = 0^\circ$ is studied. In the forward portion of the airfoil it was sufficient to apply weak interaction formulation and the strong interaction equations are applied near and downstream of the shock. The separation was predicted at 70% of the chord and is in complete agreement with the experimental data of Collins and Krupp [81]. The pressure distribution calculations using laminar separated velocity profiles show a good agreement with the experimental values [81].

To avoid the Goldstein singularity near the separation point, the boundary-layer equations and the initial conditions are derived in an inverse form to obtain regular solutions for the flows with small separations. It is important to apply minimum amount of suction that is required to have attached flow on the airfoil. A method is developed to achieve this by varying the suction parameter based on the velocity profile parameter value. The suction distribution thus obtained is considered to be close to the optimum value. At subcritical conditions the present solutions are compared with the experimental data [89-91] and the agreement is excellent for NACA 66-012, DESB 154 and KING COBRA airfoils. These comparisons for subcritical airfoils establish confidence in the suction velocity profiles that are obtained using the small perturbation theory and the state variable approach of Forbrich [60].

Results are obtained for RAE-2822 and NACA-0012 airfoils at super-critical conditions. These results indicate that a small amount of suction is required to avoid flow separation near the pressure peak at the leading edge. Most of the suction requirement is to maintain attached flow conditions in the rear part of the airfoil or near the shock. Application of larger amount of suction than required was found to have destabilizing effect on the boundary layer. Laminar flow separation reduced the shock strength considerably and shock is moved forward in comparison to the laminar attached flow with suction.

The results from the present study are in good agreement with the theoretical as well as the experimental data for attached flow condi-tions with turbulent boundary layer. At supercritical conditions the boundary layer tends to separate and application of suction has been

considered to maintain attached flow. Although the eddy viscosity model used is valid for both attached and separated flow conditions, the flow separation calculations could not be performed satisfactorily, perhaps due to the presence of suction. If the experimental data is available for turbulent separated flow with suction, the present method could be extended to separated flow conditions. For laminar as well as turbulent boundary layers the displacement thickness is small compared to the corresponding separated flow conditions and the wake thickness is much smaller. The strong interaction near the trailing edge has to be considered if the flow separates near the shock.

The boundary-layer integral method coupled with the method of integral relations gives a computationally inexpensive solution for transonic laminar viscous-inviscid interaction over airfoils. However, this method requires man-machine interaction and the solution can not be obtained in one computer run. The inverse boundary-layer approach obtains the flow solution as well as the suction distribution to keep the attached flow on the airfoil in one run. However, the boundary layer equations are not of strong interaction type. Since the shock influence point has to be determined in an iterative process the computational requirement is very high. The vectorized version of the Euler solver for the inviscid flow could be used in a further study to include the shock influence point iteration so that the strong interaction model is incorporated.

REFERENCES

1. Murman, E. M. and J. D. Cole, "Calculation of Plane Steady Transonic Flows," AIAA Journal, Vol. 9, No. 1, January 1971, pp. 114-121.

2. Kutler, P, "A Perspective of Theoretical and Applied Computational Fluid Dynamics," AIAA Paper 83-0037, January 1983.

3. Magnus, R. and H. Yoshihara, "Inviscid Transonic Flow over Airfoils," AIAA Journal, Vol. 8, December 1970, pp. 2157-2162.

4. Krupp, J. A. and E. M. Murman, "Computation of Transonic Flows Past Lifting Airfoils and Slender Bodies," AIAA Journal, Vol. 10, July 1972, pp. 880-886.

5. Lomax, H., F. R. Bailey, and W. F. Ballhaus, "On the Numerical Simulation of Three Dimensional Transonic Flow with Application to the C-141 Wing," NASA TN D-6933, August 1973.

6. Klunker, E. B., and P. A. Neuman, "Computation of Transonic Flow about Lifting Wing-Cylinder Combinations," Journal of Aircraft, Vol. 11, April 1974, pp. 254-256.

7. Schmidt, W., S. Rohlfs, and R. Vanino, "Some Results Using Relaxation Methods for Two and Three-dimensional Transonic Flows," Proceedings of the Fourth International Conference on Numerical Methods in Fluid Dynamics, Boulder, June 1974, pp. 364-372, Springer, New York, 1975.

8. Albone, C. M., M. G. Hall, and G. Joyce, "Numerical Solution of Flows past Wing-Body Combinations, Symposium Transsonicum II," Gottingen, September 1975.

9. Van der Vooren, J., J. W. Slooff, G. H. Huizing, and A. van Essen, "Remarks on the Suitability of Various Transonic Perturbation Equations to Describe Three-dimensinal Transonic Flow: Examples of Computations Using a Fully Conservative Rotated Difference Scheme," Symposium Transsonicum II, Göttingen, September 1975, pp. 557-566.

10. Garabedian, P. R. and D. G. Korn, "Analysis of Transonic Airfoils," Comm. Pure Appl. Math., Vol. 24, November 1971, pp. 841-851.

11. Jameson, Antony, "Numerical Computation of Transonic Flows with Shock Waves," Symposium Transsonicum II, Göttingen, September 1975, pp. 384-414.

12. Arlinger, B. G., "Calculation of Transonic Flow around Axisymmetric Inlets," AIAA Paper 75-80, January 1975.

13. Baker, T. J., "A Numerical Method to Compute Inviscid Transonic Flows around Axisymmetric Ducted Bodies," Symposium Transsonicum II, Göttingen, September 1975, pp. 495-506.

14. Caughey, D. A. and A. Jameson, "Accelerated Iterative Calculation of Transonic Nacelle Flow Fields," AIAA Paper 76-100, January 1976.

15. Jameson, Antony, "Iterative Solution of Transonic Flows over Airfoils and Wings Including Flows at Mach 1," Comm. Pure Appl. Math., Vol. 27, May 1974, pp. 283-309.

16. Carlson, L. A., "Transonic Airfoil Flowfield Analysis Using Cartesian Coordinates," NASA CR-2577, August 1975; also in Journal of Aircraft, Vol. 13, No. 5, May 1976, pp. 349-356.

17. Hafez, M. M. and D. Lovell, "Numerical Solution of the Transonic Streamfunction Equation," AIAA Journal, Vol. 21, No. 3, March 1983, pp. 327-335.

18. Ballhaus, W. F., A. Jameson, and J. Albert, "Implicit Approximate-Factorization Schemes for Steady Transonic Flow Problems," AIAA Journal, Vol. 16, No. 6, June 1978, pp. 573-579.

19. South, J. C. and A. Brandt, "The Multi-Grid Method: Fast Relaxation for Transonic Flows," Advances in Engineering Science, CP-2001, Vol. 4, NASA, November 1976, pp. 1359-1369.

20. Jameson, A., "Accelerated Iterative Schemes for Transonic Flow Calculations Using Fast Poisson Solvers," ERDA Report COO-3077, March 1975, New York University.

21. Steinhoff, J. S. and A. Jameson, "Non-uniqueness in Transonic Potential Flows," Proceedings of the GAMM Specialist Workshop for Numerical Methods in Fluid Mechanics, Stockholm, September 1979.

22. Steinhoff, J. S. and A. Jameson, "Multiple Solutions of the Transonic Potential Flow Equations," AIAA Paper 81-1019, Proceedings AIAA 5th Computational Fluid Dynamics Conference, Palo Alto, CA, 1981, pp. 347-353.

23. Salas, M. D., A. Jameson, and R. E. Melnik, "A Comparative Study of the Nonuniqueness Problem of the Potential Equation," AIAA Paper 83-1888-CP, AIAA 6th Computational Fluid Dynamics Conference, Danvers, MA, July 13-15, 1983.

24. Doria, M. L. and J. C. South, Jr., "Transonic Potential Flow and Coordinate Generation for Bodies in a Wind Tunnel," AIAA Paper No. 82-0223, AIAA 20th Aerospace Sciences Meeting, Orlando, FL, January 1982.

25. Holt, M. and Masson, B. S., "The Calculation of High Subsonic Flow Past Bodies by the Method of Integral Relations," Proceedings Second International Conference on Numerical Methods in Fluid Dynamics, Vol. 8, Springer-Verlag, New York, 1971, pp. 207-214.

26. Airfoils by a Multistrip Method of Integral Relations," Proceedings of the Second International Conference on Numerical Methods in Fluid Dynamics, Vol. 8, Springer-Verlag, New York, 1971, pp. 243-251.

27. Sato, J., "Application of Dorodnitsyn's Technique to Compressible Two-Dimensional Airfoil Theories at Transonic Speeds," National Aerospace Laboratory, Tokyo, Japan, Report TR-220T, October 1970.

28. Tai, T. C., "Transonic Inviscid Flow over Lifting Airfoils by the Method of Integral Relations," AIAA Journal, Vol. 12, No. 6, June 1974, pp. 798-804; also, Naval Ship Research and Development Center (NSRDC) Report No. 3424, July 1971.

29. Liepmann, H. W., "Interaction between Boundary Layers and Shock Waves in Transonic Flow," Journal of the Aeronautical Sciences, Vol. 13, No. 12, December 1946, pp. 223-237.

30. Ackeret, J., F. Feldman, and N. Rott, "Investigation of Compression Shocks and Boundary Layers in Gases Moving at High Speeds," NACA TM 1113, January 1947.

31. Bauer, F., P. R. Garabedian, and D. G. Korn, "Supercritical Wing Sections," Lecture Notes in Economics and Mathematical Systems, No. 66, Springer-Verlag, Berlin, 1972.

32. Bauer, F., P. R. Garabedian, and A. Jameson, "Supercritical Wing Sections II," Lecture Notes in Economics and Mathematical Systems, No. 108, Springer-Verlag, Berlin, 1975.

33. Nash, J. E. and A. G. J. Macdonald, "The Calculation of Momentum Thickness in a Turbulent Boundary Layer at Mach Numbers up to Unity," NPL Aero. Report 1207, Aeronautical Research Council (ARC) Current Paper 963, 1966.

34. Collyer, M. R., "An Extension to the Method of Garabedian and Korn for the Calculation of Transonic Flow Past an Airfoil to Include the Effects of a Boundary Layer and Wake," RAE Technical Report 77104, July 1977.

35. Collyer, M. R. and R. C. Lock, "Improvements to the Viscous Garabedian and Korn (VGK) Method for Calculating Transonic Flow Past an Airfoil," RAE Technical Report 78039, August 1978.

36. Collyer, M. R. and R. C. Lock, "Prediction of Viscous Effects in Steady Transonic Flow Past an Airfoil," _Aeronautical Quarterly_, August 1979, pp. 485-505.

37. Green, J. E., D. J. Weeks, and J. W. F. Broman, "Prediction of Turbulent Boundary Layers and Wakes in Compressible Flow by a Lag-entrainment Method," Aeronautical Research Council, ARC R & M No. 3791, 1977.

38. Melnik, R. E., "Turbulent Interactions on Airfoils at Transonic Speeds - Recent Developments," Advisory Group for Aerospace Research and Development (AGARD) CP-291, February 1981.

39. Klineberg, J. M. and J. L. Steger, "Calculation of Separated Flows at Subsonic and Transonic Speeds," Third International Conference on Numerical Methods in Fluid Dynamics, Paris, France, July 1972.

40. Brilliant, H. M. and T. C. Adamson, Jr., "Shock Wave-Boundary Layer Interactions in Laminar Transonic Flow," Paper 73-239, AIAA 11th Aerospace Sciences Meeting, Washington, DC, January 1973.

41. Tai, C. T., "Transonic Laminar Viscous/Inviscid Interaction over Airfoils," Naval Ship Research and Development Center (NSRDC) Report No. 4362, June 1974.

42. Lees, L. and B. L. Reeves, "Supersonic Separated and Reattached Laminar Flows: I. General Theory and Application of Adiabatic Boundary Layer Shock Wave Interactions," _AIAA Journal_, Vol. 2, No. 11, November 1964, pp. 1907-1920.

43. Klineberg, J. M. and L. Lees, "Theory of Laminar Viscous-Inviscid Interactions in Supersonic Flow," _AIAA Journal_, Vol. 17, No. 12, December 1969.

44. Goldstein, S., "On Laminar Boundary Layer Flow Near a Position of Separation," _Quarterly Journal of Mechanics and Applied Mathematics_, Vol. 1, March 1948, pp. 43-69.

45. Klineberg, J. and J. Steger, "On Laminar Boundary-Layer Separation," AIAA Paper 74-94, January 1974.

46. Werle, M. J. and R. T. Davis, "Incompressible Laminar Boundary Layers on a Parabola at Angle of Attack: A Study of the Separation Point," _Journal of Applied Mathematics_, Vol. 7, 1972.

47. Pletcher, R. and C. Dancey, "A Direct Method of Calculating Through Separated Regions in Boundary Layer Flow," _Journal of Fluids Engineering_, September 1976, pp. 568-572.

48. Murphy, J. and L. King, "Airfoil Flow-Field Calculations with Coupled Boundary-Layer Potential Codes," Second Symposium on Numerical and Physical Aspects of Aerodynamic Flows, California State University, Long Beach, CA, 1983.

49. Catherall, D. and K. W. Mangler, "The Integration of the Two-Dimensional Laminar Boundary-Layer Equations Past a Point of Vanishing Skin Friction," *Journal of Fluid Mechanics*, Vol. 26, September 1966, pp. 163-182.

50. Carter, J., "Inverse Solutions for Laminar Boundary Layer Flows with Separation and Attachment," NASA TR R-447, November 1975.

51. Cebeci, T., H. Keller, and P. Williams, "Separating Boundary-Layer Flow Calculations," *Journal of Computational Physics*, Vol. 31, June 1979, pp. 363-378.

52. Horton, H., "Separating Laminar Boundary Layers with Prescribed Wall Shear," *AIAA Journal.*, Vol. 12, December 1974.

53. Liepmann, H. W. and Roshko, A., *Elements of Gas Dynamics*, John Wiley Inc., New York, 1960.

54. Jameson, A., "Transonic Potential Flow Calculations Using Conservative Form," *Proceedings of AIAA 2nd Computational Fluid Dynamics Conference*, Hartford, Conn., 1975, pp. 148-161.

55. Illingworth, C. R., "Steady Flow in the Laminar Boundary Layer of a Gas," *Proceedings Royal Society London Ser. A.*, Vol. 99, No. A1059, December 7, 1949, pp. 533-558.

56. Stewartson, K., "Further Solutions of the Falkner-Skan Equation," *Proceedings of the Cambridge Philosophical Society.*, Vol. 50, 1954, pp. 454-465.

57. Crocco, L. and Lees, L., "A Mixing Theory for the Interaction Between Dissipative Flows and Nearly Isentropic Streams," *Journal of the Aerospace Sciences*, Vol. 19, 1952, pp. 649-676.

58. Falkner, V. M. and Skan, S. N., "Some Approximate Solutions of the Boundary Layer Equations," Aeronautical Research Council, R&M 1314, April 1930.

59. Stewartson, K., "Correlated Incompressible and Compressible Boundary Layers," *Proceedings Royal Society London Ser. A*, Vol. 200, 1949, pp. 85-100.

60. Forbrich, Jr., C. A., "Improved Solutions to the Falkner-Skan Boundary Layer Equations," *AIAA Journal*, Vol. 20, No. 9, September 1982, pp. 1306-1307.

61. Klineberg, J. M. and Steger, J. L., "Calculations of Separated Flows at Subsonic and Transonic Speeds," *Proceedings of the 3rd International Conference on Numerical Methods in Fluid Mechanics*, July 1972, Vol. II, Springer-Verlag, Berlin, 1973, pp. 161-168.

62. Ram, R. B., Vemuru, C. S., and Harvey, W. D., "Hybrid Approach to Steady Transonic Normal Shock-Compressible Laminar Boundary Layer

Interactions Over Airfoils With Suction," Paper 85-0522, AIAA Shear Flow Control Conference, Boulder, Colorado, March 1985.

63. Tai, T. C, "Transonic Turbulent Viscous-Inviscid Interaction Over Airfoils," Paper 75-78, AIAA 13th Aerospace Sciences Meeting, Pasadena, California, January 1975.

64. Kuhn, G. D. and Nielson, J. N., "Prediction of Turbulent Separated Boundary Layers," AIAA Paper No. 73-663, Palm Springs, California, July 1973.

65. Schlichting, H., Boundary Layer Theory, 6th ed., McGraw Hill, New York, 1968.

66. Loving, D. L., "Wind Tunnel Correlation of Shock Induced Separated Flow, NASA TN-D-3580, September 1966.

67. LeBalleur, J. C., "Viscous-Inviscid Coupling Calculations for Two- and Three-Dimensional Flows," Von Karman Institute for Fluid Dynamics, Lecture Series 1982-04, March 1982.

68. Bavitz, P. C., "An Analysis Method for Two-Dimensional Transonic Viscous Flow," NASA TN-D-7718, January 1975.

69. Nandanan, M., Stanewsky, E., and Inger, G. R., "Airfoil Flow Analysis With a Special Solution for Shock/Boundary Layer Interaction," AIAA Journal, Vol. 19, No. 12, December 1981, pp. 1540-1546.

70. Inger, G. R., "Some Features of a Shock-Turbulent Boundary Layer Interaction Theory in Transonic Flowfields," Advisory Group for Aerospace Research and Development (AGARD) CP-291, February 1981.

71. Wai, J. and Yoshihara, H., "Viscous Transonic Flow Over Airfoils," Boling Report D180-25934, Proceedings of 7th International Conference on Numerical Methods in Fluid Dynamics, Stanford and NASA Ames, June 1980.

72. Jameson, A., Schmidt, W., and Turkel, E., "Numerical Solutions of the Euler Equations by Finite Volume Methods Using Runge-Kutta Time-Stepping Schemes," AIAA Paper No. 81-125, June 1981.

73. Whitfield, D. L., Thomas, J. L., Jameson, A., and Schmidt, W., "Computation of Transonic Viscous-Inviscid Interaction Flow," Second Symposium on Numerical and Physical Aspects of Aerodynamic Flows, Cebeci, T. (ed.), Springer-Verlag, New York, 1983.

74. Thomas, J. L., "Transonic Viscous-Inviscid Interaction Using Euler and Inverse Boundary Layer Equations," Ph.D. Thesis, College of Engineering, Mississippi State University, Mississippi, December 1983.

75. Johnston, W. and Sockol, P., "Matching Procedure for Viscous-Inviscid Interactive Computations," AIAA Journal, Vol. 17, No. 6, June 1979, pp. 661-663.

76. Murman, E. M. and Bussing, T. R. A., "On the Coupling of Boundary Layer and Euler Equation Solutions," Second Symposium on Numerical and Physical Aspects of Aerodynamic Flows, Cebeci, T. (ed.), Springer-Verlag, New York, 1983.

77. Rizzi, A., "Numerical Implementation of Solid-Body Boundary Conditions for the Euler Equations," Zeitschrift fuer Angewandte Mathematik und Mechanik (ZAMM), Vol. 58, July 1978, pp. 301-304.

78. Carter, J. E., "Inverse Solutions for Laminar Boundary-Layer Flows With Separation and Reattachments," NASA TR R-447, November 1975.

79. Tai, T. C., "Transonic Laminar Viscous-Inviscid Interaction Over Airfoils," AIAA Journal, Vol. 13, No. 8, August 1975, pp. 1065-1072.

80. Schubauer, B. G., "Air Flow in a Separating Laminar Boundary Layer," NACA Report 527, 1935.

81. Collins, D. J. and Krupp, J. A., "Experimental and Theoretical Investigations in Two-Dimensional Transonic Flow," AIAA Journal, Vol. 12, June 1974, pp. 771-778.

82. Murman, E. M., "Computation of Wall Effects in Ventilated Transonic Wind Tunnels," AIAA Paper No. 72-1007, Palo Alto, California, September 1972.

83. Carlson, L. A., TRANSEP, "A Program for High Lift Separated Flow About Airfoils," NASA CR-3376, December 1982.

84. Harvey, W. D. and Pride, J. D., "The NASA Langley Laminar Flow Control Airfoil Experiment," Paper 82-0567, Proceedings 12th AIAA Aerodynamic Testing Conference, Williamsburg, Virginia, March 1982.

85. Carlson, L. A., TRANDES, "A FORTRAN Program for Transonic Airfoil Analysis or Design," NASA CR-2821, June 1977.

86. Ackeret, J., Feldmann, F., and Rott, N., "Investigations of Compression Shocks and Boundary Layers in Gases Moving at High Speeds," NACA TM 1113, January 1947.

87. Holder, D. W., "The Transonic Flow Past Two-Dimensional Airfoils," Journal of Royal Aeronautical Society, Vol. 68, August 1964, pp. 501-516.

88. Holder, D. W., Pearcey, H. H., and Gadd, G. W., "The Interaction Between Shock Waves and Boundary Layers," Aeronautical Research Council, CP 180, London, England, February 1954.

89. Gault, D. E., "An Experimental Investigation of Boundary-Layer Control for Drag Reduction of a Swept-Wing Section at Low Speed and High Reynolds Numbers," NASA TN D-320, October 1960.

90. Viken, J. K., "Aerodynamic Design Considerations and Theoretical Results for a High Reynolds Number Natural Laminar Flow Airfoil," Master's Thesis submitted to George Washington University, January 1983.

91. Gray, W. E. and Fullam, P. W. J., "Comparison of Flight and Tunnel Measurements of Transition on a Highly Finished Wing (King Cobra)," Royal Aircraft Establishment, Report No. AERO 2383, June 1950.

92. Ram, R. B. and Harvey, W. D., "Hybrid Approach to Steady Transonic Normal Shock-Compressible Laminar Boundary Layer Interactions Over Airfoils," Paper 84-1561, AIAA 17th Fluid Dynamics, Plasma Dynamics, and Lasers Conference, Snowmass, Colorado, June 25-27, 1984.

93. Harvey, W. D., Harris, C. D., Brooks, C. W., and Bobbitt, P. J., "Experimental Results on a Swept Supercritical Airfoil With Suction in the Langley 8-Foot Transonic Pressure Tunnel," AIAA Shear Flow Control Conference, Boulder, Colorado, March 12-14, 1985.

94. Cook, P. H., McDonald, M. A., and Firmin, M. C. P., "Aerofoil RAE-2822 Pressure Distributions and Boundary-Layer and Wake Measurements," Advisory Group for Aerospace Research and Development (AGARD), AR-138, Paper A6, May 1979.

95. Harris, C. D., "Two-Dimensional Aerodynamic Characteristics of the NACA-0012 Airfoil in the Langley 8-Foot Transonic Pressure Tunnel," NASA TM-81927, April 1981.

APPENDICES

Appendix A

LAMINAR BOUNDARY-LAYER EQUATIONS WITH SUCTION

The laminar boundary-layer equations (2.15) can be expressed as

$$\frac{d\delta_i^*}{ds} = \frac{1}{D_1} \begin{vmatrix} d_1 & a_{12} & a_{13} \\ d_2 & a_{22} & a_{23} \\ d_3 & a_{32} & a_{33} \end{vmatrix} \tag{A.1}$$

$$\frac{da}{ds} = \frac{1}{D_1 \cdot \dfrac{dH}{da}} \begin{vmatrix} a_{11} & d_1 & a_{13} \\ a_{21} & d_2 & a_{23} \\ a_{31} & d_3 & a_{33} \end{vmatrix} \tag{A.2}$$

$$\frac{dM_e}{ds} = \frac{1}{D_1} \begin{vmatrix} a_{11} & a_{12} & d_1 \\ a_{21} & a_{22} & d_2 \\ a_{31} & a_{32} & d_3 \end{vmatrix} \tag{A.3}$$

where

$$a_{11} = F \tag{A.4}$$

$$a_{21} = H \tag{A.5}$$

$$a_{31} = J \tag{A.6}$$

$$a_{12} = \delta_i^* \tag{A.7}$$

$$a_{22} = \delta_i^* \tag{A.8}$$

$$a_{32} = \delta_i^* \frac{dJ}{dH} \tag{A.9}$$

$$a_{13} = \frac{\delta_i^* f_A}{M_e} \tag{A.10}$$

$$a_{23} = \frac{\delta_i^*(2H + 1)}{M_e} \tag{A.11}$$

$$a_{33} = \frac{3\delta_i^* J}{M_e} \tag{A.12}$$

$$d_1 = \frac{\beta}{m_e} \frac{1+m_e}{1+m_\infty} \tan\Theta - \frac{V_\omega}{U_e} \tag{A.13}$$

$$d_2 = \beta \frac{M_\infty}{M_e} \frac{Q}{Re_{\delta_i^*}} + \frac{V_\omega}{U_e} \tag{A.14}$$

$$d_3 = \beta \frac{M_\infty}{M_e} \frac{R}{Re_{\delta_i^*}} + \frac{V_\omega}{U_e} \tag{A.15}$$

$$D_1 = a_{11}\left(a_{22}a_{33} - a_{23}a_{32}\right) - a_{12}\left(a_{21}a_{33} - a_{23}a_{31}\right)$$

$$+ \ a_{13}\left(a_{21}a_{32} - a_{22}a_{31}\right) \tag{A.16}$$

Appendix B

TURBULENT BOUNDARY-LAYER EQUATIONS WITH SUCTION

The turbulent boundary-layer equations are given by Equation (2.52)
as

$$
\begin{bmatrix} A_{11} & A_{12} & A_{13} \\ A_{21} & A_{22} & A_{23} \\ A_{31} & A_{32} & A_{33} \end{bmatrix} \begin{bmatrix} (U_\tau)_\zeta \\ (\delta^*)_\zeta \\ (U_e)_\zeta \end{bmatrix} = \begin{bmatrix} B_1 \\ B_2 \\ B_3 \end{bmatrix} \tag{B.1}
$$

where

$$
A_{11} = \int_0^\delta \text{FIRST } d\eta
$$

$$
A_{12} = \int_0^\delta \text{SECOND } d\eta
$$

$$
A_{13} = \int_0^\delta \text{THIRD } d\eta
$$

$$
A_{21} = \int_0^\delta (\text{FIRST}) \text{ FACT } d\eta
$$

$$
A_{22} = \int_0^\delta (\text{SECOND}) \text{ FACT } d\eta
$$

$$A_{23} = \int_0^\delta (\text{THIRD})\ \text{FACT}\ d\eta - 0.5\ U_e$$

$$A_{31} = \int_0^\delta (\text{FOURTH})\ d\eta$$

$$A_{32} = \int_0^\delta (\text{FIFTH})\ d\eta$$

$$A_{33} = \int_0^\delta (\text{SIXTH})\ d\eta$$

$$\text{FACT} = 2\eta U - U_e - \int_0^\eta \frac{U}{U_e}\ d\eta + \int_0^\delta \frac{U}{U_e}\ d\eta$$

$$B_1 = - \frac{\beta_1(0)}{Re_\infty\ \delta U_e} \left(\frac{\partial U}{\partial \eta}\right)_w$$

$$B_2 = - \frac{1}{Re_\infty\ \delta U_e} \int_0^\delta \beta_1 \frac{\partial U}{\partial \eta}\ d\eta$$

$$B_3 = V_w - V_e$$

$$C_1 = B_1 - A_{12} \frac{d\delta}{d\zeta}$$

$$C_2 = B_3 - A_{32} \frac{d\delta}{d\zeta}$$

$$\text{FIRST} = \Bigg\{ U_\tau[-0.5(1-C2)]\ [2.5 \log (C6) + 5.1)^2\ V_w$$

$$+ 2.5 \log(C6) - (3.39\ \text{DELP} + 5.1)e^{-C5} + 5.1\Big]$$

$$+ \Big[(2.5 \log (C7) + 5.1)^2\ V_w + 2.5 \log (C7)$$

$$- (3.39\ \text{ETAP} + 5.1)e^{-C8} + 5.1\Big]$$

$$+ 0.5(1 - C2)U_e \Bigg\} \Bigg\{ + 0.5(C2 - 1)U_\tau \Bigg[\frac{5.0(2.5 \log (C6) + 5.1)}{C6} \ C9 \ V_w \delta$$

$$+ 0.37(3.39 \ \text{DELP} + 5.1)e^{-C5} \ C9 \ \delta - 3.39 \ e^{-C5} \ C9 \ \delta$$

$$+ \frac{2.5 \ C9 \ \delta}{C5} \Bigg] + U_\tau \Bigg[\frac{5.0 \ \eta \ C9 \ V_w}{C7} \ (2.5 \ \log \ (C7) + 5.1)$$

$$+ 0.37(3.39 \ \text{ETAP} + 5.1)\eta \ C9 \ e^{-C5} - 3.39 \ \eta \ e^{-C5} \ C9$$

$$+ \frac{2.5 \ \eta \ C9}{C7} \Bigg] - 0.5(1 - C2)\Big[(2.5 \ \log \ C6 + 5.1)^2 \ V_w$$

$$+ 2.5 \ \log \ C6 - (3.39 \ \text{DELP} + 5.1)e^{-C5} + 5.1)$$

$$+ (2.5 \ \log \ C7 + 5.1)^2 \ V_w + 2.5 \ \log \ (C7)$$

$$- (3.39 \ \text{ETAP} + 5.1)e^{-C5} + 5.1 \Big] \Bigg\}$$

$$- \Bigg\{ U_\tau \Bigg[-0.5 \ C1 \ \pi \big[(2.5 \ \log \ C6 + 5.1)^2 \ V_w$$

$$+ 2.5 \ \log \ C6 - (3.39 \ \text{DELP} + 5.1)e^{-C5} + 5.1 \big] / \delta$$

$$+ \frac{5.0(2.5 \ \log \ C7 + 5.1) \ |U_\tau| \ V_w}{C7 \ \nu}$$

$$+ \frac{0.37\Big(3.39 + 5.1 - \frac{3.39}{0.37}\Big) \ e^{-C5} \ |U_\tau|}{\nu}$$

$$+ \frac{2.5 \ |U_\tau|}{C7 \ \nu} + \frac{0.5 \ C1 \ \pi \ U_e}{\delta} \Bigg]$$

$$+ \Bigg[0.5 \ U_\tau (C1 \ \delta - \eta\pi) \Bigg[\frac{5.0(2.5 \ \log \ C6 + 5.1) \ C9 \ V_w \ \delta}{C6} \Bigg]$$

$$+ \; 0.37(3.39 \; \text{DELP} + 5.1 - \frac{3.39}{0.37}) \; e^{-C5} \; C9 \; \delta$$

$$+ \; \frac{2.5 \; C9}{C6} \Bigg] \; / \pi$$

$$+ \; 0.5\big[(2.5 \; \log \; C6 + 5.1)^2 \; V_w$$

$$+ \; 2.5 \; \log \; C6 - (3.39 \; \text{DELP} + 5.1)e^{-C5} + 5.1\big]$$

$$\bullet \; \big[C1 \; \delta - \eta\pi\big]/\pi + 7.305 \; e^{-C5}\big[(e^{C8}(0.8556 \; \eta \; U_\tau^2 \; |U_\tau|$$

$$+ \; 0.8556 \; \nu \; U_\tau^2 \;)\log^2 \; C7 + e^{C8}\big[1.7797 \; U_\tau^2(\eta \; |U_\tau| + \nu)\log \; C7$$

$$+ \; 1.7811 \; \eta e^{C8} \; U_\tau^2|U_\tau| \; \big]V_w$$

$$+ \; e^{C8}\big[0.3423 \; U_\tau^2 \; (\eta U_\tau + \nu)\big]\log \; C7$$

$$+ \; 1.2543 \; \eta \; |U_\tau|^3 + e^{C8}(0.3560 \; \eta \; U_\tau^2 \; |U_\tau| - 5.277 \; \nu \; U_\tau^2)$$

$$+ \; 5.277 \; \nu \; U_\tau^2 \;]/(U_\tau^2 \; |U_\tau|)$$

$$- \; 7.305 \; e^{-C8}\Bigg[(0.8556 \; e^{C8} \; \nu^2 \; U_\tau^2 \; |U_\tau| \; \log^2 \; C7$$

$$+ \; e^{C8}(1.7797 \; \nu^2 \; U_\tau^2 \; |U_\tau| - 1.71125 \; \eta \nu U_\tau^4)\log \; C7$$

$$- \; 1.7797 \; \eta e^{C8} \; \nu \; U_\tau^4\Bigg]V_w$$

$$+ \; 0.3423 \; e^{C8} \; \nu^2 \; U_\tau^2 \; |U_\tau|\log\big(\frac{\nu|U_\tau|}{\eta U_\tau^2}\big) + 1\big)$$

$$- 0.3423\ e^{C8}\ \nu^2\ U_\tau^2\ |U_\tau|\ \log(\nu\ |U_\tau|)$$

$$+ e^{C8}\left[(0.6845\ \nu^2\ U_\tau^2\ \log(U_\tau) + (0.3423\ \log\ \eta - 5.277)\ \nu^2\ U_\tau^2)\ |U_\tau|\right.$$

$$- 0.3423\ \eta\nu\ U_\tau^4\Big]$$

$$+ \left(0.4641\ \eta^2\ U_\tau^4 + 5.277\ \nu^2\ U_\tau^2\right)\ |U_\tau| + 1.9525\ \eta\nu\ U_\tau^4\ /(\ \nu\ U_\tau^4)\Bigg\}$$

$$\text{SECOND} = \frac{dU}{d\delta}\ U - \Bigg\{U_\tau\Big[-0.5\pi\ C1$$

$$\Big[-e^{-C5}(3.39\ \text{DELP} + 5.1) + (2.5\ \log\ C6 + 5.1)^2\ V_w$$

$$+ 2.5\ \log\ C6 + 5.1\Big]/\delta$$

$$+ 5.0\ \frac{U_\tau\ V_w}{\nu}\ \frac{(2.5\ \log\ C7\ 5.1)}{C7}$$

$$+ \frac{0.37\ U_\tau}{\nu}\ (3.39\ \text{ETAP} + 1.71)e^{-C8}$$

$$+ \frac{2.5\ U_\tau}{\nu\ C7}\Big]$$

$$+ \frac{0.5\ \pi U_e}{\delta}\ C1\Bigg\}\Bigg\{e^{-C5}\ U_\tau\Big[1.2543\ C1\ U_\tau^3\ \delta^4$$

$$- (1.2543\ \eta\pi U_\tau^3 + 3.6387\ C1\ \nu\ U_\tau^2)\ \delta^3$$

$$+ e^{C5}\Big[C1\ \nu^2 U_\tau(51.51\ V_w + 7.6)\ \delta^2$$

$$+ \left[C2\ C3\ (-26.01\ V_w + 5.1) + C1\ v^3(26.01\ V_w + 5.1) \right.$$

$$- 25.5\ C3\ V_w - 2.5\ C3 \bigg] \delta$$

$$+ C2\ C4\ (-26.01\ V_w - 5.1) \bigg]$$

$$+ e^{-C5} \log C6 \left[C1\ v^2\ U_\tau (38.0\ V_w + 2.5) \delta^2 \right.$$

$$+ C2\ C3\ (-25.5\ V_w - 2.5) + C1\ v^3(25.5\ V_w + 2.5) - 12.5\ C3\ V_w \bigg] \delta$$

$$+ C2\ C4\ (-25.5\ V_w - 2.5) \bigg]$$

$$+ e^{C5} \log^2 C6 \left[6.25\ C1\ v^2\ U_\tau\ V_w\ \delta^2 \right.$$

$$+ (6.25\ C1\ v^3\ V_w - 6.25\ C2\ C3\ V_w) \delta - 6.25\ C2\ C4\ V_w \bigg]$$

$$+ \left[3.39\ \eta v\ \pi\ U_\tau^2 (C2 + 0.2487) - 9.993\ C1\ v^2\ U_\tau \right] \delta^2$$

$$+ \left[8.49\ C2\ C3 + 1.503\ C3 - 5.1\ C1\ v^3 \right] \delta$$

$$+ 5.1\ C2\ C4 \bigg] / (2 v^2\ \pi U_\tau\ \delta^2 + 2 v^3\ \pi\delta)$$

$$- 0.5\ U_e (\delta^2\ C1 - C1\ \eta\pi\delta) / \pi\delta^2 \bigg\}$$

$$\text{THIRD} = 0.5 \left\{ U_\tau (-0.5 \ \pi \ C1 \right.$$

$$\left[(2.5 \ \log C6 + 5.1)^2 \ V_w + 2.5 \ \log C6 \right.$$

$$- (3.39 \ \text{DELP} + 5.1)e^{-C5} + 5.1)/\delta$$

$$+ \frac{5.0 \ (2.5 \ \log C7 + 5.1)U_\tau \ V_w}{C7 \ \nu}$$

$$+ \frac{0.37 \ U_\tau}{\nu} \ (3.39 \ \text{ETAP} + 5.1)e^{-C8}$$

$$- \frac{3.39 \ U_\tau}{\nu} \ e^{-C8}$$

$$+ \frac{2.5 \ U_\tau}{\nu \ C7} \left] + \frac{0.5 \ \pi \ U_e}{\delta} \right\} \frac{\delta \ C1 \ - \ \eta\pi}{\pi} + U \frac{dU}{dU}_\beta$$

$$\text{FOURTH} = U_\tau \left[+0.5(C2 \ - \ 1) \right] \left[\frac{5.0 \ U_\tau \ V_w \ \delta(2.5 \ \log C6 + 5.1)}{\nu \ |U_\tau| \ C6} \right]$$

$$+ \ 0.37 \ U_\tau \ \delta \ (3.39 \ \text{DELP} + 5.1)e^{-C5}/\left(\nu \ |U_\tau| \right)$$

$$- \ 3.39 \ C9 \ \delta \ e^{-C5} + 2.5 \ \frac{C9 \ \delta}{C6}$$

$$+ \frac{5.0 \ C9 \ \eta(2.5 \ \log C7 + 5.1)V_w}{C7}$$

$$+ \ 0.37 \ C9 \ \eta(3.39 \ \text{ETAP} + 5.1)e^{-C8}$$

$$- \ 3.39 \ C9 \ \eta \ e^{-C8} \quad + \frac{2.5 \ \eta \ C9}{C7}$$

$$- 0.5(1 - C2)\left[V_w(2.5 \log C6 + 5.1)^2\right.$$

$$+ 2.5 \log C6 - (3.39\ C6 + 5.1)e^{-C5} + 5.1\Big]$$

$$+ (2.5 \log C7 + 5.1)^2\ V_w + 2.5\ C7 - (3.39\ ETAP + 5.1)e^{-C8} + 5.1$$

$$FIFTH = U_\tau\left[0.5\ \eta\pi\ C1\left[V_w(2.5 \log C6 + 5.1)^2\right.\right.$$

$$+ 2.5 \log C6 - (3.39\ DELP + 5.1)e^{-C8} + 5.1)/\delta^2$$

$$- 0.5(1 - C2)\Big]\Big[5.0\ |U_\tau|\ V_w(2.5 \log C6 + 5.1)/(\nu\ C6)$$

$$+ 0.37\ |U_\tau|\ (3.39\ DELP + 4.1)e^{-C8}/\nu + \frac{2.5\ |U_\tau|}{\nu\ C6}\Big] - \frac{0.5\ \eta\pi U_e\ C1}{\delta^2}$$

$$SIXTH = 0.5\ (1 - C2)$$

where

$$ETAP = U_\tau\ \eta/\nu$$

$$DELP = U_\tau\ \delta/\nu$$

$$C1 = \sin\left(\frac{\pi\eta}{\delta}\right)$$

$$C2 = \cos\left(\frac{\pi\eta}{\delta}\right)$$

$$C3 = \eta \nu^2 \pi U_\tau$$

$$C4 = \eta \nu^3 \pi$$

$$C5 = 0.37 \text{ DELP}$$

$$C6 = \text{DELP} + 1$$

$$C7 = \text{ETAP} + 1$$

$$C8 = 0.37 \text{ ETAP}$$

$$C9 = \frac{U_\tau}{\nu \left| U_\tau \right|}$$

BIOGRAPHY

Chandra Sekhar Vemuru was born in Vijayawada, India on December 31, 1956. In June 1977, he received a Bachelor of Engineering degree in Mechanical Engineering from Mysore University, India. He received a Master of Technology degree in Mechanical Engineering with specialization in Heat Transfer and Thermal Power from the Indian Institute of Technology, Madras, India. He came to the United States of America in 1981 and enrolled in the graduate study program at the Old Dominion University.

In May 1983, he completed the course requirements for the Doctor of Philosophy degree at the Old Dominion University and started his dissertation research. During the period of research, he was associated with the Airfoil Aerodynamics Branch of the NASA Langley Research Center, Hampton, Virginia.

Chandra S. Vemuru married Padmaja Patury in 1984 and they presently live in Norfolk, Virginia.